University College London

# Computer Modelling Studies of Mackinawite, Greigite and Cubic FeS

Thesis submitted for the degree of Doctor of Philosophy (PhD) by

**Anthony John Devey**

Supervisor:

Prof. Nora H. de Leeuw

University College London

Department of Chemistry

October 2009

## Declaration

I confirm that this is my own work and that all material from other sources has been properly and fully acknowledged.

Anthony John Devey

October 2009

# Abstract

In this thesis we develop rigorous theoretical models for the simulation of the iron sulfides mackinawite, greigite and cubic FeS using both *ab initio* and interatomic potential methods.

The mineral mackinawite (tetragonal FeS) takes a layered PbO-type structure, with Fe atoms coordinated tetrahedrally to S ligands. We have used GGA+U calculations to show that the inter-layer interaction is very difficult to accurately describe using this form of DFT, and instead a single-layer formulism is developed which allows the modelling of the electronic and magnetic properties of a single layer of mackinawite. These results are used to derive an interatomic potential to investigate the surfaces of this phase, and we use the calculated surface energies to successfully reproduce the observed crystal morphology of mackinawite. The effect of impurity atoms in the interlayer sites is investigated, and it is found that these contribute considerably to the stabilisation of the mackinawite structure.

Greigite ($Fe_3S_4$) is the iron sulfide analogue of the famous iron oxide magnetite. We use spin-polarised GGA+U calculations to model the magnetic and electronic structure of greigite, and this phase is found to be most accurately described using an applied $U_{eff}$ value of 1 eV. Further calculations show that a Verwey-type low temperature transition in greigite is energetically unfavourable.

Cubic FeS takes the cubic sphalerite structure at room temperature. A low temperature transition to an antiferromagnetic orthorhombic structure has been observed experimentally. GGA+U calculations demonstrate that applying a value for the Hubbard $U_{eff}$ parameter of 2 eV provides an excellent description of both the low- and high-temperature structures. It is found that the previously derived potential for

mackinawite predicts the cubic FeS structure as well as non-spin-polarised GGA.

The work described in this thesis has provided a greater understanding of the electronic, magnetic and structural properties of these iron sulfides.

# Table of Contents

# Acknowledgements

I would first like to thank my supervisor, Prof. Nora de Leeuw, for a great deal of support throughout the last three years. Special mention should also go to Dr. Ricardo Grau-Crespo for his invaluable help and guidance over the past year, and for much advice, conversation and encouragement.

Gratitude also goes to the Royal Institution and the EPSRC for funding, and my second supervisor, Prof. Richard Catlow, for his support and helpful suggestions. Thank you also to Prof. Francesc Illas and his group for hosting me in Barcelona, and to the HPC-Europa program for providing travel funding

I also would like to mention the following people, who have enriched my experience at UCL immeasurably: Keith Butler; Kim Jelfs; Alan Lobo; Tom Daff; Devis di Tommaso, and all members of the group, past and present.

Acknowledgement should also be made of the machines on which this work was undertaken, including the HECToR, HPCx, Legion and Marenostrum supercomputers, and the Huygens and Compaq clusters.

Finally, thank you to my parents and to my girlfriend Kat, for everything.

# List of Publications

The work described in this thesis has been published in the following papers:

A. Devey, R. Grau-Crespo, N. H. de Leeuw, "Combined Density Functional Theory and Interatomic Potential Study of the Bulk and Surface Structures and Properties of the Iron Sulfide Mackinawite (FeS)", *J. Phys. Chem. C*, **112**, 10960 (2008)

A. Devey, R. Grau-Crespo, N. H. de Leeuw, "Electronic and magnetic structure of Fe3S4: GGA+U investigation", *Phys. Rev. B*, **79**, 195126 (2009)

A. Devey, N. H. de Leeuw, "DFT Study of the High- and Low-Temperature Phases of Cubic Iron Sulfide (FeS)", *Phys. Rev. B* (submitted) (2009)

A. Devey, N.H. de Leeuw, "GGA Study of Interstitial Impurities in the Iron Sulfide Mineral Mackinawite", (in preparation) (2009)

# 1. Introduction

The materials containing iron and sulfur are still a relatively infrequently studied group of compounds, whose importance in nature is only beginning to be widely recognised (Morse *et al.*, 1987; Rickard *et al.*, 2001; Rickard & Luther, 2006; Lill & Mühlenhoff, 2008). Due to their readiness to oxidise, these compounds were originally thought to play only a small role in natural processes; however recent investigations into the deep oceans of Earth, where the normally metastable phases of Fe-S minerals have been found to be stable over long timescales, have shown this assumption to be erroneous (Rickard & Morse, 2005). Iron sulfide clusters, complexes and solids are now considered to play major roles in the chemistry of marine systems (Rouxel *et al.*, 2005), proto-planetary disks (Keller *et al.*, 2002) and inorganic biochemistry (Rees & Howard, 2003). An excellent review of the literature is given in the book by Vaughan and Craig (1978) and the three review papers by Rickard *et al.* (2005; 2006; 2007). This thesis considers the solid phases in the Fe-S system, and is structured as follows:

Chapter one introduces the family of bulk iron sulfide materials, and discusses the moderately well studied phases pyrite and pyrrhotite; particular emphasis is placed on previous theoretical studies present in the literature. A discussion of current research into the role of Fe-S minerals in the origin of life, their occurrence around black smokers and their incorporation into biological systems is also presented.

Chapter two presents and explains the theoretical techniques used to build the

physical models of these materials, namely density functional theory (DFT) and interatomic potential (IP) methods. Extensions to the local density generalised gradient approximations, in particular the Hubbard U correction, are also discussed.

Chapter three examines the layered, tetragonal iron sulfide mackinawite (FeS) using DFT and IP techniques. The effect of impurity atoms in the interstitial octahedral sites between layers is also investigated using DFT.

Chapter four presents the investigation of the greigite ($Fe_3S_4$) spinel structure using DFT. In addition, a theoretical monoclinic form of greigite is investigated, analogous to that seen below the Verwey temperature in the isostructural iron oxide magnetite.

Chapter five details the modelling of the high- and low-temperature cubic FeS structures, with its magneto-structural transition, and Chapter 6 discusses the results of the previous chapters and suggests further avenues for research in this area.

## 1.1 Iron-Sulfur Materials

The only stable binary solids in the Fe-S system above 200°C and near ambient temperatures are the pyrrhotites, $Fe_{1-x}S$ (where x = 0 represents the stoichiometric end-member troilite, FeS), and pyrite, $FeS_2$ (Taylor, 1980). Many of the metastable phases occur widely at lower temperatures, in both natural and artificial environments. Figure 1.1 illustrates the known system of iron sulfides.

Ward (1970) made the distinction between the sulfides of iron in which S-S chemical bonding is not a pronounced structural feature and those where it is important in the stabilisation of the structures. The members of the first of these categories have tended to be poorly studied, primarily due to their instability under

oxidising conditions and difficulty in their synthesis. This study will concentrate upon the minerals in this first category, namely mackinawite (FeS), greigite ($Fe_3S_4$) and cubic FeS. The latter category includes both pyrite and its polymorph marcasite; these structures are discussed in the next two sections.

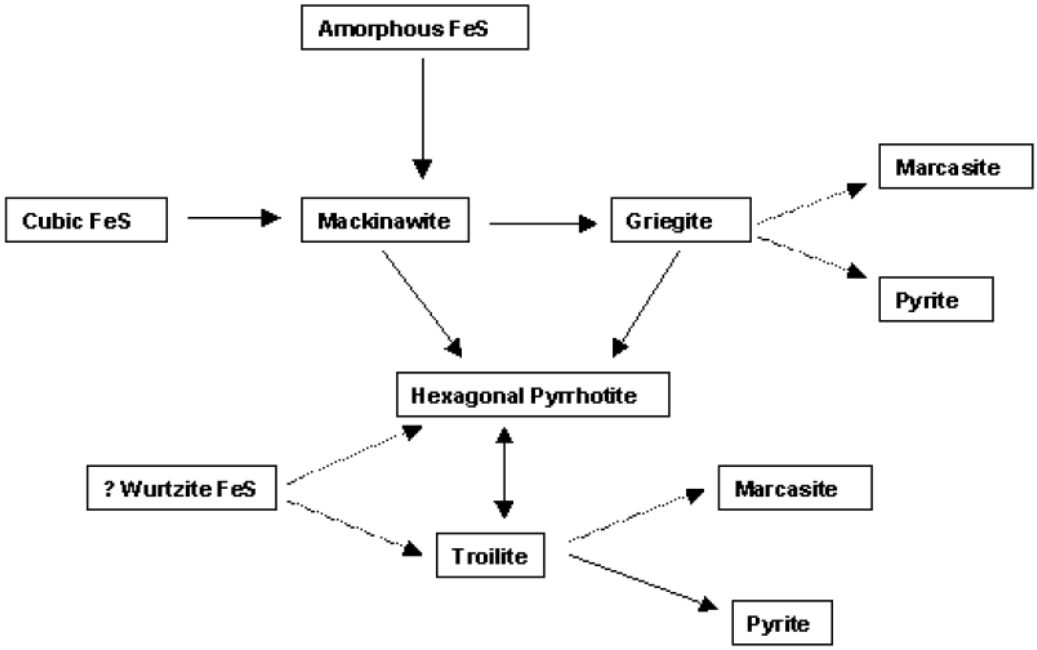


Figure 1.1 – Diagram showing the low temperature phase relations in the FeS system. Solid arrows indicate transformations that have been experimentally verified. Reproduced from Livens *et al.* (2004). Amorphous FeS and wurtzite FeS have not been observed.

Of the seven Fe-S materials known to exist, only troilite, pyrite and marcasite are to any extent well represented in the literature by either experimental or theoretical studies. Cubic FeS, mackinawite, and greigite have only patchy experimental data available. Very little data are available on the rhombohedral iron sulfide phase smythite, $Fe_9S_{11}$, (Fleet, 1982; Furukawa & Barnes, 1996) and due to confusion over its structure and composition this phase will not be considered in this

work.

A variety of other Fe-S phases have been suggested in addition to those listed above, most commonly by analogy with isomorphic Fe-O materials. For instance, although no conclusive evidence has been found that a haematite-analogue iron sulfide exists, it is on occasion reported in the literature; most recently as a hexagonal phase inside pyrrhotite samples (Farina *et al.*, 1990). This phase would be assigned the formula α-$Fe_2S_3$, in analogy with the oxide. Similarly, an iron-sulfur analogue to the lacunary iron oxide maghemite (γ-$Fe_2O_3$), which would be assigned the formula γ-$Fe_2S_3$, has been hypothesised to exist by Letard *et al.* (2005), and was suggested to form from the presence of ordered iron atom vacancies in greigite.

This thesis aims to provide theoretical descriptions of the mackinawite, greigite and cubic FeS phases. Before attention turns to these poorly understood materials, we briefly review previous studies of the pyrite and pyrrhotite phases.

## 1.2 Pyrite (Cubic $FeS_2$) and Marcasite (Orthorhombic $FeS_2$)

The chemical formula of the iron sulfide pyrite, $FeS_2$, was determined at the beginning of the 19$^{th}$ century (Hatchett, 1804), and over a hundred years later this mineral was one of the first crystal structures determined by the X-ray diffraction method (Bragg, 1913). Since then a wide variety of empirical and theoretical studies have focussed on pyrite, predominately due to its high stability (Kullerud & Yoder, 1959), ubiquity (about 5 million tons of pyrite are produced annually by the worlds oceans) (Rickard & Luther, 2007) and its importance as an ore mineral (Vaughan & Craig, 1978). The stability of this phase is the reason why pyrite is suspected to be the common end product which evolves from the other iron sulfides under normal conditions (Hunger & Benning, 2007), although this assertion remains to be proven

conclusively (Rickard & Luther, 2006).

Pyrite crystallises in the NaCl structure, with $Fe^{2+}$ in the $Na^{+}$ sites and the centre of mass of the dimeric sulfur $S_2^{2-}$ located at $Cl^{-}$ sites. The molecular axis of the $S_2^{2-}$ dimers is aligned along the four equivalent (111) directions (Huggins, 1922). This cubic structure possesses the lattice parameters $a = b = c = 5.418$ Å, with all iron atoms octahedrally arranged in relation to the sulfur ligands. Pyrite is diamagnetic (it exhibits magnetism only in a strong magnetic field), and as such its six Fe *d*-orbital electrons are paired and completely fill the $t_{2g}$ orbitals. This low-spin configuration of the $Fe^{2+}$ is an indication of the strength of the ligand field due to the disulfide anions (Vaughan & Craig, 1978). Semiconducting properties are observed, with a measured energy gap of around 0.9eV (Schlegal & Wachter, 1979) and natural pyrite samples are known to exhibit both n- and p-type behaviour, on occasion within the same crystal (Rimstidt & Vaughan, 2003). It is this semiconducting behaviour which has attracted major interest in the use of pyrite for solar energy systems (Ellmer & Hopfner, 1997).

Experiments by Benning *et al*. (2000) suggested that below 100°C mackinawite is the precursor in the formation of pyrite, and that an oxidant is required for the formation to occur. The reaction was said to proceed via the intermediate, mixed valence ($Fe^{2+}/Fe^{3+}$) phase greigite ($Fe_3S_4$). The difficulty in determining reaction energies lies in the incorrect values used for the Gibbs free energy of formation for the hexaaqua $Fe^{2+}$ ion (Parker & Khodkovskii, 1995). However, it has been noted that the solid-state transition of greigite to pyrite has not been observed conclusively, and is structurally and chemically improbable as a process; the considerable rearrangement of the S lattice which is required creates a massive energy barrier (Rickard & Luther, 2006).

Density functional theory (Muscat *et al.*, 2002), MO (Molecular Orbital) (Bither *et al.*, 1968; Luther, 1987) and interatomic potential (de Leeuw *et al.*, 2000) theoretical treatments have proved very useful in the description of the pyrite phase. Using classical interatomic potentials derived for the $FeS_2$ structure, de Leeuw *et al.* (2000) determined surface stabilities, water adsorption energies and the effects of stepped-surfaces for the {100}, {110} and {111} surfaces. Muscat *et al.* (2002) found that DFT-GGA predicts to within a good accuracy the unit cell parameters, internal S coordinates and S-S bond distance of the $FeS_2$ structure; however Hartree-Fock (HF) calculations failed to reproduce these properties, presumably due to an underestimation of the level of electron correlation present. It is also found that both GGA and HF incorrectly predict pyrite to be a conductor, presumably for the same reason. Further DFT studies using improved GGA formalisms have correctly predicted the bulk band-gap, and have advanced to the investigation of the (100) and (110) surfaces of pyrite to determine surface relaxations and energies (Hung *et al.*, 2002); a further study examined the (001) surface (Cai & Philpott, 2004). Other studies have extended these models to examine the behaviour of a variety of adsorbates on these surfaces, for example $As(OH)_3$ (Blanchard *et al.*, 2007), xanthate (Hung *et al.*, 2004), $H_2S$ (Stirling *et al.*, 2003a) and water (Stirling *et al.*, 2003b).

Marcasite is the sole known polymorph of pyrite, and this phase is also characterised by the presence of dimeric sulfur anions, $S_2^{2-}$. Marcasite is orthorhombic with the lattice parameters $a$ = 4.443 Å, $b$ = 5.424 Å and $c$ = 3.387 Å, and space group *pnnm* (Tossell & Vaughan, 1981). The formation mechanism of marcasite is unclear (Schoonen & Barnes, 1991), but the electronic structure has been modelled in much the same way as pyrite (Bullett, 1982; Reich & Becker, 2006), suggesting that theoretical methods, and DFT in particular, is successful in the description of both of

these phases.

## 1.3 The Pyrrhotites

The pyrrhotite minerals ($Fe_{1-x}S$ with $0 \leq x \leq 0.125$) vary from the cation-deficient, monoclinic NiAs-structure $Fe_7S_8$ to the slightly-distorted NiAs-like structure troilite (the FeS end-member, where x = 0) (Vaughan & Craig, 1978). The members of this mineral family demonstrate a variety of magnetic behaviour depending on the stoichiometry. For example, the monoclinic form shows ferrimagnetism, while hexagonal pyrrhotite ($Fe_{11}S_{12}$) has an antiferromagnetic nature. The pyrrhotites are rarely seen in marine environments due to their propensity to convert to pyrite (Rickard & Luther, 2007).

Troilite has prompted a number of theoretical studies, mainly due to its discovery in meteorites (Takele & Hearne, 2001) and suspected presence in the cores of planets (Lie *et al.*, 2001). Studies of troilite are of particular interest to the current work since DFT (Raybaud *et al.*, 1997; Hobbs & Hafner, 1999) and also DFT+U (Rohrbach *et al.*, 2003) techniques have been applied to this phase. These studies found that although the phase transition between the non-magnetic NiAs-type and the antiferromagnetic troilite phase is well described, the semiconducting gap is not predicted in a similar manner to that found in the pyrite studies. The addition of a Hubbard $U_{eff}$ value of around 1 eV corrects this deficiency (to a degree), although different values of $U_{eff}$ are needed to accurately predict different properties (See section 2.2.6 for a discussion of the Hubbard U parameter). Wells *et al.* (2004) studied the troilite, pyrrhotite and MnP structures using DFT in the generalised gradient approximation (GGA) approximation and found that this correctly predicted structures and transition pressure; however this study did not consider the band

structure in any way.

## 1.4 Iron Sulfides and Black Smokers

The floor of the deep ocean, along mid-ocean ridges, is home to a large number of hydrothermal vents, first discovered in 1977 and given the name “black smokers” (Jannasch & Wirsen, 1979), so called because the precipitated sulfides and sulphates colour the surrounding waters black. These particulates are formed when superheated water from beneath the Earth’s crust is emitted through the ocean floor, forming chimney-like structures with heights of up to 20 feet and temperatures of around 350°C. This superheated water contains a large variety of minerals from the crust, most notably sulfide compounds. As the superheated water hits the cold marine waters a number of materials are deposited, including iron sulfides (Luther *et al.*, 2001). Another striking property of the black smokers is the rich variety of elements and compounds they contain, including Cu, Fe, $H_2S$, Zn, Na, Cl and Mg, which has important implications for the incorporation of impurities in sulfides (Von Damm, 1990). As a result, the walls of black smokers consist of zinc sulfides, iron sulfides and copper-iron sulfides in the interstitial sites between deposits of anhydrite, $CaSO_4$ (Verati *et al.*, 1999).

Black smokers lie at the centres of entire ecosystems, which, in the absence of light from the sun, derive their energy from either chemosynthesis or use the glow from the black smoker for photosynthesis (Takai *et al.*, 2001). This had led to suggestions that life itself evolved in these environments and that Fe-S compounds are key components in this process; the so called “iron-sulfur world hypothesis” (Wächtershäuser, 2000).

## 1.5 The Role of Iron Sulfides in the Origin of Life

It is accepted that three conditions needed to be satisfied for the creation of organic molecules upon the early Earth (Cairns-Smith *et al.*, 1992): The presence of organic elements in sufficient concentrations; a highly reducing environment; and a suitable location far from the highly oxidizing UV radiation of the sun. The final criterion is thought to have been satisfied deep in the early ocean, while the donation of electrons through the oxidation of Fe(II) to Fe(III) is considered the most plausible source of electrons for reduction, since iron is the main constituent of the Earth's core and, because of its two common valence states, may accept, store and transfer electrons under various conditions (Russell & Martin, 2004). It had been suggested (Wächtershäuser, 1997) that the formation of pyrite was the principle energy source of a surface metabolist, however this was discounted on the grounds that the iron in pyrite is unable to partake in metabolism reactions (Schoonen *et al.*, 1999). This prompted the investigation of other FeS compounds as the vital reactants.

Those compounds which conduct electrons, and where the valence state of iron can be switched readily, seem plausible contenders. These iron minerals include mackinawite (FeS) and the mixed valence, more oxidised greigite ($Fe_3S_4$). Development of this theory has led to the suggestion that life originated around deep ocean springs on the floor of the Hadean Ocean around 4.2 thousand million years ago (Russell *et al.*, 1994, 1997, 2004). This hot, anaerobic deep sea environment contained both bi-sulfide bearing alkaline seepage waters from underwater vents and acidulous (due to high levels of $CO_2$), Fe-bearing ocean water from which mackinawite (FeS) formed as a colloidal membrane at the redox and pH front where these waters met. It is thought that the incorporation of Ni leads to this semi-permeable membrane acting as a catalytic surface / boundary for the transfer of

electrons for reduction reactions to form organic molecules.

The theory visualises that the mackinawite membrane expanded due to thermal differential effects until failure, when daughter bubbles of FeS were produced, which acted as permeable membranes. These bubbles would have encapsulated a highly reduced, high pH hydrothermal solution, separate from the low pH external solution. Empirical studies into the initial reactions of life have confirmed that high concentrations of organic molecules are required for the synthesis of amino acids, far higher than those present in the primordial ocean as a whole. The presence of these bubbles or coacervates (Walde *et al.*, 1994) encapsulated by an iron sulfide membrane offer plausible "reaction chambers" within which sufficient concentrations of reactants would be able to congregate.

The earliest `living` organisms, distant ancestors of the modern prokaryote (and all life on Earth), are thought to have been anaerobic chemoautotrophic microbes (Thauer *et al.*, 1977). Similar microbes around today utilise redox enzymes containing Ni-S and Fe-S clusters to metabolize hydrogen, carbon dioxide and carbon monoxide. These enzymes contain a variety of Ni-Fe-S compounds, and are likely to have evolved from primordial reactions.

The mackinawite membrane is envisaged to go through geochemical transformations, which formed the mixed-valence catalytic phases which use $H_2$ as the primary electron donor. Russell and Hall (1997) suggested greigite ($Fe_3S_4$) and Violarite ($FeNi_2S_4$) in addition to mackinawite (Cody, 2004) as favourable catalysts, due to their similarity to the cubane structure ($Fe_4S_4$) with four iron ferrodoxins. FeS is a plausible catalyst, and has been shown to be a strong reactant (Heinen & Lauwers 1996). It is the catalytic nature of these phases that is thought to promote the key redox chemistry necessary for metabolism. Practical interest in Fe-S materials and

cubane clusters centres on the possibility of their use in carbon fixation, since biological systems, such as Fe-S clusters, have been found to be capable of activating and converting the $CO_2$ molecule into a range of organic materials despite its high thermodynamic stability (Russell & Martin 2004; Volbeda *et al.*, 2005). The similarity in the structures of these cubane clusters to those of the iron sulfides mackinawite and greigite indicates that these minerals offer a valuable route of enquiry.

The implication of metastable iron sulfide compounds in the development of life highlights the need for a thorough understanding of these materials, their surface chemistry, and their propensity for both phase transitions and catalytic behaviour.

## 1.6 Iron Sulfides in Biological Systems

Both greigite and pyrite have been found in the shell of a deep-sea dwelling mollusc, which lives in the vicinity of black smokers (Goffredi *et al.*, 2004). The presence of greigite provides a magnetic character to the snail's shell, for reasons that are at present unclear. The iron sulfide scales do however bear strong resemblance to those found to belong to the very first complex animals, which lived in the Cambrian period (540-500 million years ago) (Yi *et al.*, 1989). Indeed, the magnetic nature of greigite is used extensively by strains of magnetostatic bacteria, where the mineral is grown by the organism into magnetosome morphologies (Pósfai *et al.*, 1998b). These needle-like structures are used by the bacteria to align with the Earth's geomagnetic field in order to navigate to regions of optimal oxygen concentration (Blakemore, 1975).

Iron sulfide clusters, which are very similar in structure to areas of the surfaces of the metastable Fe-S solid phases, are widespread in biochemistry where they make up the active centres of FeS proteins such as ferrodoxin (Nicolet *et al.*, 1999).

## 1.7 Summary

A review of the literature on iron sulfides suggests that there is a great deal of scope for further theoretical studies regarding these phases. Chapters three, four and five will examine in detail the current understanding of the iron sulfide phases in question (mackinawite, greigite and cubic FeS respectively), and describe the models we have developed for their description. The importance of working theoretical models for these iron sulfides should not be underestimated, since this would lay the groundwork for a more thorough understanding of iron sulfide chemistry, and provide a means to further examine the richness of the electronic and magnetic behaviour observed in these materials. The analogy of pyrite is instructive; once the DFT model was shown to provide a good description of the bulk solid, studies of the surfaces (and reactions which take place in the vicinity of those surfaces) were able to proceed and provide important insights.

# 2. Computational Methods

Materials modelling methods can be divided into two categories, which differ in the level of physical theory which they implement. The classical interatomic potential (IP) methodology treats atoms as idealised nomological objects which possess no internal structure, and interact only according to different forms of potential energy relations; the second type, *ab initio* electronic structure methods, consider the electronic structure of materials using the modern mathematical framework of quantum mechanics. This study uses both methods, as each has its own distinct advantages for the purposes of describing different physical systems. In general, IP methods are able to deal with systems composed of a far greater number of atoms (of the order of 100,000) than *ab initio* techniques (which can manage up to around a 100). They are, however, unable to provide any details regarding the electronic structure of the systems under consideration, which is the domain where *ab initio* techniques come into their own.

In this study, IP modelling is implemented within the programs GULP (the General Utility Lattice Program) and METADISE (Minimum Energy Techniques Applied to Dislocations, Interface and Surface Energies). GULP is a molecular modelling program which facilitates the fitting of interatomic potentials to energy surfaces and empirical data, in addition to the predictive modelling of material properties. METADISE is a surface modelling program that implements a two-region approach for the calculation of surface energies of planar, dislocated and other forms

of crystal surfaces.

The *Ab initio* density functional theory (DFT) techniques used in this thesis are implemented within the program VASP (Vienna *Ab initio* Simulation Package), a comprehensive computer modelling package for performing quantum mechanical energy minimisation and molecular dynamics simulations using the plane-augmented-wave (PAW) method and a plane wave basis set.

This chapter gives an overview of the theoretical background and computational implementation of these methods.

## 2.1 Interatomic Potential Techniques

### 2.1.1 Interatomic Potential Models

Interatomic potential techniques are based upon the Born model of solids (Born and Huang, 1954), which assumes that the ions in a crystal lattice interact solely through long- and short-range electrostatic forces. Although such simulations can provide no information relating to the electronic structure of materials, they do afford a powerful and tractable method for modelling crystal structures and physical phenomena such as surface stability, defect characteristics or crystal growth. The GULP program (Gale 2003) permits the fitting of potential energy terms to either experimental data or data acquired from other, higher quality calculations, in order to provide an accurate physical model of the system in question.

The fitting of interatomic potential parameters uses the “sum of squares” method to measure the degree of agreement between the potential model and the known quantities which are to be fitted. This “fit” is denoted by the parameter F, and is defined according to:

$$F = \sum_{\text{all observables}} W\left(f_{ideal} - f_{calc}\right)^2 \qquad (2.1.1)$$

where $f_{calc}$ is the calculated quantity, $f_{obs}$ is the observed quantity and W is a weighting factor. The aim of the fit is to minimise this sum of squares by varying the potential parameters, where F = 0 corresponds to a perfect fit.

The potential energy relation between two ions takes the familiar form of the Coulomb potential:

$$U = \frac{q_1 q_2}{r} + \varphi \qquad (2.1.2)$$

where the first term on the right-hand side represents the long-range electrostatic interaction between atoms; $q_1$ and $q_2$ are the charges assigned to the first and second atoms respectively, and r is the separation between the atomic centres. The second term on the right-hand side, φ, represents the short-range forces acting between atoms. These short range interatomic forces, which include both the electrostatic repulsive forces and the Van der Waals interaction acting between neighbouring electron charge clouds, are described by simple analytical functions. The short range cation-anion and anion-anion interactions are described using an effective Buckingham potential:

$$\Phi_{ij}(r_{ij}) = A_{ij} e^{-r_{ij}/\rho_{ij}} - \frac{C_{ij}}{r_{ij}^6} \qquad (2.1.3)$$

where $\Phi_{ij}$ represents the potential, $r_{ij}$ the distance and $A_{ij}$, $\rho_{ij}$ and $C_{ij}$ represent the potential parameters describing the interaction between an ion at site i and a second ion at site j. According to the classical picture of the atom, $A_{ij}$ and $\rho_{ij}$ correspond to the size and hardness of the ion, respectively. However, in an effective pair potential such as that used here, and in most other instances, the $A_{ij}$ and $\rho_{ij}$ parameters interdependently govern the first term, and are mathematically inseparable. In this case, the first term represents the short-range repulsive interaction between the ions,

while the second term represents the attractive Van der Waals (dispersive) forces.

The electronic polarisability of the sulfur ion is accounted for via the shell model of Dick and Overhausen (1958), in which each polarisable ion is represented by a core and a massless shell, connected by a theoretical "spring" with an associated spring constant. The polarisability of this core-shell system is determined by the spring constant and the charges assigned to the core and shell. The form of the interaction is that of a harmonic potential:

$$\Phi_{ij}^{\text{core-shell}}\left(r_{ij}\right) = \frac{1}{2} k_{ij}\left(r_{ij} - r_0\right)^2 \qquad (2.1.4)$$

where $k_{ij}$ is the bond force constant, $r_{ij}$ is the separation between cation i and anion j and $r_0$ is the same separation at equilibrium.

Finally, the long-range Coulombic interactions between ions are calculated using Ewald summation (Ewald, 1921). Since bulk materials are considered to be composed of infinitely repeating unit cells, the inverse square form of the Coulomb interaction leads to the potential energy exponentially increasing outwards from a point. In order to prevent this infinity, the summation of the interaction energies is split into a short-range part and a long-range part, with the stipulations of charge neutrality and zero dipole moment. The Coulomb summation proceeds in real space over the short-range part, while the long-range summation is conducted over Fourier space, which has the advantage of converging rapidly (Kittel, 1986).

### 2.1.2 Surface Calculations

The treatment of surfaces in the IP calculations is implemented in the METADISE program (Watson *et al.*, 1996), which is adept at dealing with the construction and re-construction of polar surfaces. This code determines unrelaxed and relaxed surface

energies and surfaces structures, and follows the surface-typing scheme of Tasker (1979). In this formulism there are three possible ionic surface types, defined in the following way:

1. Type I surfaces are uncharged and no dipole exists in the stacking plane;
2. Type II surfaces have no dipole normal to the surface, but contain a net charge per stacking plane;
3. Type III surfaces possess a dipole normal to the surface, and each stacking plane is alternately charged.

The Coulombic interactions are calculated using a variant of the Ewald sum, the Parry method (Parry, 1975). This considers the crystal as a series of charged planes of infinite size, terminating at the surface in question. Because the Parry sum will stretch to infinity if a net dipole exists normal to the surface, any type III surface must be reconstructed in such a way as to remove the surface dipole.

A useful measure of the stability of crystal surfaces is the surface energy, denoted by $\gamma$, which is defined as the energy per unit area that is required to form the crystal surface, relative to the bulk. This is given by:

$$\gamma = \frac{U_s - U_B}{A} \qquad (2.1.5)$$

where $U_s$ represents the internal energy of region 1, $U_B$ represents the internal energy of an equivalent number of bulk atoms in region 2, and A is the surface area. The lower the surface energy, the more stable the surface.

Once the surface type has been characterised, the theory considers the crystal as consisting of charged stacks of planes of atoms periodic in two dimensions and parallel to the surface being investigated. A block of such stacks is chosen which extends into the crystal and models a specific area of surface. This block is further

separated into two regions: region 1 is the “near-surface” region, which includes the surface plane and a few layers underneath; and region 2 is a “bulk” region below region 1 (Figure 2.1). The atoms of region 1 are permitted to relax to their surface equilibrium positions, while those of the bulk are fixed at the bulk equilibrium positions. The sizes of both blocks are increased until the surface energy no longer varies, signifying convergence.

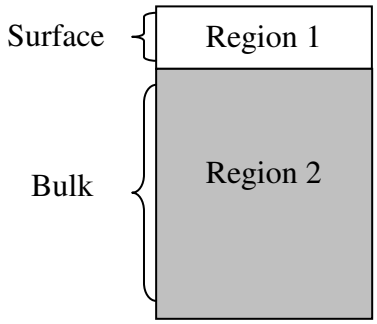


Figure 2.1 – Schematic representation of the two region approach used to model a single surface block.

## 2.2 Density Functional Theory

### 2.2.1 Introduction

Quantum theory describes the physical world on the atomic scale, where the quantization or “graininess” of quantities, such as energy, becomes apparent. This leads to the formulation of physical models on the nanoscale that are very different from those used in classical physics. The initial implementations of quantum mechanical calculations were based upon the determination of the wavefunction of a system, which due to the dual particle-wave nature of matter is required to describe

observed phenomena. It was soon discovered that systems with more than one electron, or "many-body" systems, were extremely difficult to solve (Lewars, 2003) and the accurate description of periodic solids practically impossible.

In view of these difficulties, it was first suggested by Thomas (1927) and Fermi (1928) and later elucidated by Kohn and Sham (1965) that the description of a system might be made in terms of the electronic charge density. This scalar quantity is dependent upon only a single spatial vector, instead of the vastly complicated many-electron vector wavefunction. The electron density itself is intimately related to the ground state energy of the entire system of electrons and nuclei, and once this energy is known any physical property that can be related to a total energy, or to a difference between total energies, can be calculated. Such total-energy techniques have been used to predict such properties as equilibrium lattice constants, bulk moduli, phonon modes, piezoelectric constants, and phase-transition pressures and temperatures (see Payne *et al.* (1992) for a discussion). The quantum mechanical mathematical framework based upon the consideration of the electron charge density was named density functional theory (DFT).

DFT is, in principle, an exact theory, however in practice various approximations must be made in order to obtain a tractable form for the mathematics for real systems. These approximations all relate to the many-body interacting electron system, which by its nature is immensely complicated. This problem is approached by treating the many-body interactions as a simpler, one-body interaction, which describes an "imaginary" non-interacting electron system which possesses the same density as the real, interacting one. In turn, the many-body interactions are modelled using further approximations. The choices that must be made in DFT calculations, including the form of the exchange-correlation functional, the selection

of a basis-set for the expansion of the Kohn-Sham orbitals and the algorithms adopted for solving the Kohn-Sham equations and for calculating energies, forces and stresses are examined in the following sections. The degree to which the chosen functional accounts for many-electron correlations, and the completeness of the basis-set, determine the accuracy of the calculation whilst the numerical algorithms are decisive in regards to its efficiency (Hafner, 2007).

### 2.2.2 Foundations of DFT

DFT begins by considering the Hamiltonian, H, of a system of *n* interacting electrons acted upon by an electrostatic field:

$$H = T + U + V = H_0 + V \qquad (2.2.1)$$

where T is the kinetic energy of the electrons, U is the mutual interaction energy of the electrons, $H_0$ is the Hamiltonian of the interacting electron system (excluding the external field) and V is the interaction energy between the electron system and the external field due to the nuclei. The separation of the energy of the electrons from that of the external field is crucial, and follows from the Born-Oppenheimer approximation (Eckart, 1935), which proposes that, due to the large mass difference between nuclei and electrons, the nuclei can be assumed to be stationary in relation to the moving electrons. Thus the nuclei may be treated *adiabatically*, leading to a separation of the electronic and nuclear coordinates in the many body wavefunction (Note that in the quantum mechanical usage of the term, adiabatic signifies that the change in the Hamiltonian of a system is infinitely slow). In addition, relativistic effects relating to the valence electrons are assumed to be negligible, a justifiable simplification for lighter nuclei such as Fe or S, where the outer electrons do not reach relativistic energies (Engel, 1998). Any relativistic effects relating to the core

electrons are taken care of by pseudopotentials.

The two theorems of DFT may then be applied (Hohenburg & Kohn, 1964). Theorem 1 states that it is impossible that two different external potentials could ever give rise to the same ground state density distribution; this is equivalent to asserting that a ground state electron density distribution, $n(\underline{r})$, must determine a unique external potential for that distribution, and hence must determine the many-body wavefunction also. To state this more succinctly, $n(\underline{r})$ uniquely specifies the external potential $v(\underline{r})$, and hence the many-body wavefunction $\Psi$.

Theorem 2 (the variational principle) states that in order to find the ground state energy for a given potential, it is necessary to vary the electron density with respect to the energy of the system. The minimum in this energy corresponds to the ground state electron density, $E_g[n(\underline{r})]$. Thus by minimising $E_g[n(\underline{r})]$ with respect to $n(\underline{r})$ for a fixed $v(\underline{r})$, the $n(\underline{r})$ which yields the minimum energy must be the electron density in the ground state. Taken together, these two theorems provide the means to find the ground state energy for any given external potential.

Consideration of the components of the energy leads to the following total energy functional for the system:

$$E_{tot}[n] = \int d\underline{r}\; v(\underline{r})n(\underline{r}) + T[n] + E_H[n] + E_{xc}[n] \qquad (2.2.2)$$

The first term on the right-hand side represents the electrostatic interaction between the external field and the electrons, and the second term the total kinetic energy of the electrons. The third is the electrostatic energy of the charge distribution of the electrons (the Hartree energy), given by:

$$E_H[n(\underline{r})] = \frac{1}{2}e^2 \int d\underline{r}\; d\underline{r}' \frac{n(\underline{r})n(\underline{r}')}{|\underline{r} - \underline{r}'|} \qquad (2.2.3)$$

The last term on the right-hand side of Equation (2.2.2), $E_{xc}[n]$, is the exchange-

correlation energy, and accounts for all the electronic many-body interactions which are not included in the other terms. Thus the differences between the non-interacting electron model "state" and the true state are conglomerated into this term.

The Kohn-Sham potential, which corresponds to the scalar potential field which gives the ground state energy for the ground state electron density, is defined as:

$$V_{KS}(\underline{r}) = v(\underline{r}) + e^2 \int d\underline{r}' \frac{n(\underline{r}')}{|\underline{r} - \underline{r}'|} + \frac{d(n\varepsilon_{XC}(n))}{dn} \qquad (2.2.4)$$

The many-body electronic problem is approached using a fictitious, one-particle wavefunction, $\psi_i$. This effectively converts the interactions of all the electrons into an average interaction and from the minimisation of the non-interacting energy functional with respect to $\psi_i^*$ the following set of Schrödinger-like equations is found. These are the Kohn-Sham equations:

$$\hat{H}_{KS}\psi_i(\underline{r}) = \left[ -\frac{\hbar^2\nabla^2}{2m} + V_{KS}(\underline{r}) \right] \psi_i(\underline{r}) = \varepsilon_i \psi_i(\underline{r}) \qquad (2.2.5)$$

where the Hermeticity (an operator is Hermetic if it possesses an orthonormal basis in which the operator can be represented as a diagonal matrix, with entries of real numbers) of the operators ensures the possibility of choosing the constraints in such a way that the orthonormality conditions for the fictitious wavefunction are satisfied:

$$\int \psi_i^*(\underline{r})\ \psi_j(\underline{r})\ d\underline{r} = \delta_{ij} \qquad (2.2.6)$$

In order to solve the Kohn-Sham equations, an iterative method is used with an initial "guess" for the wavefunctions. Application of the potential evolves both the electron density and energy into self-consistency. This method has obvious advantages, notably that it uses the mature field of matrix computational methods that are well suited to even relatively large systems (Gourley & Watson 1973). It is

important to note that the wavefunctions in this treatment have no physical meaning – they represent the eigenstates of the one-body density matrix and as such are wavefunctions of the fictitious non-interacting electron system.

The theoretical approach used so far can be expected to be very successful when the dominant part of the energy consists of the kinetic and electrostatic terms, described as they are without approximation. This leaves only the exchange-correlation term in Equation (2.2.2) to consider.

### 2.2.3 Exchange-Correlation and the LDA

The exchange-correlation energy functional, $E_{xc}[n]$, encompasses all electron-electron interactions other than the Coulomb interaction. An understanding of the nature of this functional is made possible by taking the well understood non-interacting system (Perdew *et al.* 1981) and gradually introducing the interactions, via an interaction parameter λ which is varied from 0 (non-interacting) to 1 (the physical system). This must be accompanied by an external potential $V_\lambda$ adjusted such that $n(\underline{r})$ is not a function of λ (Harris & Jones, 1974). The exchange-correlation energy can then be expressed as an integral over λ (Langreth & Perdew, 1975):

$$E_{xc} = \frac{1}{2}\int d\underline{r}\; n(\underline{r}) \int d\underline{r}' \frac{1}{|\underline{r}-\underline{r}'|} n_{xe}(\underline{r}, \underline{r}'-\underline{r}) \qquad (2.2.7)$$

with

$$n_{xc}(\underline{r}, \underline{r}'-\underline{r}) \equiv n(\underline{r}') \int_0^1 d\lambda \left(g(\underline{r}, \underline{r}', \lambda) - 1\right) \qquad (2.2.8)$$

Where $n_{xc}$ is the exchange-correlation hole, which describes the effect of the interelectronic repulsion using the pair correlation function, $g(\underline{r}, \underline{r}', \lambda)$. $n_{xc}$ can be considered as a measure of the effect where the presence of an electron at $\underline{r}$ reduces

the probability of finding another electron at $\underline{r}$'. In turn, this provides a means of evaluating local (short-range) correlations between electrons. Thus the associated exchange-correlation energy can be viewed as the energy resulting from the interaction between an electron and its own exchange-correlation hole.

Determining the form of the exchange correlation functional requires the determination of the pair-correlation function, which can be found for model systems (Parr and Yang, 1989). These considerations lead to the local density approximation (LDA). The LDA assumes that the exchange-correlation energy of a real system behaves locally as a uniform, homogeneous electron gas of the same density. The exchange-correlation energy per unit volume at position $\underline{r}$ is given by $n(\underline{r})\varepsilon_{xc}(n(\underline{r}))$, which in turn gives:

$$E_{xc}^{LDA}[n] = \int \varepsilon_{xc}^{hom}(n(\underline{r}))n(\underline{r})d\underline{r} \qquad (2.2.9)$$

where $\varepsilon_{xc}^{hom}(n(\underline{r}))$ is the exchange-correlation energy of the homogeneous electron gas. The exchange-correlation potential can be obtained from the exchange-correlation energy functional:

$$v_{xc}^{LDA}(\underline{r}) = \frac{\delta E_{xc}^{LDA}[n]}{\delta n(\underline{r})} = \left.\frac{\partial F_{xc}(n)}{\partial n}\right|_{n=n(\underline{r})} \qquad (2.2.10)$$

where $F_{xc}(n) = \varepsilon_{xc}^{hom}(n)n$. This approximation was intended to work with systems in which the electronic charge density is expected to be smooth (for example metals with nearly-free electrons).

The exchange-correlation energy can be further split into its component exchange and correlation parts, according to $\varepsilon_{xc} = \varepsilon_x + \varepsilon_c$. The exchange energy in the LDA formulism, $\varepsilon_x$, is given by the Dirac formula (Dirac, 1930):

$$\varepsilon_x^{Dirac} = -\frac{3}{4}\left(\frac{3}{\pi}\right)^{\frac{1}{3}} n^{\frac{1}{3}} = \frac{0.458}{r_s} a..u \qquad (2.2.11)$$

Where $r_s = (3/(4\pi\pi))^{1/3}$ and n is the number of electrons per unit volume. The correlation part is much more complicated, and is commonly found from high-level Monte Carlo calculations for a homogeneous electron gas of various densities (Ceperley & Adler, 1980). For systems where magnetism is likely to play an important role it is possible to extend the LDA to magnetic systems by splitting the total population of electrons into two groups, the first with spin up and the second with spin down, and considering each group individually. The interaction between the two groups is treated separately. This approach is termed the local spin density approximation (LSDA).

### 2.2.4 Local Spin Density Approximation

The treatment of magnetic systems, where the number of spin-up electrons is not exactly balanced by the number of spin-down, is simplified by treating the exchange-correlation functional as explicitly dependent on the two electron spin populations separately. In this case, the first three terms of Equation (2.2.2) remain the same, with the exception of the exchange correlation functional which becomes (Oliver & Perdew, 1979):

$$E_{xc}^{LSD}[n_\uparrow, n_\downarrow] = \int \varepsilon_{xc}^{hom}(n_\downarrow(\underline{r}), n_\uparrow(\underline{r}))\ n(\underline{r})\ d\underline{r} \qquad (2.2.12)$$

with the exchange-correlation potential:

$$v_{xc}^{LSD}(\underline{r}) = \frac{\delta E_{xc}\left[\ n^{\uparrow}, n^{\downarrow}\right]}{\delta n(\underline{r})} \qquad (2.2.13)$$

The two spin populations interact through their mutual Hartree and exchange-correlation energies, and the effective field acting upon one of them depends on the opposing spin charge density also. Equation (2.2.13) also illustrates that magnetic

phenomena in a system emerge solely from the exchange-correlation term, and that a reliable treatment of systems where magnetism is important requires a sound treatment of this term.

The exchange and correlation functionals of this spin dependent approach may also be split into exchange and correlation parts. The exchange contribution is obtained by extending the non-spin-polarised expression:

$$E_x^{LSDA}[n] = \sum_\sigma \int F_x^{LSDA}(n_\sigma(\underline{r}))d\underline{r} = \sum_\sigma F_x^{LSDA}(2n_\sigma(\underline{r}))d\underline{r} \qquad (2.2.14)$$

where $F_x^{LSDA}$ represents the same functional as used in the unpolarised LDA case and σ denotes the spin-populations. The spin-polarised correlation functional is obtained by interpolating the results for the homogeneous electron gas at different spin polarisations; the resulting functional can be expressed as dependent upon both the total charge density $n(\underline{r})$ and the magnetisation $m(\underline{r})$, which is defined as:

$$m(\underline{r}) = \mu_B\left(n^{\uparrow}(\underline{r}) - n^{\downarrow}(\underline{r})\right) \qquad (2.2.15)$$

The magnetic polarisation can be defined by:

$$\xi(\underline{r}) = \frac{\frac{1}{\mu_B}|m(\underline{r})|}{n(\underline{r})} \qquad (2.2.16)$$

So that $0 \leq \zeta \leq 1$. The following contribution to the total energy results:

$$E_c^{LSDA}[n,\xi] = \int\left[\varepsilon_c^U(n(\underline{r})) + f(\xi(\underline{r}))\left(\varepsilon_c^P(n(\underline{r})) - \varepsilon_c^U(n(\underline{r}))\right)\right] n(\underline{r})d\underline{r} \qquad (2.2.17)$$

Where f(ζ) is a smooth interpolating function with f(0) = 0 and f(1) = 1. The functionals $\varepsilon_c^P$ and $\varepsilon_c^U$ represent the correlation energy densities for the polarised and unpolarised systems respectively. This study uses the correlation functional of Vosko *et al.* (1980), which has met with considerable success in the description of a wide range of bulk materials (e.g. Clerc, 1998; Gibbs *et al.*, 2005; Zope & Blundell, 2001).

The contribution to the Kohn-Sham potential from the exchange and

correlation functionals described so far correspond to an *effective* magnetic field. By calculating the first derivatives of these quantities with respect to the spin polarised charge densities, we obtain a first term, equal for the two spin polarisations, and a second term (depending upon the magnetisation) which has the same absolute value for both but changes sign according to the spin to which it is applied. This latter term introduces differences in the two effective fields, thus producing the spin imbalances from which the magnetic properties of the system emerge.

The L(S)DA has met with much success in the description of certain materials, particularly simple (nearly-free electron like) metals (Callaway & Wang, 1977), ionic solids (de Boer & de Groot, 1999) and covalent semiconductors (Salehpour & Satpathy, 1989). However, the L(S)DA has difficulty predicting the correct bond energies and bond lengths, often calculating lengths considerably shorter than those found in experiment (Ballone & Galli, 1990). There were also major discrepancies from experiment for some material properties, most notably the inability to predict the ferromagnetic ground state in bcc Fe (Wang *et al.*, 1985). This prompted refinement of the LDA, and the development of the generalised gradient approximation (GGA).

### 2.2.5 Generalised Gradient Approximation (GGA)

An extension to the exchange-correlation energy approximation is offered by the GGA, which attempts to account for inhomogeneities within the electron density of real materials by including consideration of "local" gradients in the electron density. In order to account for non-uniform electron densities, the chosen exchange-correlation energy functional must depend in some way upon the electron density gradient $\nabla n(\underline{r})$. The inclusion of the GGA introduces the following term into the $E_{xc}$ functional:

$$E_{xc}^{GGA}[n] = \int \varepsilon_{xc}^{GGA}\left(n(\underline{r}), \left|\nabla n(\underline{r})\right|\right)\, n(\underline{r}) d\underline{r} \qquad (2.2.18)$$

which can be adjusted to include the spin populations:

$$E_{xc}^{GGA}[n_{\uparrow}, n_{\downarrow}] = \int \varepsilon_{xc}^{GGA}\left(n_{\uparrow}(\underline{r}), n_{\downarrow}(\underline{r}), \nabla n_{\uparrow}(\underline{r}), \nabla n_{\downarrow}(\underline{r})\right)\, n(\underline{r}) d\underline{r} \qquad (2.2.19)$$

Several different formulations of the GGA exchange-correlation functional have been described (Filippi *et al.*, 1994), which can be divided into two broad categories:

(i) "Semi-empirical" GGA functionals, such as BLYP. These are comprised of electron density terms with adjustable parameters, fitted to a range of experimental data. Such functionals have proved successful in the description of molecules and clusters (Boese & Handy, 2001).

(ii) "Parameter-free" GGA functionals that have been derived from first principles, based upon the LDA. Such functionals have proven to be very successful in the description of bulk materials. Calculations within this report use Perdew and Wang's PW91 functional (Perdew & Wang, 1991).

In addition, hybrid functionals have also been developed which include a fraction of Hartree-Fock exact exchange, such as B3LYP (Glukhovtsev *et al.*, 1997).

The GGA has achieved some significant successes in correctly predicting the properties of some non-homogeneous systems, most notably in the correct prediction of the ferromagnetic bcc ground state in bulk iron, where LDA incorrectly predicts a paramagnetic fcc structure (Ahuja *et al.*, 1994).

Even with this refinement, however, DFT still has great difficulty dealing with the so-called "strongly correlated" materials, where a large degree of electron localisation occurs. It has been theorised that this is at least partly caused by the uniform electron gas description on which LDA is based, which is incommensurate with strongly bound valence electrons (Amador *et al.*, 1992). In response to this

failure of the GGA for some materials (particularly transition metal oxides), further modifications to the exchange-correlation functional have been proposed.

### 2.2.6 Hubbard U Correction

Highly-correlated materials, where interactions between moving electrons account for an important fraction of the total system Hamiltonian, are difficult to describe using the GGA method. Highly-correlated materials tend to consist of elements with electrons that occupy 3*d*, 4*f* or 5*f* orbitals (Kotliar *et al.*, 2006), implying that the transition metals, actinides and lanthanides pose particular problems for DFT. Transition metal oxides in particular tend to be subjected to strong on-site electron-electron repulsions in the 3*d* band, with the narrow bandwidth a decisive factor.

One method that has been proposed to deal with failures in the description of highly-correlated materials in the GGA is the so called GGA+U approximation, for which different formulations have been devised (Anisimov *et al.*, 1991; Ebert *et al.*, 2003). Whichever form is taken, the core concept is to correct the LSDA or GGA with a mean-field, Hubbard-like term (Hubbard, 1963), designed to improve the description of the electron correlations relating to on-site coulomb repulsions. A further correction term is also included to treat any "double counting" of contributions. Thus the U term can be thought of as an additional energy contribution, taken from the model Hamiltonians that represent the framework within which normal band theories treat strongly correlated materials. Anisimov and co-workers (Anisimov *et al.*, 1991; Anisimov *et al.*, 1993; Solovyev *et al.*, 1994) introduced a basis-set independent formulation of GGA + U, where the energy functional takes the form:

$$E = E_{LDA} + \sum_{I}\left[\frac{U}{2}\sum_{m,\sigma\neq m',\sigma'} n_{m}^{I\sigma} n_{m'}^{I\sigma\sigma} - \frac{U}{2} n^{I}\left(n^{I}-1\right)\right] \qquad (2.2.20)$$

where $n_m^{I\sigma}$ and $n_{m'}^{I\sigma\sigma}$ are generalised atomic orbital occupations for the "Hubbard" atom (the atom with strongly correlated electrons) at site I, $n^I = \sum_{m,\sigma} n_{m\sigma}^I$, and U is the Hubbard parameter describing the on-site correlations. Using this equation to derive the orbital energy with respect to the orbital occupation gives:

$$\varepsilon_{m\sigma}^I = \frac{\partial E}{\partial n_m^{I\sigma}} = \varepsilon_{m\sigma}^{0I} + U\left(\frac{1}{2} - n_m^{I\sigma}\right) \qquad (2.2.21)$$

where $\varepsilon^0$ is the corresponding LDA quantity. It is evident that a gap of width ≈ U opens between occupied ($n_i^I \approx 1$) and unoccupied ($n_i^I \approx 0$) orbitals.

This scheme was further developed to take account of the possible non-spherical character of the effective interactions (the dependence of U on the magnetic quantum number m) and the exchange coupling. To solve these problems, and the further issue of making the theory rotationally invariant, a further formulation of GGA + U was introduced (Liechtenstein *et al.*, 1995) (Anisimov *et al.*, 1997) and further developed into Dudarev's approach (Dudarev *et al.*, 1998). This treats the on-site Coulomb interaction energy as:

$$E_U = \frac{\left(\overline{U} - \overline{J}\right)}{2} \sum_{\sigma} \left[ \mathrm{Tr}\left(n^{\sigma}\right) - \mathrm{Tr}\left(n^{\sigma} n^{\sigma}\right) \right] \qquad (2.2.22)$$

where $n^\sigma$ is the density matrix of the *d* electrons, σ is a spin index and $\overline{U}$ and $\overline{J}$ are the spherically averaged matrix elements of the screened Coulomb and exchange interactions respectively. Only the difference $U_{eff} = (\overline{U} - \overline{J})$ is considered meaningful. A summary of the mathematical framework of this model is given by Rohrbach *et al.* (2003).

A drawback of the $U_{eff}$ functional is that it is rarely possible to determine its value from any first-principle methods, and instead its value must be determined by agreement with experiment, in a semi-empirical way (Novák *et al.*, 2001]. In this

study, a range of $U_{eff}$ values will be tested for the materials simulated, and the results compared with empirically determined parameters to find the best agreement with experiment.

### 2.2.7 Periodic Systems

The description of bulk materials within DFT is based upon the assumption that the atoms are (at least within the Born-Oppenheimer approximation) at rest in their equilibrium positions and form an infinitely repeating structure of basic units. In mathematical terms the potential experienced by the electrons due to the ion cores may be represented by:

$$V(\underline{r} + \underline{R}) = V(\underline{r}) \qquad (2.2.23)$$

where $\underline{R}$ is a direct lattice vector corresponding to an integer linear combination of three fundamental vectors, which determine the periodicity of the lattice in three independent directions. The entire electronic Hamiltonian also shares the translational invariance of the lattice, which permits the application of the Bloch theorem (Bloch, 1928):

$$\psi_{\underline{k}v}(\underline{r}) = e^{i\underline{k}\bullet\underline{r}} u_{\underline{k}v}(\underline{r}) \qquad (2.2.24)$$

where $\underline{k}$ is the crystal momentum of the electrons, *v* is the band index classifying all states corresponding to the same $\underline{k}$-vector and $u_{\underline{k}v}(\underline{r})$ is a function with the same periodicity as the crystal:

$$u_{\underline{k}v}(\underline{r} + \underline{R}) = u_{\underline{k}v}(\underline{r}) \qquad (2.2.25)$$

The k-vectors are defined within the first Brillouin zone (BZ) of reciprocal space. This is a periodic structure of reciprocal lattice vectors, represented by $\underline{b}_i$, and is related to the real lattice vectors according to:

$$\underline{b}_i \bullet \underline{u}_j = 2\pi\, n \qquad n = 1, 2, 3\ldots \quad i,j = 1, 2, 3 \qquad (2.2.26)$$

The summations over electronic states which define many physical quantities, for instance the band energies, $E_{band}$, and the electron density, $n(\underline{r})$, actually correspond to integrals over the BZ. Due to the translational invariance of the system, different $\underline{k}$-points can be treated independently. Further, the symmetry of the crystal means that the integration can conveniently be confined to a smaller region of the BZ, named the irreducible wedge of the Brillouin zone (IBZ). This model can be further refined by the use of the special point integration technique, which allows the use of reciprocal space integration using a small set of k-vectors in the IBZ. These points may be chosen according to different formalisms, but for all calculations in this report the Monkhorst-Pack algorithm is used (Monkhorst & Pack, 1976), which is a rectangular grid of points spaced evenly through the BZ.

The special points technique encounters some difficulties when applied to metals, since the region around the Fermi energy needs to be sampled accurately; in general a larger number of sampling points is required to determine the partial occupancy present in these bands. This issue can be addressed by introducing a finite "smearing" of the Fermi distribution, with the effect of smoothing the weight of the states around this level and in turn avoiding large fluctuations in the calculated quantities. A variety of convoluting functions can be chosen (Methfessel & Paxton, 1989), which are specified in this report as they are applied. These include Gaussian smearing (finite-temperature smearing) and the tetrahedron method with Blöchl corrections (Blöchl, 1994). The first of these methods uses a Gaussian function with a width given by a parameter, the smearing parameter. This smearing can be considered in the form of a finite temperature DFT method (Mermin, 1965) where the variational quantity is the electronic free energy. Phonon calculations use the convoluting function and smearing method of Methfessel and Paxton (1989).

Ionic relaxations are undertaken after each electronic relaxation step as required. The minimisation proceeds via a conjugate-gradient technique (Press *et al.*, 1986).

### 2.2.8 Plane Wave Basis Sets

In order to solve the Kohn-Sham equations, the electronic wavefunction need to be built from simpler functions, termed the *basis set*. VASP uses a plane-wave basis set (Pickett, 1989) and implements efficient algorithms such as fast Fourier transforms (FFTs) to move between real and reciprocal space. In this formulism the Bloch electronic wavefunction takes the form:

$$\psi_{\underline{k}v}(\underline{r}) = \frac{1}{\sqrt{(N\Omega)}} \sum_{\underline{G}} e^{i(\underline{k}+\underline{G})\bullet\underline{r}} c_v(\underline{k}+\underline{G}) \qquad (2.2.27)$$

where $\Omega$ is the volume of the unit cell, N is the number of electrons, $\underline{G}$ represents the reciprocal lattice vectors, and the $c_v(\underline{k}+\underline{G})$ coefficients are normalised in such a way that:

$$\sum_{\underline{G}} \left| c_v(k+G) \right|^2 = 1 \qquad (2.2.28)$$

Using this expansion, the Kohn-Sham equations can be written in reciprocal space format:

$$\sum_{\underline{G}'} \left[ \frac{\hbar^2}{2m} \left| \underline{k}+\underline{G} \right|^2 + v_h(\underline{G}-\underline{G}') + v_{xc}(\underline{G}-\underline{G}') + v_{ext}(\underline{G},\underline{G}') \right] c_v(\underline{K}+\underline{G}') = \varepsilon_{\underline{k}v} c_v(\underline{k}+\underline{G}) \qquad (2.2.29)$$

This equation demonstrates that the Hamiltonian has block diagonal form with respect to the $\underline{k}$ vectors, and the diagonalisation can be performed within each of these blocks separately. For each k-point, only a finite number of the lowest-energy electronic states on which all the electrons of the system can be accommodated need to be

computed to obtain the charge density. This quantity is then used to construct a new "guess" of the potential to be reintroduced into the Kohn-Sham equations for the next step of the iterative diagonalisation.

The plane wave expansion is exact in the limit of an infinite number of $\underline{G}$-vectors. In practical calculations an energy cut-off is chosen, which can be thought of as including only the plane waves inside a sphere of maximum kinetic energy $E_{cut}$:

$$\frac{\hbar^2}{2m}\left|\underline{k}+\underline{G}\right|^2 \leq E_{cut} \qquad (2.2.30)$$

Thus when $E_{cut}$ is fixed, all the wavefunctions of the system whose variation takes place over distances larger than (and up to) $2\pi\hbar/\sqrt{2mE_{cut}}$ can be well described.

A drawback of the plane-wave approach lies in its uniform resolution throughout all regions. This means that the description of ionic cores and the electronic states partially localised around them, require an impossibly great number of $\underline{G}$ vectors. This problem is avoided through the application of pseudopotentials.

### 2.2.9 Pseudopotentials

By assuming that the relevant properties of a chemical system are attributable to the valence electrons only, and that the ionic cores (the nuclei and core electrons) are frozen in their configurations, the atoms themselves may be split into these two regions. The valence electrons are considered to move in an effective potential produced by the ionic cores, and the pseudopotential attempts to reproduce the interaction between the true atomic potential and the valence states without explicitly including the core states in the DFT calculation.

In this thesis we have utilised the projector-augmented wave (PAW) method in

order to account for ion-valence electron interactions. This formulism considers that the ion-electron system is composed of atomic orbitals and a set of "envelope functions" which describe the spaces between the atoms. The Fe pseudopotential considers the [Ne] inner electrons of the Fe atom, meaning that only the outer $3d^6$ and $4s^2$ are considered as valence electrons described using plane waves, whilst the S pseudopotential describes the inner $1s^2$ $2s^2$ $2p^6$ electrons, leaving only the outer $3s^2$ and $3p^4$ to be represented by plane waves.

The implementation of the GGA+U method in the PAW scheme is summarised in Rohrbach *et al.* (2003) and VASP follows the adaptation of Kresse and Joubert (1999).

### 2.2.10 Determining Elastic Constants

Elastic constants relate a stress applied upon a crystal lattice to the resulting strain. Each elastic constant, $c_{ij}$, is defined as the second derivative of the energy density with respect to strain components:

$$c_{ij} = \frac{1}{V}\frac{\partial^2 E}{\partial\varepsilon_i \partial\varepsilon_j}\bigg|_0 \qquad (2.2.31)$$

Where V is the volume of the unit cell, E is the internal energy of the unit cell, and $\varepsilon_i$ and $\varepsilon_j$ are lattice strain components. The tensor of elastic constants takes the form:

$$\begin{pmatrix} c_{11} & c_{21} & c_{31} & c_{41} & c_{51} & c_{61} \\ c_{12} & c_{22} & c_{32} & c_{42} & c_{52} & c_{62} \\ c_{13} & c_{23} & c_{33} & c_{43} & c_{53} & c_{63} \\ c_{14} & c_{24} & c_{34} & c_{44} & c_{54} & c_{64} \\ c_{15} & c_{25} & c_{35} & c_{45} & c_{55} & c_{65} \\ c_{16} & c_{26} & c_{36} & c_{46} & c_{56} & c_{66} \end{pmatrix}$$

This may be simplified for a tetrahedral lattice, such as that of mackinawite, using

symmetry considerations. This becomes:

$$\begin{pmatrix} A & B & C & 0 & 0 & 0 \\ B & A & C & 0 & 0 & 0 \\ C & C & D & 0 & 0 & 0 \\ 0 & 0 & 0 & E & 0 & 0 \\ 0 & 0 & 0 & 0 & E & 0 \\ 0 & 0 & 0 & 0 & 0 & F \end{pmatrix}$$

Where

$$A = c_{11} = c_{22}$$
$$B = c_{12} = c_{21}$$
$$C = c_{13} = c_{23} = c_{31} = c_{32}$$
$$D = c_{33}$$
$$E = c_{44} = c_{55}$$
$$F = c_{66}$$

Of these constants, the most important with respect to experimental effects are those represented by A and B.

Focusing upon the determination of the constants A and B, consider a strain matrix of size (3x3):

$$\varepsilon = \begin{pmatrix} \delta_{11} & \delta_{21} & \delta_{31} \\ \delta_{12} & \delta_{22} & \delta_{32} \\ \delta_{13} & \delta_{23} & \delta_{33} \end{pmatrix} \qquad (2.2.32)$$

In order to determine the constants A and B, two different strains must be applied. In the case of A, the appropriate tensor takes the form:

$$\varepsilon = \begin{pmatrix} \delta & 0 & 0 \\ 0 & 0 & 0 \\ 0 & 0 & 0 \end{pmatrix} \qquad (2.2.33)$$

Where $\delta = \frac{a'}{a}$ is the dimensionless strain ratio, *a'* is the deformed a lattice parameter and *a* is the undeformed a lattice parameter. This strain is depicted in figure 2.2.

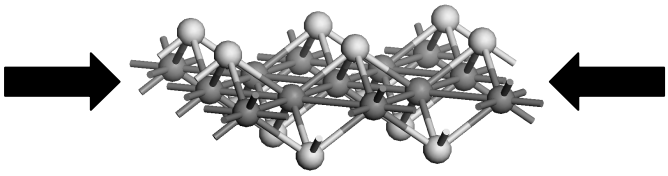

Figure 2.2 – Applied strain on mackinawite structure corresponding to the strain of Equation (2.2.33). The strain is applied in the *a* direction.

The expression for the internal energy of the unit cell as a function of this strain is given by a Taylor expansion about E(0):

$$\begin{aligned} E(\varepsilon( &= E(0) + \tfrac{1}{2}\frac{\partial^2 E}{\partial \varepsilon_1^{\,2}}\bigg|_0 \delta^2 + ... \\ &= E(0) + \tfrac{1}{2} V c_{11} \delta^2 + ..... \\ &= a + b\delta^2 + .... \end{aligned} \tag{2.2.34}$$

Where a and b are the coefficient of a polynomial fit of E versus δ. Thus from Equation (2.2.31):

$$A = \frac{1}{V}\frac{\partial^2 E}{\partial \varepsilon^2}\bigg|_0 = \frac{2b}{V} \tag{2.2.35}$$

The calculation of B requires the following strain matrix to be applied:

$$\varepsilon = \begin{pmatrix} \delta & 0 & 0 \\ 0 & \delta & 0 \\ 0 & 0 & 0 \end{pmatrix} \tag{2.2.36}$$

This strain is depicted in figure 2.3.

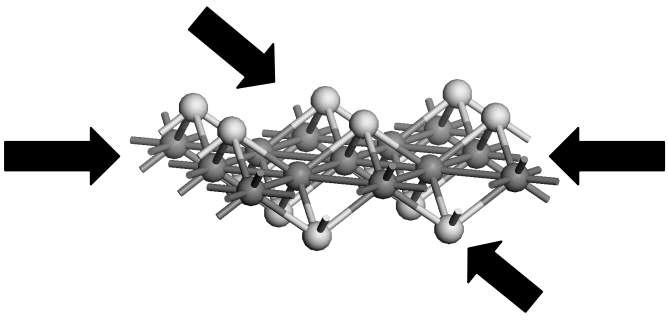

Figure 2.3 – Applied strain on mackinawite structure corresponding to the strain of Equation (2.2.36). The strain is applied in both the *a* and *b* directions simultaneously.

The energy expression associated with the applied strain of Equation (2.2.36) is given by:

$$E(\varepsilon_1, \varepsilon_2) = E(0,0) + V\left(\tfrac{1}{2}c_{11} + \tfrac{1}{2}c_{22} + \tfrac{1}{2}c_{12} + \tfrac{1}{2}c_{21}\right)\delta^2 + \ldots \qquad (2.2.37)$$

From the earlier symmetry considerations, $c_{11} = c_{22}$ and $c_{12} = c_{21}$, and this expression becomes:

$$\begin{aligned} E(\varepsilon_1\varepsilon_2) &= E(0,0) + V\left(c_{11} + c_{12}\right)\delta^2 + \ldots \\ &= a + b\delta^2 + \ldots \end{aligned} \qquad (2.2.38)$$

Thus

$$c_{11} + c_{12} = \frac{b}{V} \qquad (2.2.39)$$

Therefore $c_{12}$ may be found once $c_{11}$ has been determined.

### 2.2.11 Bader Charge Analysis

Calculating the number of valence electrons associated with a particular ion in a periodic solid is a common problem in quantum chemistry. Traditionally, the summation would take place over a sphere with a radius equal to the Wigner-Seitz radius. This method provides a useful guide, however only *s* orbitals can be considered to be spherical in shape, and such spheres are poor approximations to the *p*, *d* and *f* orbitals.

Bader analysis was posited in response to this difficulty (Henkelman *et al.*, 2006). This method considers the electron density around an atom (or ion) as an analytical function, and demarcates the valence electron boundary as the surface where the charge density normal to the boundary is at a minimum. The volume enclosed by this surface is termed the Bader basin, inside of which the electron

density is summed in order to find the Bader charge for that atom. This technique also offers a durable solution to the problem of finding the charge on ions in mixed-valence systems, and can be adapted to magnetic systems; the electronic magnetic moments contained within the Bader basins can be integrated in the same manner as the charge.

### 2.2.12 Magnetic Coupling Parameters

In ordered magnetic materials exchange interactions govern the alignment of neighbouring (or next-nearest neighbouring) magnetic moments. These interactions are quantitatively described using magnetic coupling parameters, termed the exchange constants, $J_{ij}$. Regarding the magnetic interactions of the iron sulfide materials considered in this thesis, by far the most important magnetic interaction is that of *superexchange*, where the magnetic interactions between neighbouring Fe atoms is mediated via the non-magnetic S atoms.

The exchange constants may be calculated by converting spin-polarised DFT results into the magnetic Heisenberg Hamiltonian form:

$$H = E_0 - 2J_{ij}\sum_{\{i,j\}} S_i S_j \qquad (2.2.40)$$

where H is the total internal energy of the system, $E_0$ is the constant paramagnetic energy, the $S_i$ and $S_j$ values for high spin $Fe^{2+}$ are ± 4/2, and the indices {i, j} represent a sum over Fe-Fe pairs. When the interaction is of a ferromagnetic form the $J_{ij}$ parameter must be positive, and for an antiferromagnetic interaction $J_{ij}$ must be negative.

For the case of cubic FeS examined in this thesis, each Fe atom has 12 nearest Fe neighbours, with mediation of the exchange interaction occurring via the

neighbouring S atoms. The form of the Hamiltonian depends on the nature of the interaction between each neighbouring atom. Consideration of the Heisenberg Hamiltonian for Fe-Fe superexchange for three different antiferromagnetic scenarios, denoted by $H_{(1)}$, $H_{(2)}$ and $H_{(3)}$, and the ferromagnetic arrangement $H_{(ferro)}$ leads to four simultaneous equations of the same form as Equation (2.2.40), which describe these scenarios using the exchange constants $J_{12}$, $J_{13}$ and $J_{14}$ and $E_0$ :

$$H_{(ferro)} = E_0 - 2\times\left(\frac{4}{2}\right)^2 4J_{ij} = -32\left(J_{12} + J_{13} + J_{13} - \frac{1}{32}E_0\right)$$

$$H_{(1)} = -32\left(J_{12} - J_{13} - J_{13} - \frac{1}{32}E_0\right)$$

$$H_{(2)} = -32\left(-J_{12} - J_{13} + J_{13} - \frac{1}{32}E_0\right)$$

$$H_{(3)} = -32\left(-J_{12} + J_{13} - J_{13} - \frac{1}{32}E_0\right)$$

solving for $J_{12}$, $J_{13}$, $J_{14}$ and $E_0$ and combining into a matrix equation gives:

$$\begin{pmatrix} J_{12} \\ J_{13} \\ J_{14} \\ E_0 \end{pmatrix} = -\frac{1}{256}\begin{pmatrix} 1 & 1 & -1 & -1 \\ 1 & -1 & -1 & 1 \\ 1 & -1 & 1 & -1 \\ -32 & -32 & -32 & -32 \end{pmatrix}\begin{pmatrix} H_{ferro} \\ H_{(1)} \\ H_{(2)} \\ H_{(3)} \end{pmatrix} \qquad (2.2.41)$$

Where $J_{12}$, $J_{13}$ and $J_{14}$ represent the exchange parameters between the Fe atoms. By rearrangement, $J_{12}$, $J_{13}$, $J_{14}$ and $E_0$ may be found.

The mean-field approximation equation for the Néel temperature is taken from Swendsen (1973), where the cubic FeS structure is type-I face-centred cubic antiferromagnet. Considering only the Fe nearest neighbour interactions gives:

$$T_N^{MFA} = \frac{2}{3}S(S+1)(4J_1 - 4J_2 - 4J_3) \qquad (2.2.42)$$

Finally, it should be mentioned that this thesis does not consider any spin-orbit coupling terms in spin-polarised calculations due to the high computational demand of such calculations.

# 3. Mackinawite

## 3.1 Introduction

The iron sulfide mineral mackinawite (often referred to as tetragonal FeS) was first discovered in Snohomish County, Washington, USA, within the mine that bears its name (Evans *et al.*, 1962; Evans *et al.*, 1964). Mackinawite has been found to be the precursor to the formation of nearly every other iron sulfide (Livens *et al.*, 2004), it is able to form in recent sediments (Berner, 1967), is produced by certain bacteria (Watson *et al.*, 2000) and, more interestingly, is found in active hydrothermal systems on or near mid-ocean ridges (Russell & Hall, 1997). Indeed, this phase of iron sulfide is the first to form in most ambient environments, and anoxic marine sediment pore waters are saturated with respect to disordered mackinawite (Wolthers *et al.*, 2005). Investigations into the chemistry of mackinawite have served to highlight the significance of this phase in many important processes, where its reported ability to capture heavy metal atoms within its octahedral interlayer vacancies (Moyes *et al.*, 2002) and its possible role in the development of proto-metabolism (Russell & Martin, 2004) are particularly interesting.

The synthesis of mackinawite was first reported by Berner (1962, 1964). By immersing reagent grade metallic iron wire in a saturated aqueous solution of $H_2S$, tetragonal FeS was precipitated. This solid phase was reported to possess a black colour when wet, to be soluble in concentrated HCl, to be unattracted by an ordinary

hand magnet and to oxidise rapidly in air to FeOOH (lepidocrocite) and orthorhombic sulfur. Due to this rapid reaction with oxygen the material properties of mackinawite, such as elastic constants and vibrational modes of the crystal lattice, are unknown.

A number of experimental studies on the stability of mackinawite have found that it converts to the more oxidised spinel phase greigite (Lennie *et al.*, 1997), although it has been shown that if mackinawite is kept in a reducing atmosphere devoid of any reactant other than $H_2S$ it is stable and its transition to the greigite phase is inhibited over a wide range of pH and temperature (Benning *et al.*, 2000). The upper limit for the thermal stability of mackinawite is thought to be around 130ºC (Taylor & Finger, 1980). In solution, lattice expansions of up to 54% by volume, relative to crystalline mackinawite, have been observed caused by intercalation of water molecules between the lattice sheets (Wolthers *et al.*, 2005). Recent research has found that mackinawite forms between 1 and 10 ms after the Fe(II) and S(-II) solutions are admixed.

Finally, naturally occurring mackinawite has been reported to be non-stoichiometric, postulated to result from an S deficiency (Kostov & Minceva-Stefanova, 1982). As such its formula is conventionally written $FeS_{1-x}$ (where typically $0 \leq x \leq 0.07$). Synthetic mackinawite has, however, been found to have a formula very close to the stoichiometric end-member FeS (Mullett *et al.*, 2002) and it is likely that poorly formed samples or interstitial Fe explains any non-stoichiometry (Rickard & Luther, 2007).

### 3.1.1 Structure

The structure of mackinawite is that of a distorted cubic-packed array of sulfur atoms, with iron in some of the tetrahedral interstices and vacancies in the larger octahedral

spaces (Taylor & Finger, 1970). This arrangement corresponds to a tetragonal PbO structure. The space group is *p4nmm* (129) (Kuovo *et al.*, 1963), where the iron atoms lie at the centre of slightly distorted tetrahedra with sharing edges, forming sheets stacked along the *c* axis. These sheets are bonded via weak Van Der Waals forces (Figure 3.1).

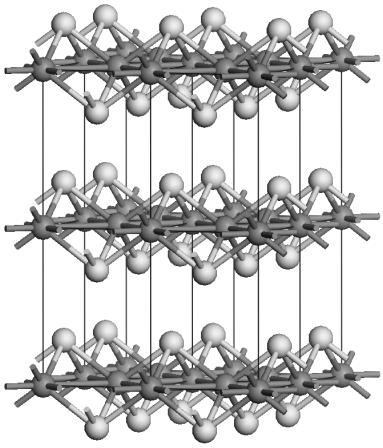

Figure 3.1 – The structure of mackinawite. The iron atoms are represented in dark grey and the sulfur in light grey. Note the close Fe-Fe separation in the basal plane compared to the interlayer distances.

The layered structure is unusual in that it permits very close metal-metal distances in the basal plane (2.485 Å) where the iron atoms are coordinated tetrahedrally to four equidistant sulfur atoms.

Table 3.1 – Summary of experimentally determined values for the lattice parameters of mackinawite.

| Author | a (Å) | c (Å) |
|---|---|---|
| Lennie *et al.*, (1997) | 3.6647 ± 0.0013 | 4.9971 ± 0.0019 |
| Uda, (1968) | 3.68 | 5.04 |
| Mullet *et al.* (2002) | 3.67 | 5.05 |
| Berner, (1962) | 3.679 ± 0.002 | 5.047 ± 0.002 |
| Lennie *et al.* (1995) | 3.6735 ± 0.0001 | 5.0328 ± 0.0001 |

Table 3.1 shows all published experimentally determined values for the lattice parameters of mackinawite. It has been reported that the tetrahedra in stoichiometric mackinawite are very nearly perfect, with Fe-S-Fe angles very close to 109.47° (Lennie *et al.*, 1995).

### 3.1.2 Interstitial Impurities

It has been reported that naturally occurring mackinawite samples frequently contain substantial amounts of other transition metals (Clark, 1970a; Clark, 1970b; Vaughan, 1969), presumed to be present within the large interlayer vacancies of the structure (Vaughan & Ridout, 1971). Such impurities include up to 10% of either Cr or Cu, and up to 20% each of either Co or Ni (Clark, 1970a; Vaughan, 1969; Sarkar, 1971). It is further suggested that these interstitial atoms tend to enhance the stability of the structure (Takeno, 1965; Clark 1966; Takeno & Clark, 1967) It is in regards to the ability of mackinawite to accommodate impurities in the octahedral vacancy sites between layers that applications for this material as a sink for heavy metal atoms has been suggested (Moyes *et al.*, 2002; Mullet *et al.*, 2004; Livens *et al.*, 2004; Liu *et al.*, 2008).

### 3.1.3 Formation and Nucleation of Mackinawite

Taylor (1980) suggested that the homogeneous nucleation of mackinawite is facile, based upon the ease of precipitation of fine-grained (< 1μm) crystals. The formation is thought to proceed by complexation of $Fe^{2+}$ and $SH^-$:

$$Fe^{2+} + SH^- \rightarrow FeSH^+$$

followed by dimerisation polymerisation of $FeSH^+$ with elimination of protons and

water of solvation:

$$2FeSH^{+} \rightarrow Fe_2S_2 + 2H^{+}$$

Tesselation of these $Fe_2S_2$ rings leads to the formation of mackinawite.

### 3.1.4 Experimental Studies

Of all the experimental techniques used to investigate Fe compounds, Mössbauer analysis has proved to be the most useful and versatile for the determination of the electronic structure (X-ray diffraction (XRD) is of course paramount in structural determination) (Vaughan & Craig, 1978). The first Mössbauer study of mackinawite determined the spectra to consist of overlapping magnetic hyperfine patterns (Morice *et al.*, 1969), attributed to impurities and the presence of other sulfide phases in the samples. A more detailed Mössbauer study dealing with more stoichiometric mackinawite was undertaken by Vaughan & Ridout (1971), and confirmed the absence of any internal field, and also indicated that mackinawite is comprised solely of low-spin $Fe^{2+}$. It was further suggested that the *d* electrons in mackinawite may be delocalised extensively in the basal plane, forming metallic bands, and that the close Fe-Fe distances in mackinawite (0.259 nm) give rise to magnetic coupling and the absence of a net magnetisation. The formal oxidation state of iron in the tetrahedral sites is considered to be less than +2 due to this delocalisation. However, it should be mentioned that an earlier study of Bertaut *et al.* (1965) had found no evidence of metallic behaviour.

Mullett *et al.* (2002) characterised a fabricated sample of mackinawite using XRD, transmission electron microscopy (TEM), transmission Mössbauer spectroscopy (TMS) and X-ray photon spectroscopy (XPS). The TEM data showed the Fe:S atomic ratio to be 0.99 with a standard deviation of 0.08, in agreement with

the conventional formula of $FeS_{1-x}$ where $0 < x < 0.07$. The TMS experiments permitted the investigation of the bulk properties of the material, and at room temperature one singlet and two doublets were found in the spectra; this corresponds to a superposition of elemental sub-spectra. This suggests that iron is likely to be present in another oxidation state other than $Fe^{2+}$, presumed to be $Fe^{3+}$. The relative abundance of $Fe^{2+}$ to $Fe^{3+}$ is found to be 4:1. XPS is sensitive only to the sample surface, and it was found that the $Fe^{3+}$ is present chiefly upon the surface of the crystal. It is proposed that the surface of mackinawite possesses a greigite structure (a weathered layer) where some of the $Fe^{2+}$ has oxidised to $Fe^{3+}$, which may be an important consideration in the phase change of mackinawite to greigite. Oxidation from the ferrous state in mackinawite to the ferric state in greigite would be facilitated by electronic conduction along the iron bands in the mackinawite. As the ferrous iron loses electrons, the reduced radius of the ferric iron allows their diffusion, and mackinawite is transformed to greigite (Krupp, 1994). A variety of experimental studies have dealt with the conversion of mackinawite to greigite (Boursiquot *et al.*, 2001; Lennie *et al.*, 1997) and pyrrhotite (Lennie *et al.*, 1995) although the exact mechanisms of each are still unclear.

Berner (1967) studied the solubility product constants and, by derivation, the standard free energy of formation of both mackinawite and greigite, leading to the following reaction paths and values for the free energy transitions:

$$3FeS_{mackinawite} + S_{rhombic} \rightarrow Fe_3S_{4greigite} \qquad \Delta F_{reaction} = -2.5 \text{ kcal/mole}$$

$$Fe_3S_{4greigite} + 3FeS_{mackinawite} \rightarrow FeS_{2pyrite} \qquad \Delta F_{reaction} = -13.5 \text{ kcal/mole}$$

These are solid state reactions at 25°C. However, the reliance of these calculations upon the questionable $G°_f(Fe^{2+}_{(aq)})$ value (Rickard & Luther, 2007) means that these values cannot be completely trusted. Benning (2000) calculated the Gibbs free energy

of formation for greigite and mackinawite as:

| | |
|---|---|
| Greigite ($Fe_3S_4$) | $\Delta G^0_{f,298.15}$ = -273.8 kJ/mol |
| Mackinawite (FeS) | $\Delta G^0_{f,298.15}$ = -87.7 kJ/mol |

These values are thought to be a more reliable guide to formation energies.

An electron diffraction study of mackinawite by Lennie *et al.* (1997) found, for approximately stoichiometric single crystals of mackinawite, patterns consistent with mackinawite lying with its {001} surface parallel to the carbon film substrate onto which it was deposited. The morphology of mackinawite crystals has been studied by Rickard and Ohfuji (2006) who found using selected area electron diffraction (SAED) that, for both freeze-dried and precipitated samples of FeS, the {001} surface is the most stable followed in decreasing stability by the {101}, {200} (equivalent to the {100} surface) and {111} surfaces. The resultant crystals are described as being thin and tabular in form.

### 3.1.5 Computational Studies

In general, computational studies of the iron sulfides have tended to focus on pyrite (e.g. Muscat *et al.*, 2002; de Leeuw *et al.*, 2000). The sole exception is the study of Welz and Rosenberg (1987), who undertook the modelling of iron sulfide tetrahedra using self-consistent linear muffin tin orbital calculations with local density approximations. Describing the tetragonal phase as a planar stack of sheets of edge-sharing tetrahedra, they noted the absence of an iron magnetic moment, in contrast to other iron sulfide tetragonal compounds (e.g. $CuFeS_2$). The Fermi level is seen to cut the continuous Fe 3*d* band, suggesting that the compound is metallic. From a consideration of the electronic contribution of Fe and S to the Fe-S bond, they concluded that there is a low degree of covalent mixing and that this bond is

predominantly ionic. Considering the spin-polarised band structure using the Stoner model of itinerant magnetism (Martin, 1967), where the *d* electrons of a transition metal govern the magnetism, the theory predicts that mackinawite will be non-magnetic. It is suggested that the absence of magnetism is due to some form of Fe-Fe interaction, which causes the low density of states by rearranging the Fe *d* bands in the vicinity of the Fermi level. This conclusion is also suggested by the short Fe-Fe bond length of 2.65 Å (close to the metallic Fe bond length of 2.485 Å). The magnetic behaviour of mackinawite is given as Pauli paramagnetic, where the paramagnetism arises from the magnetic moments associated with the spins of the conduction electrons (usually found in metallic materials).

It is important to note that this study considered only isolated $FeS_4$ tetrahedra, describing compounds with exclusively corner sharing units. For compounds displaying chains of edge-sharing tetrahedral (such as mackinawite) the writers do not have a simple binary compound of a type similar to tetragonal iron monosulfide, indicating that this study is unable to describe mackinawite in a rigorous way. A rigorous quantum mechanical study of mackinawite is clearly desirable in order to study its properties and predict its behaviour.

## 3.2 GGA+U Study of Mackinawite

### 3.2.1 Introduction

The aim of this part of the study is to determine to what degree DFT, in the form of the GGA or GGA+U methodologies as implemented within the VASP code, is capable

of correctly reproducing the known structure and properties of mackinawite. The first section will put particular emphasis upon reproducing the crystal structure and the known electronic and magnetic behaviour of mackinawite. In order to determine the spin-ordered state with the lowest energy, calculations are undertaken for each of three ordered magnetic arrangements:

(i) *non-magnetic* – no initial magnetic moments on either Fe atom in the unit cell, which corresponds to only low-spin Fe present in the structure;

(ii) *ferromagnetic* – magnetic moments of $4\mu_B$ on each Fe atom, aligned in a parallel manner to each other; and

(iii) *antiferromagnetic* – magnetic moments of $4\mu_B$ on each Fe atom, aligned in an anti-parallel manner.

Both ferromagnetic and antiferromagnetic arrangements consider the presence of high-spin Fe only. These calculations are repeated with $U_{eff}$ parameter values of 2 eV and 4 eV in order to investigate the effect of enhanced Fe on-site electron correlation on the model.

Once an acceptable level of accuracy and agreement with experiment has been determined, the model will be used to predict further characteristics of this material, specifically the elastic constants and phonon modes. It will be shown that GGA and GGA+U are incapable of providing an adequate description of the interlayer interaction in mackinawite, but instead are able to offer a very good description of the structure, electronic and magnetic properties of a single mackinawite layer.

### 3.2.2 Preliminary Calculations

The bulk mackinawite structure is modelled using the experimentally determined

structure of Lennie *et al.* (1995), with $a = b = 3.6735$ Å and $c = 5.0328$ Å. A non-spin-polarised singlepoint calculation, where the lattice parameters and ionic coordinates are fixed to the experimentally determined values and only the electronic degrees of freedom are allowed to relax, is used to determine the accuracy of the GGA description.

A dense k-point grid of 11x11x11 was used in conjunction with Gaussian smearing around the Fermi level, with a smearing parameter of 0.02 eV. The electronic convergence was checked and was confirmed when the total free energy change and the band structure energy difference between two ionic relaxation steps are both smaller than $10^{-5}$ eV. With these parameters set, the wavefunction basis set cut-off energy (ENCUT) is varied in order to determine the value at which convergence occurs. The results of these calculations are presented in table 3.2.

Table 3.2 – Internal energy convergence with basis set cut-off energy for the experimental mackinawite structure.

| ENCUT (eV) | Internal Energy (eV) |
|---|---|
| 300 | -26.448 |
| 400 | -26.475 |
| 500 | -26.475 |
| 600 | -26.475 |

These results demonstrate that an ENCUT value of 400 eV is sufficient to ensure convergence of the energy to within 1 meV. Each of these calculations result in very large stresses (greater than 10 GPa) occurring within the unit cell, indicating that the experimental structure simulated here does not represent a minimum on the potential energy surface calculated by DFT.

A relaxation of the ionic internal coordinates was then undertaken for each of the three magnetic arrangements, using the conjugate-gradients method to find the

minimum energy ionic arrangement. The structure as defined by Lennie *et al.* (1995) was again used, along with the same calculation parameters as above and a basis set energy cut-off of 400eV. The non-magnetic case yields a structure with internal energy -26.754 eV and a large internal stress within the unit cell of -2.4GPa. This indicates that relaxation of the ions leads to a decrease in the internal energy of the structure of around 0.28 eV, a substantial reduction which highlights the importance of ionic relaxations in the determination of the final energy of simulated structures.

Further calculations introduce the different possible spin orientations of the magnetic moments present on the two Fe atoms in the unit cell of mackinawite. For magnetic moments aligned in opposing directions (the antiferromagnetic arrangement), ionic relaxation followed by an electronic singlepoint calculation finds that the structure is unable to support an antiferromagnetic spin arrangement. Instead, the resulting structure possesses no magnetic moments on the Fe atoms and has the same energy and ionic coordinates as the non-magnetic starting arrangement. For an initial magnetic arrangement in which the magnetic moments on both Fe atoms are parallel (the ferromagnetic arrangement), the calculation also converges to the non-magnetic solution. If the magnetic moments are fixed to 4 on each Fe atom, the same calculations result in a ferromagnetic solution with an internal pressure of 9.6 GPa, indicating very large stresses within the unit cell. The internal energies of these calculations are given in table 3.3. The non-magnetic arrangement is more stable by 1.7 eV, a considerable margin, and the fact that all calculations converge to this arrangement unless forced otherwise suggests this is by far the preferred magnetic state for the system.

Table 3.3 – Internal energies (IE), magnetic moment (MM) on the Fe atoms and residual internal stress (IS) of the unrelaxed mackinawite structure for both non-magnetic and ferromagnetic arrangements.

| | IE (eV) | Fe MM ($\mu_B$) | IS (GPa) |
|---|---|---|---|
| **Non-Magnetic** | -26.475 | - | -2.4 |
| **Ferromagnetic** | -24.782 | 3.36 | 9.6 |

These results confirm that a method for relaxing both the unit cell and the internal coordinates is required in order to determine the mackinawite ground state structure.

### 3.2.3 Unit Cell Relaxation Calculations

For a great many bulk materials it is possible to perform a full relaxation of the unit cell (both shape and volume, via the three lattice parameters and three angles between each) together with the internal coordinates at an increased basis set energy cut-off (in order to avoid any Pulay stresses on the cell) to obtain the ground state ionic structure. We have performed such a procedure on the experimentally determined mackinawite unit cell, with the same calculation parameters as before but with an increased basis set energy cut-off value of 520 eV. Performing this calculation for the non-magnetic, ferromagnetic and antiferromagnetic arrangements, it is found that, as before, all simulations converge to the non-magnetic arrangement. The ferromagnetic structure can only be simulated by forcing the magnetic moments into parallel alignment, each with an initial magnetic moment of 4 $\mu_B$. This results in a structure with an internal energy over 1.6 eV higher than the non-magnetic case, and a magnetic moment on each Fe atom of 3.46 $\mu_B$, summed over the calculated Fe bader volume. The resultant

structures are described in table 3.4.

Table 3.4 – Final structural parameters, S atom coordinate, Fe magnetic moment (MM) and internal energy (IE) of the mackinawite cell for non-magnetic (NM) and ferromagnetic (FM) arrangements. The experimental structure of Lennie *et al.* (1995) is also given.

| | **NM** | **FM** | **Exp.** |
|---|---|---|---|
| **a (Å)** | 3.599 | 3.917 | 3.6735 |
| **b (Å)** | 3.599 | 3.917 | 3.6735 |
| **c (Å)** | 5.625 | 5.762 | 5.0328 |
| **S coordinate** | 0.2162 | 0.2310 | 0.2602 |
| **MM ($\mu_B$)** | - | 3.46 | - |
| **IE (eV)** | -26.821 | -25.190 | - |

These results demonstrate that a full cell relaxation calculation is unable to adequately describe the attractive dispersive forces between the layers, instead leading to an underbinding effect between the layers and a resultant overestimation of the *c* lattice parameter and an underestimation of the S coordinate, which is the fractional position of the first S atom in the *z*-direction. It is also possible that due to unphysical inter-layer interactions (those that cannot reasonably be expected to arise from dispersive forces) there is an associated slight underestimation of the *a* and *b* lattice parameters. When the structure is forced to become ferromagnetic the predicted *a* and *b* lattice parameters increase by around 9%, and the *c* parameter also shows an increase, suggesting that the presence of magnetic ordering radically affects the structure.

This calculation highlights a very important caveat to the use of DFT techniques, namely the difficulty in describing the dispersive forces acting between atoms or molecules. It is well known that the majority of DFT methodologies fail to take account of these interactions, and the incorrect simulation of the Van der Waal's

forces which act between the layers in mackinawite is a further example of this failure of DFT.

### 3.2.4 Interlayer Distance: GGA

It is clear from the preliminary DFT simulations of the mackinawite structure that a closer inspection of the behaviour of the inter-layer distance is required. To this end, a series of calculations were performed to determine the total energy as a function of the *c* lattice parameter. The *a* and *b* lattice parameters are kept constant at the experimentally determined value of 3.6735 Å, while the *c* parameter is varied between values of 3 Å and 7 Å in intervals of 0.1 Å with a constant unit cell shape and volume for each of these individual calculations. In order to accurately determine the correct internal ionic coordinates for each calculation, two simulations were undertaken for each interval: the first to relax the ions into their lowest energy coordination; these non-spin-polarised calculations use the same calculation parameters as in previous calculations, with a basis set energy cut-off of 400eV. The second calculations take these relaxed structures and relax only the electronic degrees of freedom, to ensure convergence of the internal energy.

Figure 3.2 plots the resulting internal energy versus *c* parameter relationship, and definitively shows that this form of DFT is incapable of correctly predicting the interlayer distance and instead the layers continue to repel one another at the experimentally determined *c* parameter of 5.0328 Å. There is no positive gradient to the energy curve for any *c* parameter simulated, indicating that the layers do not attract each other at any interlayer separation distance in the range tested. This is clearly unphysical and proves that the GGA is unable to account for the attraction between the layers, in accord with previous studies of dispersive forces in DFT

(Kristyán and Pulay, 1994). The next section tests the effect of introducing the $U_{eff}$ parameter into the GGA calculations of the mackinawite structure.

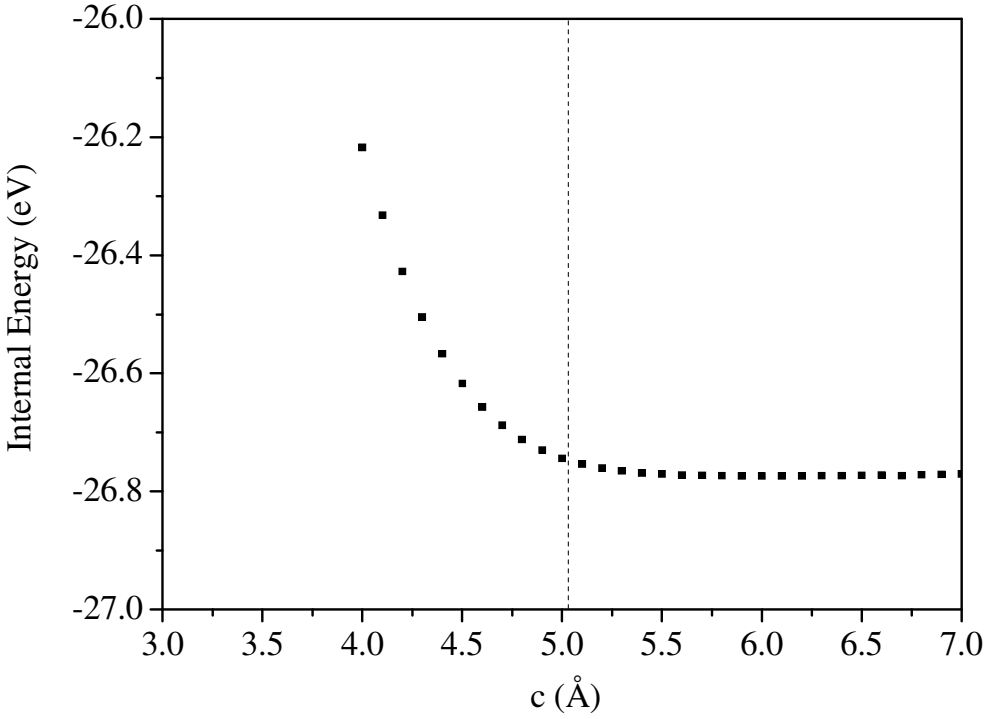


Figure 3.2 – Simulation of the variation of internal energy of the unit cell with the *c* lattice parameter for the non-magnetic GGA calculations for the mackinawite structure. The experimentally determined value for *c* (Lennie *et al.* 1995) is denoted by the dashed line.

### 3.2.5 Interlayer Distance: GGA + U

In order to assess whether the introduction of the Hubbard $U_{eff}$ parameter can aid in the description of the mackinawite structure, four $U_{eff}$ values are tested in full cell relaxations of the mackinawite structure. It has been determined that in Fe oxides a

$U_{eff}$ value of around 4 eV tends to give an optimum description of material properties (Grau-Crespo *et al.*, 2006; Anisimov *et al.* 1997; Piekarz *et al.*, 2007), and so $U_{eff}$ values of 1, 2, 3 and 4 eV are selected, in accord with the observation that correlation effects in sulfides are lower than those seen in the analogous oxides (Rohrbach *et al.*, 2003). All calculations are non-spin-polarised, with an energy cut-off of 520 eV. It is important to note that it is meaningless to compare internal energies between calculations which use differing $U_{eff}$ values, due to the different parameterisations of the Hamiltonian for each.

Tables 3.5 and 3.6 present the results for the fully relaxed non-magnetic and ferromagnetic structures respectively.

Table 3.5 – Predicted lattice parameters and S coordinate for the non-magnetic case with a range of values of the Hubbard $U_{eff}$ parameter

| **$U_{eff}$ (eV)** | **0.0** | **1.0** | **2.0** | **3.0** | **4.0** | **Experimental** |
|---|---|---|---|---|---|---|
| **a (Å)** | 3.599 | 3.589 | 3.586 | 3.580 | 3.565 | 3.6735 |
| **b (Å)** | 3.599 | 3.589 | 3.586 | 3.580 | 3.565 | 3.6735 |
| **c (Å)** | 5.625 | 7.407 | 5.531 | 5.373 | 5.707 | 5.0328 |
| **S coordinate** | 0.2162 | 0.1636 | 0.2178 | 0.2233 | 0.2104 | 0.2602 |

Table 3.6 – Predicted lattice parameters, S coordinate and Fe magnetic moments for the ferromagnetic case with a range of values of the Hubbard $U_{eff}$ parameter

| **$U_{eff}$ (eV)** | **0.0** | **1.0** | **2.0** | **3.0** | **4.0** | **Experimental** |
|---|---|---|---|---|---|---|
| **a (Å)** | 3.917 | 3.799 | 3.926 | 4.078 | 4.124 | 3.6735 |
| **b (Å)** | 3.917 | 3.799 | 3.926 | 4.078 | 4.124 | 3.6735 |
| **c (Å)** | 5.762 | 5.694 | 5.759 | 5.578 | 5.394 | 5.0328 |
| **S coordinate** | 0.2310 | 0.2415 | 0.2345 | 0.2349 | 0.2411 | 0.2602 |
| **Fe MM ($\mu_B$)** | 3.46 | 3.22 | 3.56 | 3.65 | 3.70 | - |

Table 3.5 demonstrates the inability of the $U_{eff}$ parameter to improve the

description of the interlayer interaction in mackinawite for the non-magnetic case. The predicted *a* parameter decreases with increasing $U_{eff}$, away from the experimental value, and the *c* parameter is also incorrectly predicted by a significant margin compared with the experimental value. Table 3.6 shows that the ferromagnetic structure calculations predict *a* parameters and *c* parameters that are too large, for all $U_{eff}$ values tested. For all calculations regardless of the $U_{eff}$ value applied the structure is unable to support an antiferromagnetic arrangement, suggesting that increased electron correlation does not favour an antiferromagnetic arrangement for the mackinawite structure in preference to the non-magnetic case.

### 3.2.6 Fixed Interlayer Distance Calculations

In order to find the most energetically favourable value for the *a* (and *b*) lattice parameter of the mackinawite structure at the experimental interlayer distance, a relaxation of the positions of the ions within the unit cell of mackinawite is undertaken for a range of *a* lattice parameter values. The range chosen is from $a = b =$ 3.4 Å to 4.25 Å, with each measurement taken at an interval of 0.05 Å from the last. These calculations are repeated for the three magnetic arrangements, each simulated with applied $U_{eff}$ values of 0, 2 and 4 eV. The *c* parameter is fixed at the experimentally determined value of 5.0328 Å for all calculations.

Figure 3.3 shows the $U_{eff} = 0$ eV case for the three magnetic arrangements, where the lines correspond to a parabolic fit to each set of data. The non-magnetic case is found to be more stable than the ferromagnetic for all *a* values tested in this case. The minimum energy of the non-magnetic structure corresponds to an *a* lattice parameter of 3.612 Å, in good agreement with the experimentally reported measurement of 3.6735 ± 0.002 Å, an error of less than 2%. The ferromagnetic

solution possesses a minimum in energy at $a$ = 3.972 Å, an overestimation of 10 % compared with the experimentally determined value. The results have been extended for the ferromagnetic case in order to meaningfully show the region around the minimum. It is important to note that the antiferromagnetic and non-magnetic energies are not degenerate; instead the mackinawite unit cell is unable to support an anti-ferromagnetic arrangement of spins on the Fe atoms, and it collapses to the non-magnetic structure.

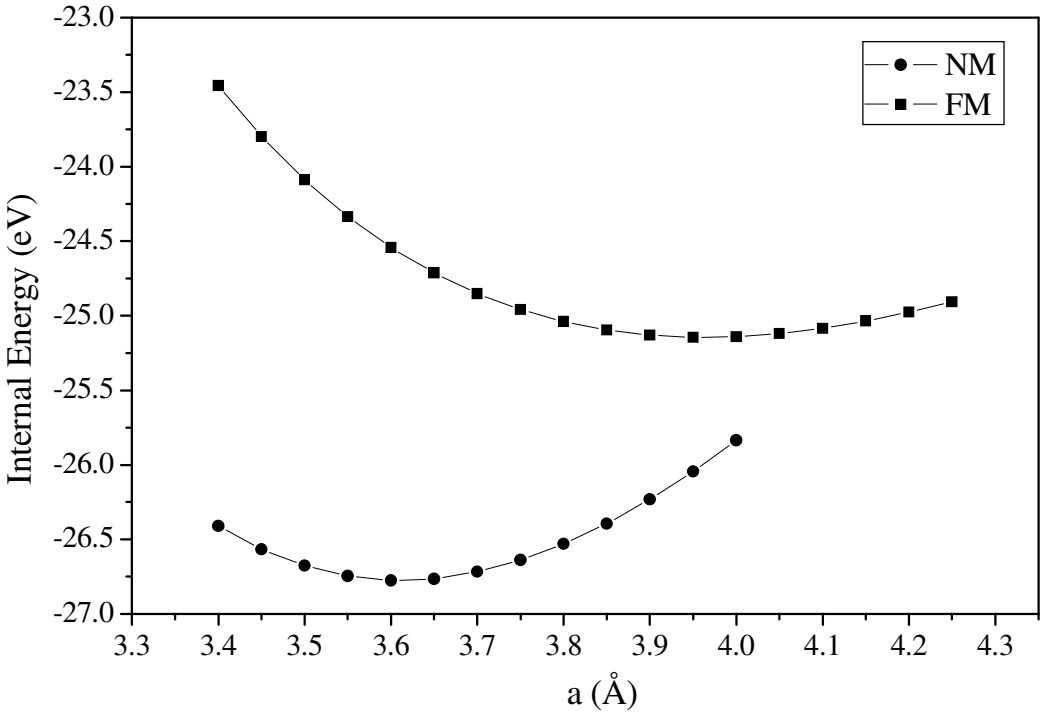


Figure 3.3 – Graph of the variation of the total energy with the $a$ lattice parameter for mackinawite (at fixed $c$ parameter) at $U_{eff}$ = 0 eV.

Figure 3.4 shows that for the case of $U_{eff}$ = 2 eV the non-magnetic case is no longer the lowest energy arrangement. Instead, the antiferromagnetic arrangement possesses the lowest energy, but at a lattice parameter value of 3.85Å and above this arrangement cannot be supported and collapses to the non-magnetic case, in a similar

manner to that seen for the $U_{eff}$ = 0 eV case. Therefore there is no true minimum in the energy for the antiferromagnetic arrangement, which explains the observation in the full geometrical optimisations of the previous section where the antiferromagnetic arrangement cannot be supported. The ferromagnetic energy minimum leads to a structure with a lattice constant *a* of 3.988 Å, a large overestimation compared with the experimental value but very close to the value calculated for the $U_{eff}$ = 0 eV case. In fact, between $U_{eff}$ = 0 eV and 2 eV both the non-magnetic and ferromagnetic cases show little variation in the location of their respective energy minima as a function of the *a* parameter.

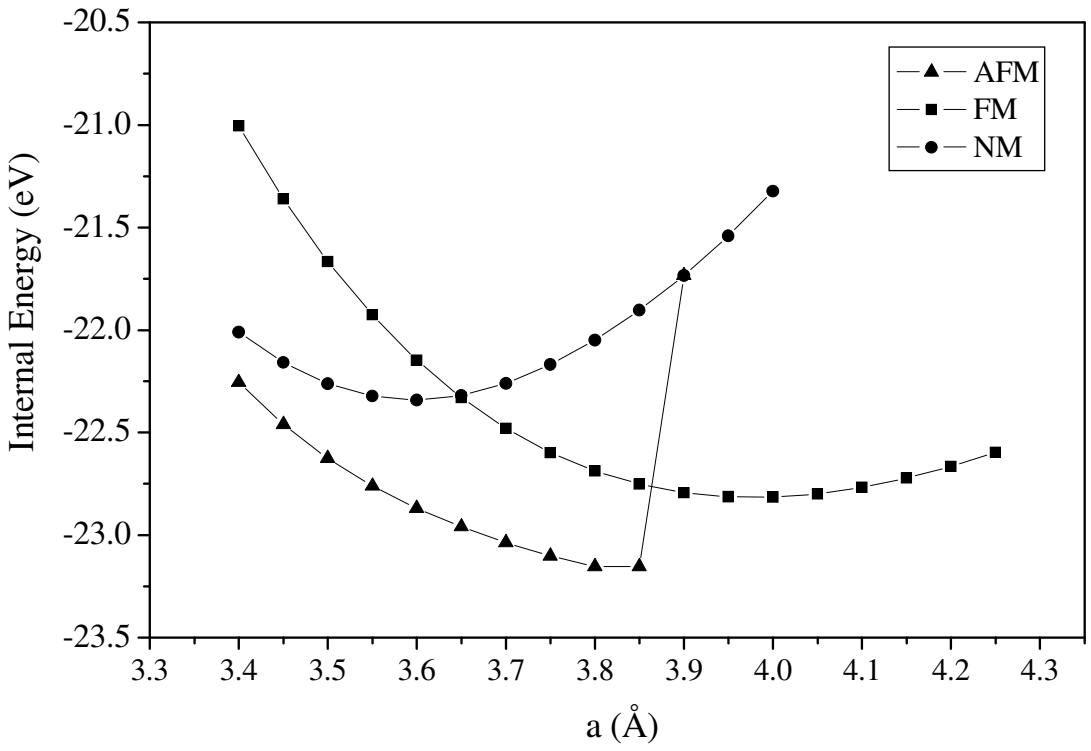


Figure 3.4 – Graph of the variation of the total energy with the *a* lattice parameter for mackinawite (at fixed *c* parameter) at $U_{eff}$ = 2 eV.

Figure 3.5 demonstrates the increasing instability of the non-magnetic case

with increasing $U_{eff}$. Instead, the ferromagnetic case is by far the most stable arrangement when $U_{eff}$ = 4 eV, and predicts a structure with a lattice constant of around 4.2 Å, far greater than that seen experimentally. This suggests that increasing the level of electron correlation favours the ferromagnetic arrangement, and the Fe-Fe distances must increase accordingly, as would be expected from the exclusion principle. As in the $U_{eff}$ = 2 eV case, the structure is unable to support an antiferromagnetic arrangement for any value of *a* greater than around 3.9 Å. The energy difference of 3.2 eV between the non-magnetic and ferromagnetic minimum energies is significant.

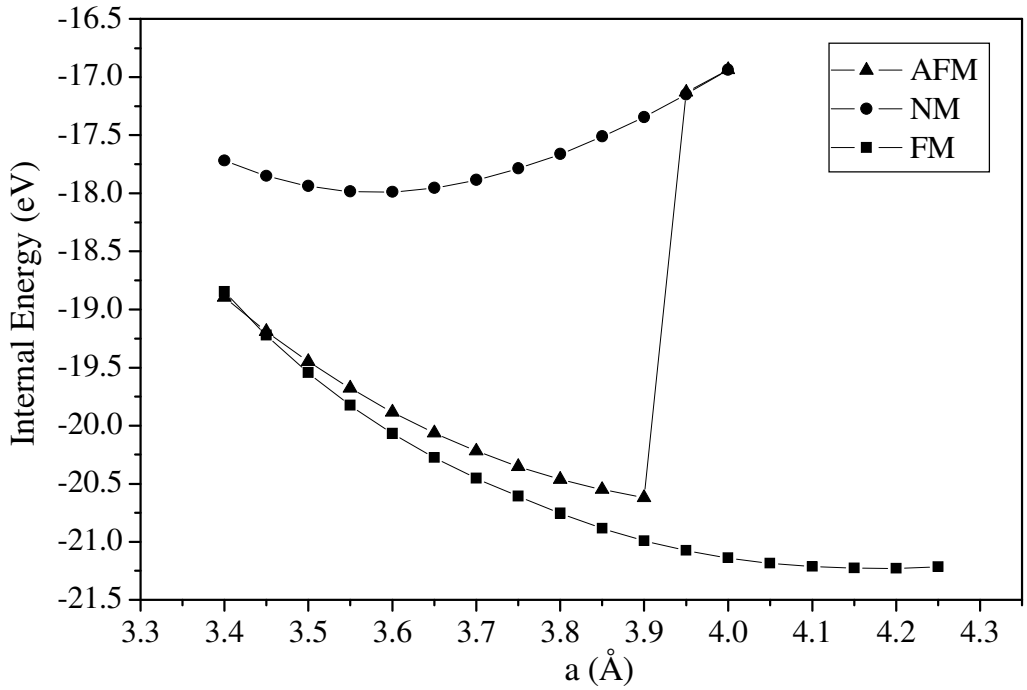


Figure 3.5 – Graph of the variation of the total energy with a parameter for mackinawite (fixed *c* parameter) at $U_{eff}$ = 4 eV

Figures 3.3, 3.4 and 3.5 provide evidence that the most suitable value for $U_{eff}$, that is the value which reproduces the experimental structure and non-magnetic nature

of the individual layers of mackinawite most faithfully, is $U_{eff}$ = 0 eV. The inability of the mackinawite structure to support a stable antiferromagnetic arrangement over a reasonable range of *a* parameters, regardless of the level of electron correlation present, leaves only the non-magnetic and ferromagnetic arrangements for the mackinawite structure. A summary of the minimum locations for each $U_{eff}$ value and magnetic structure is given in table 3.7.

Table 3.7 – Minimum internal energies, *a* lattice parameters, Fe-Fe and Fe-S bond lengths and magnetic moments per Fe atom for the non-magnetic (NM) and ferromagnetic (FM) arrangements, for the $U_{eff}$ = 0, 2 and 4eV cases.

| | **$U_{eff}$ = 0 eV** | | **$U_{eff}$ = 2 eV** | | **$U_{eff}$ = 4 eV** | |
|---|---|---|---|---|---|---|
| | **FM** | **NM** | **FM** | **NM** | **FM** | **NM** |
| **$E_0$ (eV)** | -25.145 | -26.775 | -22.817 | -22.339 | -21.274 | -17.991 |
| **$a_0$ (Å)** | 3.972 | 3.612 | 3.988 | 3.597 | 4.209 | 3.580 |
| **Fe-Fe distance (Å)** | 2.81 | 2.55 | 2.82 | 2.54 | 2.98 | 2.53 |
| **Fe-S distance (Å)** | 2.29 | 2.23 | 2.39 | 2.23 | 2.48 | 2.22 |
| **MM/f.u. ($\mu_B$)** | 4.00 | - | 4.00 | - | 4.00 | - |

Our results show that the calculated relative stability of each arrangement is very sensitive to the $U_{eff}$ parameter applied. For low levels of electron correlation, corresponding to low $U_{eff}$ values, the non-magnetic arrangement is the most stable. For higher values of $U_{eff}$, the ferromagnetic state is more stable. The $U_{eff}$ = 0 eV calculations accurately reproduce the experimentally determined structure of mackinawite, and correctly predict the non-magnetic behaviour. Further, this case predicts an Fe-Fe atomic separation of 2.55 Å and a Fe-S bond length of 2.23 Å, and these values agree very well with the experimentally determined Fe-Fe distance of 2.598 Å and the Fe-S bond distance of 2.256 Å (Lennie *et al.*, 1995). The lack of stability of the non-magnetic arrangement as the electron correlation is increased via the $U_{eff}$ parameter suggests that mackinawite does not require a non-zero Hubbard $U_{eff}$

parameter, and hence that Fe on-site electron correlation is of much lesser importance than in similar simulations of iron oxide materials. In fact, for this case it can be deduced that the $U_{eff}$ parameter is actually detrimental to the description of mackinawite.

A Bader charge analysis of the non-magnetic $U_{eff}$ = 0 eV case is given in table 3.8. The Bader charges for both atoms fall short of the formal oxidation states of these atoms in this coordination. This can be explained by the large degree of covalency associated with the Fe-S bond, where the difference in the oxidation states of the Fe atom and the S atom is 0.30 electrons. This may be compared to an iron oxide such as magnetite, where calculations show a difference in Bader valence of around 0.9 – 1.0 electrons between Fe atoms and O (Wenzel & Steinle-Neumann, 2007).

Table 3.8 – Calculated Bader charges for non-magnetic $U_{eff}$ = 0 eV case in mackinawite.

| Atom | Bader Charge (e) |
|---|---|
| $Fe^1$ | 0.85 |
| $Fe^2$ | 0.85 |
| $S^1$ | -0.85 |
| $S^2$ | -0.85 |

### 3.2.7 Density of States

Further information regarding the electronic structure is provided by the electronic density of states (DOS). Accurate singlepoint calculations were undertaken for both non-magnetic and ferromagnetic arrangements, at $U_{eff}$ values of 0, 2 and 4 eV, using the minimum energy structures determined in the previous section and given in table 3.7. The electronic energy smearing was changed from Gaussian to the tetrahedron method with Blöchl corrections (Blöchl *et al.*, 1994) to improve the DOS description,

since this method has been found to improve the summation of the electronic states in the BZ. Figure 3.6 shows a summary of the DOS for all the stable arrangements found.

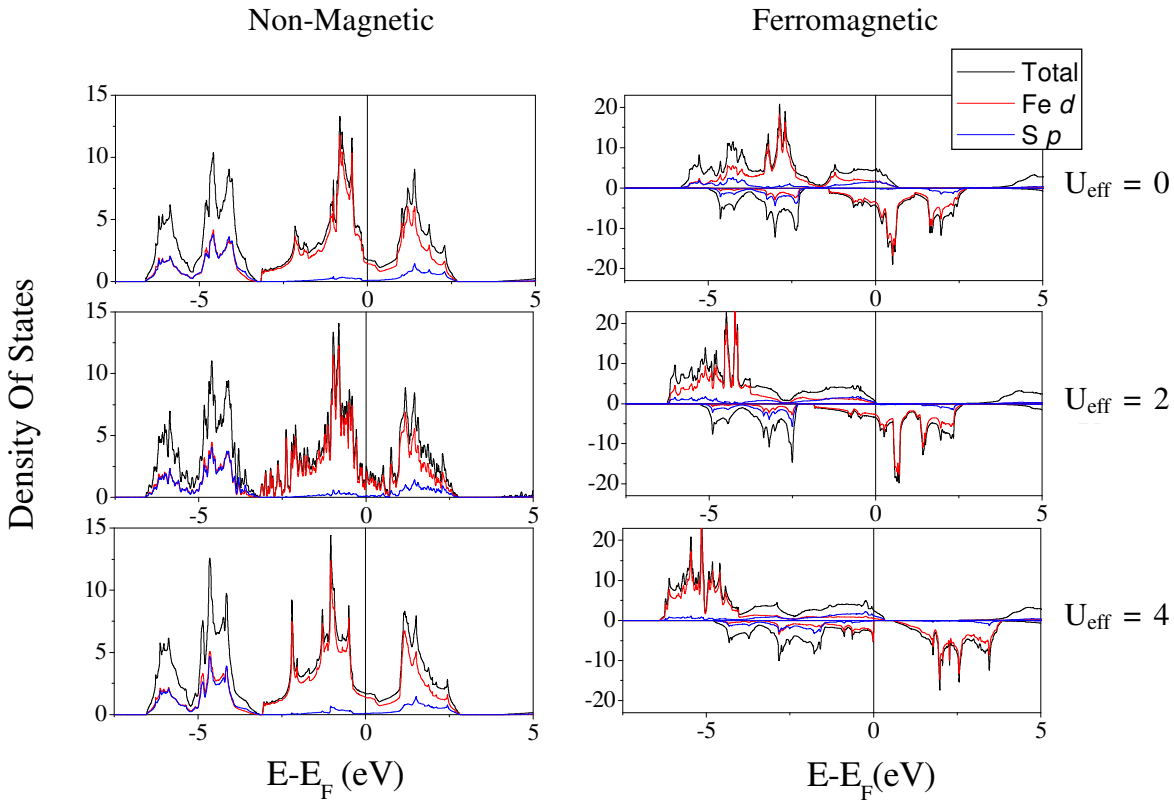


Figure 3.6 – Electronic DOS graphs for non-magnetic and ferromagnetic conditions for each $U_{eff}$ value at T= 0 K. Each graph shows the total DOS and the contributions from the iron *d*-orbitals and the sulfur *p*-orbitals.

The non-magnetic electronic DOS graphs confirm a property hinted at in the literature, namely that mackinawite has a metallic nature in the plane of the layers. The Fermi energy is seen to cut a band of the Fe *d*-orbital roughly in the centre of a local minimum between the $t_2$ and $e$ tetrahedrally split sub-orbitals, indicating the presence of mobile charge carriers. This finding is in agreement with the experimental findings of Vaughan and Ridout (1971). Regardless of the magnitude of the $U_{eff}$

parameter, the non-magnetic DOS has a very similar appearance, indicating that the mackinawite structure is metallic regardless of the amount of electron correlation imposed upon the Fe atoms. The contribution to the DOS at the Fermi level from the S atoms is negligible. This is another success for the $U_{eff}$ = 0 eV simulation, which has correctly predicted the metallic nature of mackinawite within the individual layers.

### 3.2.8 Expanded-Layer Formalism

In order to overcome the problems inherent in the description of the dispersive forces in the mackinawite structure, a new method for relaxing the unit cell is required, which builds upon the successful description of individual layers of the structure. A logical way to proceed involves breaking down the relaxation into parts, beginning with a relaxation of only the *a* (and hence also the *b*) lattice parameters. This is achieved by fixing the *c* parameter to three times that of the experimental value, thereby removing any spurious interactions between the layers which would affect the calculation of second derivative properties of the mackinawite, such as the phonon frequencies. This new structure is depicted in figure 3.7.

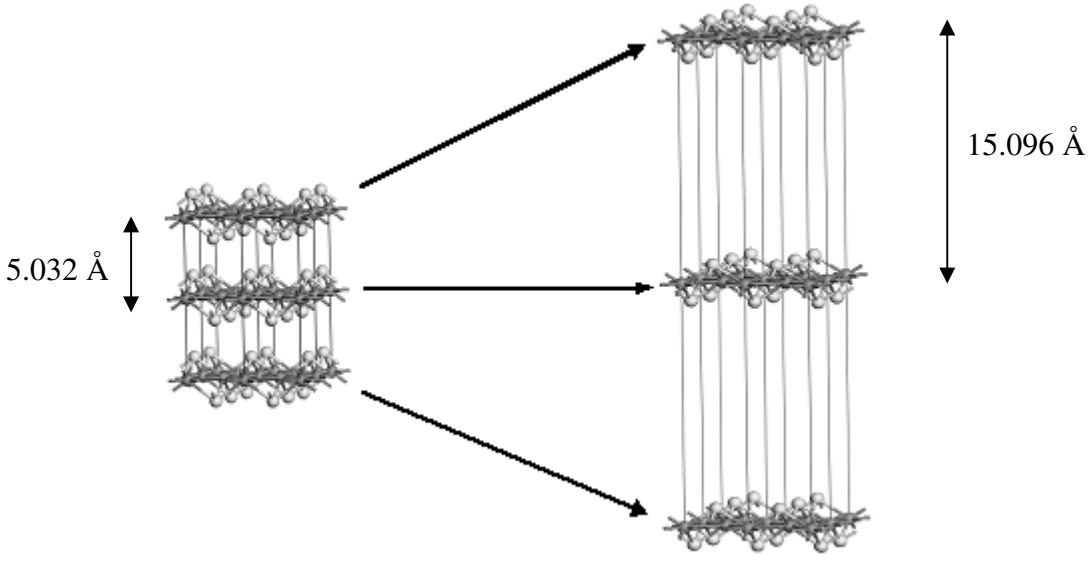

Figure 3.7 – Expanded formulism of the layers within mackinawite in order to remove spurious interlayer interactions. The *c* parameter is tripled.

The Fe-S bond length remains unchanged. Calculations in this formulism can be considered to determine the properties of a single layer of the mackinawite structure *only*.

### 3.2.9 Single-Layer Elastic Constant Calculations

Elastic constants are an important property of any material, relating as they do an applied stress on the crystal lattice to the resultant strain. In order to determine from first principles the elastic constants for the mackinawite crystal, the expanded-layer structure with $U_{eff}$ = 0 eV and no initial applied magnetic arrangement is chosen, due to its excellent agreement with experiment. By conducting only electronic relaxations and refusing to allow the ions to relax, the measured energy density on the unit cell for a given strain (deformation of the lattice) gives the elastic constants, which are found from the second derivative of the energy versus strain on the unit cell (See section 2.2.10).

The calculated elastic constants depend on the direction of the applied strain tensor. A given one-dimensional strain, represented by a dimensionless quantity and denoted by $\delta$, is the ratio of any strained lattice parameter to the equilibrium value. In order to find the minimum of this relation a fitting procedure is used, which fits a parabola to a set of strains and the resultant increase in the internal energy for each discrete value for the applied strain. Figure 3.8 shows the fit to the internal energy versus applied strain for the strain corresponding to Equation (2.2.33) in section (2.2.10). With this fit $c_{11}$ is determined according to Equation (2.2.35):

$$c_{11} = \frac{k_2}{V} = \frac{2 \times 29.66596 \text{ eV}}{202.34 \text{ A}^3} = \underline{\underline{46.9 \text{ GPa}}}$$

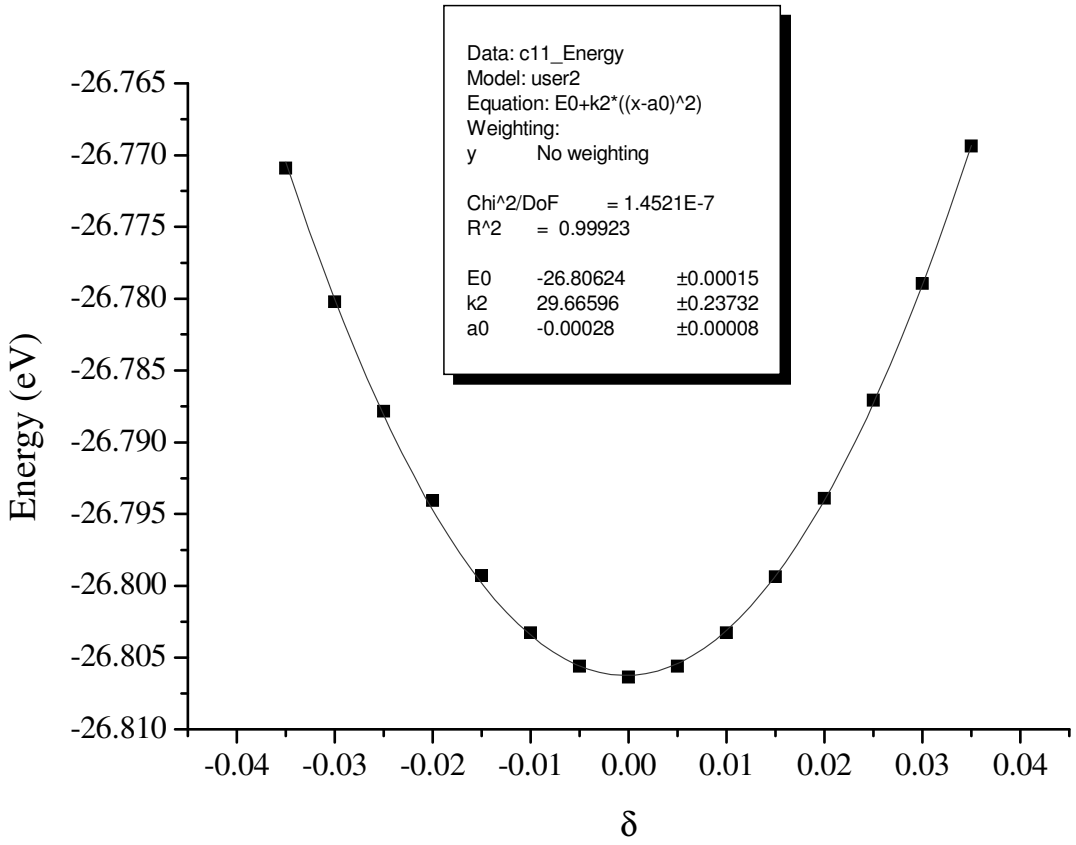


Figure 3.8 – Graph of the fitting of the $c_{11}$ elastic constant to the internal energy of the expanded-layer mackinawite unit cell versus applied strain. The fit is a parabola with equation $E(\delta) = E(0) + k_2(\delta - a_0)^2$, where $k_2$ corresponds to *a* in Equation (2.2.35).

$c_{12}$ is determined by applying a strain in both directions of the plane of the mackinawite layer (See figure 2.3). Figure 3.9 shows the fit to the internal energy versus strain for the applied strain in the form of Equation (2.2.36). With this fit $c_{12}$ can be found from Equation (2.2.39):

$$c_{12} = \frac{k_2}{V} - c_{11}$$
$$= \frac{96.65834 eV}{202.34 A^3} - 0.2932 \ eV\, A^{-3}$$
$$= \underline{\underline{29.5 \ \text{GPa}}}$$

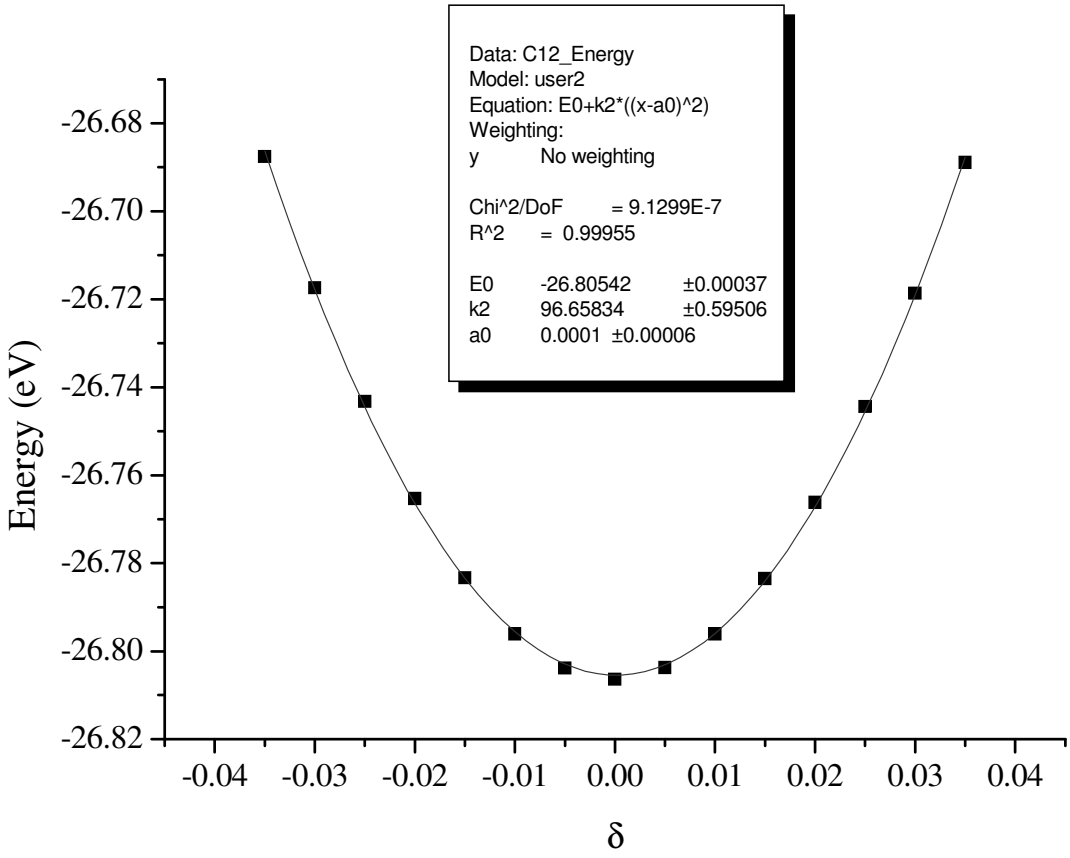


Figure 3.9 – Plot of the fitting of the $c_{12}$ elastic constant. The fit is again a parabola of equation $E(\delta) = E(0) + k_2(\delta - a_0)^2$, where $k_2$ corresponds to *b* in Equation (2.2.39).

### 3.2.10 Single-Layer Phonon Mode Calculations

Phonon modes, the quantized modes of vibration of a crystal lattice, are a very important property of a crystal lattice. Phonon mode calculations on the calculated expanded-layer, non-magnetic $U_{eff} = 0$ eV mackinawite structure are undertaken using

a stringent electronic self-consistent global break condition of $10^{-6}$ eV and an ionic relaxation loop break condition of $10^{-5}$ eV. This allows the accurate calculation of phonon modes for a single mackinawite layer. These are calculated by displacing each of the four atoms in the unit cell in each direction along the Cartesian axes, with displacements of 0.03 Å in both directions.

In these calculations, the Hessian matrix, a matrix of the second partial derivatives of the energy with respect to the atomic positions, is calculated for each of the possible arrangements of atomic displacements. The associated forces on the atoms are found by division by the applicable atomic mass, and from these forces the vibrational frequencies may be found. From the symmetry of the lattice and the fact that the mackinawite unit cell contains four atoms, there are 12 vibrational modes of mackinawite, with the first three corresponding to translational displacement of the entire lattice. The frequencies of these modes are given in table 3.9.

Table 3.9 – Vibrational frequencies of a single layer of mackinawite, found from DFT calculations.

| | |
|---|---|
| **$\nu_1$ (cm$^{-1}$)** | 0 |
| **$\nu_2$ (cm$^{-1}$)** | 0 |
| **$\nu_3$ (cm$^{-1}$)** | 0 |
| **$\nu_4$ (cm$^{-1}$)** | 187 |
| **$\nu_5$ (cm$^{-1}$)** | 267 |
| **$\nu_6$ (cm$^{-1}$)** | 267 |
| **$\nu_7$ (cm$^{-1}$)** | 368 |
| **$\nu_8$ (cm$^{-1}$)** | 377 |
| **$\nu_9$ (cm$^{-1}$)** | 389 |
| **$\nu_{10}$ (cm$^{-1}$)** | 397 |
| **$\nu_{11}$ (cm$^{-1}$)** | 400 |
| **$\nu_{12}$ (cm$^{-1}$)** | 414 |

The first three phonon modes are zero, in accord with their status as translational modes of the lattice. No imaginary modes are observed, which is

encouraging since any imaginary phonon modes for this lattice would imply that the structure is unstable, which is contrary to experimental observations.

### 3.2.11 Summary

This section has examined the modelling of the mackinawite structure using both GGA and GGA+U methods. Preliminary calculations on the unit cell showed that a straightforward relaxation of the ionic and electronic degrees of freedom using the experimentally determined structure fails to find a minimum energy configuration. Indeed, even a full relaxation of the unit cell, including the lattice parameters, predicts an incorrect structure, with a large overestimation of the interlayer distance due to the incorrect treatment of dispersive forces. Simulations leading to a non-magnetic structure yields a configuration with an Fe-Fe distance and *a* and *b* lattice parameters close to those measured experimentally, while forcing a ferromagnetic nature to the structure leads to a large overestimation of the *a* and *b* parameters. An antiferromagnetic magnetic arrangement cannot be supported by the structure. Applying $U_{eff}$ values from 1eV to 4eV has no effect on correcting the problems with the interlayer interaction for any of the magnetic arrangements.

Instead, a range of *a* lattice parameters are tested and the *c* parameter is fixed. It is found that the non-magnetic $U_{eff}$ = 0 eV case gives the best agreement with the experimental structure within the mackinawite layer, and an examination of the electronic density of states of mackinawite indicates that it is metallic in the plane of the layers for this case, with delocalised electrons in the Fe-*d* orbitals explaining the metallic nature. It is likely that the close Fe-Fe distances within the layers of mackinawite give rise to this behaviour.

A new formulism is postulated to model the mackinawite structure. Expanding the inter-layer distance by a factor of three effectively converts the calculations from bulk to a consideration of a single layer of mackinawite only. Using this new unit cell, the elastic constants and phonon modes of a single layer of mackinawite are found

from first principles.

## 3.3 Interatomic Potential Simulations

### 3.3.1 Interatomic Potential Parameter Fitting

Due to the absence of experimentally confirmed, quantified physical data for mackinawite, no potential models exist for this structure in the literature. Indeed, to the authors' knowledge no parameterised potential model between $Fe^{2+}$ and $S^{2-}$ has yet been developed. However, the success of the DFT calculations in the previous section make possible the fitting of interatomic potentials to the structure using the predicted elastic constants and phonon modes for the expanded-layer form of mackinawite and the experimentally determined mackinawite structure itself. The aim is to determine a set of interatomic potentials which successfully reproduce the structures and properties of both the expanded and experimental mackinawite structures to a high accuracy.

A variety of different potential models were tested to determine their suitability for this task. After a great deal of trial and error in the fitting and optimisation of the potentials and their parameters to the properties, a very close fit to the structures and properties is obtained. It was found that a potential term taking into account of the S-Fe-S 3-body "bond-bending" of the covalent bond was not required. Instead, two Buckingham potentials, each modelling the interaction between S-S and Fe-S ions, were sufficient to accurately reproduce the mackinawite structure. A further term includes a shell- and spring- model with an associated spring constant to account for the polarisability of the S atoms.

Table 3.10 presents the derived parameters for the interatomic potential describing mackinawite. The high polarisability of the sulfur atom is evidenced by the small value for the spring constant between the core and shell of 23.0 eV $Å^{-2}$, as compared with the value for k of 62.9 eV $Å^{-2}$ in Fe-O (Lewis & Catlow, 1985).

Table 3.10 – Derived interatomic potentials for the mackinawite structure. An effective cut-off distance of 15 Å is applied to the Buckingham potentials.

| **Buckingham Potential** | **A (eV)** | **ρ (Å)** | **C (eV·Å$^6$)** |
|---|---|---|---|
| Fe-S | 1000.00 | 0.3201 | 0.0 |
| S-S | 9201.82 | 0.3147 | 130.0 |

| **Spring Potential** | **k (eV·Å$^{-2}$)** |
|---|---|
| S core – S shell | 23.0 |

| **Ion Charges** | **Charge (e)** |
|---|---|
| Fe core | +2.000 |
| S core | +1.357 |
| S shell | -3.357 |

Table 3.11 lists the predictions of the structure and elastic constants of mackinawite compared with available experimental data. Table 3.12 presents the properties from the *ab initio* calculations and the interatomic potential simulations of the single layer, compared to experiment. The fitting to structural parameters for both the expanded layer and experimental structures is excellent, as is the fit to the elastic constants and phonon modes.

Table 3.11 – Comparison of interatomic potential calculations and experimental structure for mackinawite.

| | **Potential** | **Experiment** |
|---|---|---|
| **a, b (Å)** | 3.667 | 3.674 |
| **c (Å)** | 5.033 | 5.033 |
| **$c_{11}$, $c_{22}$ (GPa)** | 145.6 | - |
| **$c_{12}$, $c_{21}$ (GPa)** | 99.1 | - |
| **$c_{13}$, $c_{23}$, $c_{31}$, $c_{23}$ (GPa)** | 8.5 | - |
| **$c_{33}$ (GPa)** | 13.0 | - |
| **$c_{44}$, $c_{55}$** | 3.8 | - |
| **$c_{66}$** | 185.8 | - |

Table 3.12 – Comparison of potential model and *ab initio* calculated properties of an isolated layer of mackinawite.

| | **Potential** | ***ab initio*** |
|---|---|---|
| **a, b (Å)** | 3.661 | 3.599 |
| **c (Å)** | 15.098 | 15.098 |
| **$c_{11}$ (GPa)** | 48.6 | 46.9 |
| **$c_{12}$ (GPa)** | 32.5 | 29.5 |
| **$\nu_1$ ($cm^{-1}$)** | 0.00 | 0.00 |
| **$\nu_2$ ($cm^{-1}$)** | 0.00 | 0.00 |
| **$\nu_3$ ($cm^{-1}$)** | 0.00 | 0.00 |
| **$\nu_4$ ($cm^{-1}$)** | 124 | 187 |
| **$\nu_5$ ($cm^{-1}$)** | 191 | 267 |
| **$\nu_6$ ($cm^{-1}$)** | 245 | 267 |
| **$\nu_7$ ($cm^{-1}$)** | 245 | 368 |
| **$\nu_8$ ($cm^{-1}$)** | 302 | 377 |
| **$\nu_9$ ($cm^{-1}$)** | 323 | 389 |
| **$\nu_{10}$ ($cm^{-1}$)** | 323 | 397 |
| **$\nu_{11}$ ($cm^{-1}$)** | 329 | 400 |
| **$\nu_{12}$ ($cm^{-1}$)** | 413 | 414 |

The prediction by the *ab initio* methods of the conductivity of mackinawite suggests that there exists within the Fe basal plane a degree of electron delocalisation, which may be interpreted as a form of metallic bonding between the iron cations. This is not reproduced by the interatomic potential, which provides a possible explanation

for the small discrepancies in elastic constants and phonon modes when compared to the *ab initio* predictions.

### 3.3.2 Surface Geometry and Analysis

Using the interatomic potential derived in the previous section, it is now possible to examine the stability and structure of the surfaces of mackinawite in a rigorous manner. To this end, the crystal structure produced from the interatomic potential calculations was "cut" in a number of different directions to produce the {100}, {010}, {001}, {110}, {101}, {011} and {111} surfaces of mackinawite. The symmetry of the crystal in the *a* and *b* directions leads to the equivalence of the {100} and {010} pair of surfaces, and also the {101} and {011} surfaces. Using the procedure described in section 2.1.2, the unrelaxed and relaxed surface energies predicted by the derived potential are calculated, and these values are presented in Table 3.13. In addition, it should be noted that every one of these surfaces possesses only a single, unique repeat unit each. with the exception of the {001} surface which has two.

Table 3.13 – Unrelaxed and relaxed surface energies for mackinawite, calculated using the derived interatomic potential. The suffixes –S and –Fe denote the termination of a surface at a plane of that species of atoms.

| Surface | 001-S | 011 | 101 | 100 | 010 | 111 | 110 | 001-Fe |
|---|---|---|---|---|---|---|---|---|
| $\gamma_{unrelaxed}$ ($Jm^{-2}$) | 0.07 | 1.14 | 1.14 | 1.25 | 1.25 | 3.35 | 3.72 | 6.41 |
| $\gamma_{relaxed}$ ($Jm^{-2}$) | 0.07 | 0.60 | 0.60 | 0.71 | 0.71 | 0.75 | 1.16 | 2.64 |

Figure 3.10 (a), (b) shows the relaxed structures of the {001} surface, two distinct orderings corresponding to two different repeat units. The {001}-S surface

(figure 3.10(a)) corresponds to a splitting of the layers at the interlayer mid-point, leaving a typical terminated surface of S atoms, as seen in the bulk structure, whereas the {001}-Fe surface (figure 3.10(b)) cuts the bulk structure mid-layer leaving a partially vacant layer of Fe atoms at the surface. This is a type-III surface, reconstructed to a type-II.

The {001}-S surface is by far the most important surface in mackinawite. The very low surface energy associated with this surface is due to the breaking of only the weak interlayer Van der Waal's S-S bonding between the S atoms, which results in only negligible relaxation of the surface species. The {001}-Fe termination divides the Fe-Fe basal plane into a reconstructed type-III surface, and as such breaks the greatest number of Fe-S bonds, leading to a high surface energy of 6.41 $Jm^{-2}$ prior to relaxation. Upon relaxation the surface atoms experience large displacements, with the Fe-S bond length decreasing from 2.24 Å to 1.89 Å and the Fe-S-Fe bond angle increasing from 110.0º to 152.8º.

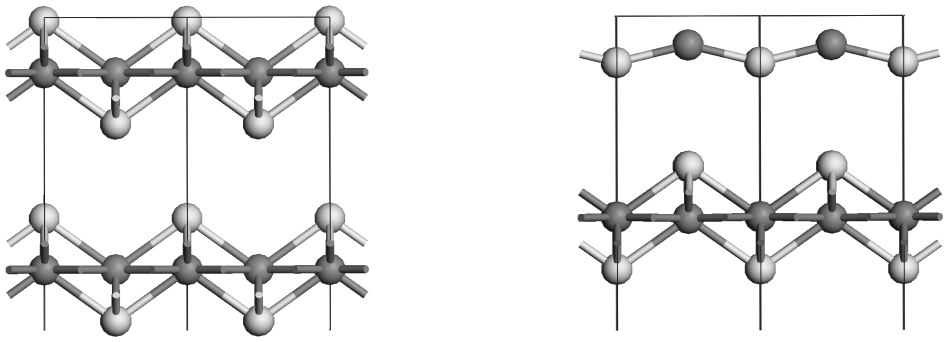

(a) (b)

Figure 3.10 (a), (b) – Schematic of the (a) relaxed {001}-S and (b) {001}-Fe surfaces. Both diagrams show a bulk layer beneath the surface and are viewed along the *a* axis.

The next most stable surfaces are the identical {011} and {101} planes, which possess only a single repeat unit (figures 3.11(a), (b)) which terminates in a Fe atom at the surface. These surfaces possess a surface energy of 1.14 $Jm^{-2}$ prior to relaxation and 0.60 $Jm^{-2}$ afterwards, a decrease of 47%. This is accompanied by a displacement of the surface Fe atom of 0.27 Å into the surface.

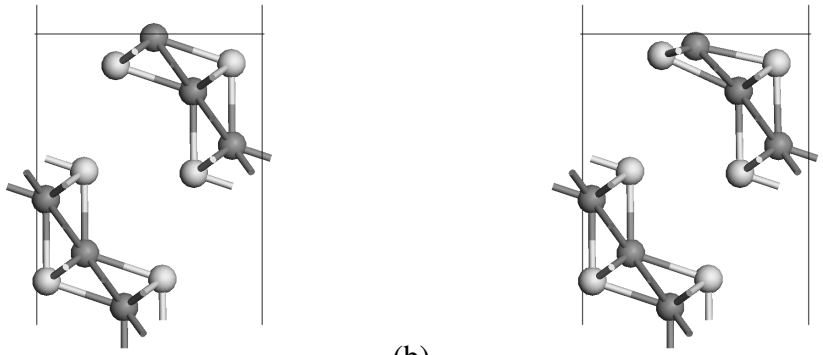

(a) (b)

Figure 3.11 (a), (b) – The (a) unrelaxed and (b) relaxed surface structure of the {011} surface, viewed along the *b* axis.

The {100} (and {010}) surface possesses only one repeat unit (figures 3.12 (a) and 3.12 (b)), which demonstrates a large reduction in the surface energy upon relaxation, of the order of 40%, with a displacement of the surface sulfur atom out of the plane of the surface by 0.09 Å (figure 3.12(a), (b) and 3.13(a), (b)).

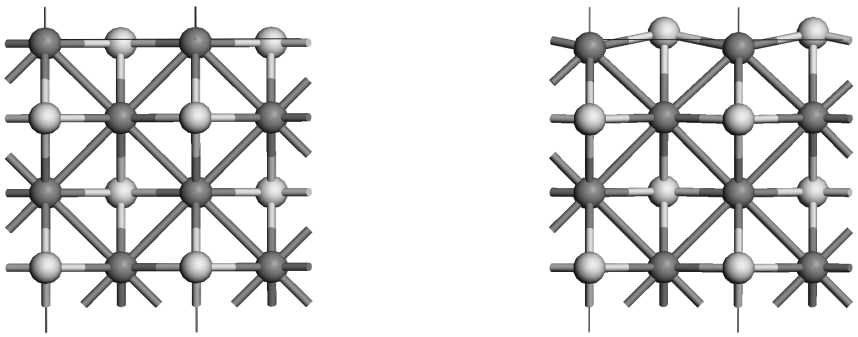

(a) (b)

Figure 3.12 (a), (b) – The (a) unrelaxed and (b) relaxed surface structure of the {100} surface, viewed along the *a* axis.

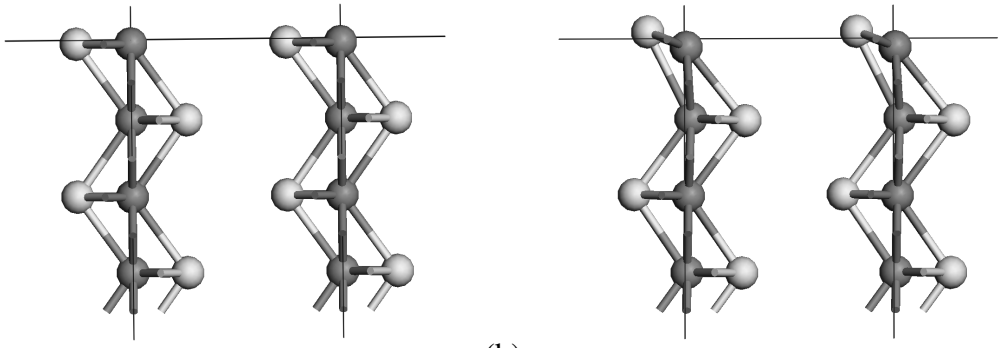

(a) (b)

Figure 3.13 (a), (b) – The (a) unrelaxed and (b) relaxed surface structure of the {100} surface, viewed along the *b* axis.

In the case of the {111} surfaces, two repeat units are possible. However the first is a type-II (Figure 3.14(a), (b)) and the second a type-III, which reverts to the type-II surface upon reconstruction. A very large relaxation is seen for the {110} surface, where a decrease in surface energy of 70% occurs upon energy minimisation, whereas the {111} surface demonstrates an even larger decrease of 78%. These large reductions in surface energy upon relaxation demonstrate the relatively high instability of these surfaces and the requirement for a significant relocation of both S and Fe atoms at the surface. The {110} surface in particular demonstrates a notable reconstruction of the mackinawite structure upon relaxation (figures 3.15(a), (b) and 3.16(a), (b)), as does the {111} surface (figure 3.14(a), (b)).

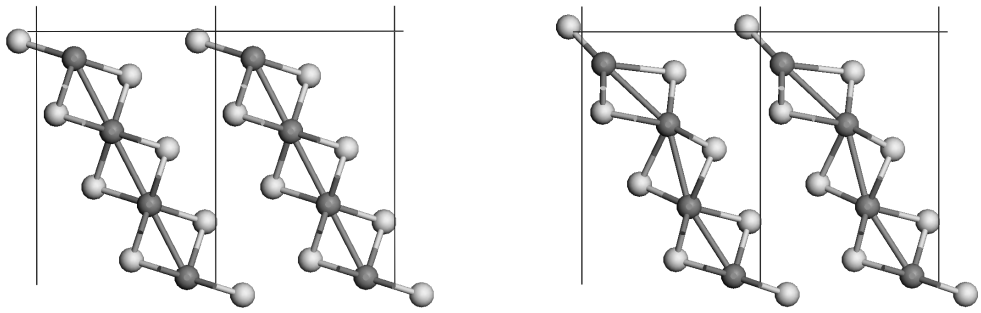

(a) (b)

Figure 3.14 (a), (b) – The (a) unrelaxed and (b) relaxed {111} structure viewed along the *b* axis.

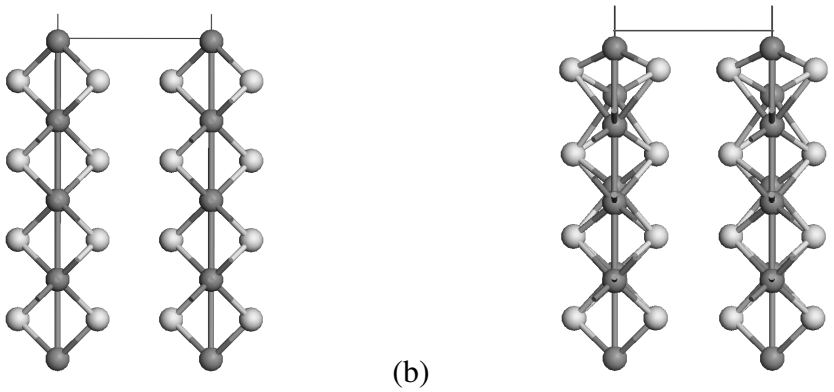

(a) (b)

Figure 3.15 (a), (b) – The (a) unrelaxed {110} structure viewed along the *a* axis and (b) relaxed {110} viewed in the same direction.

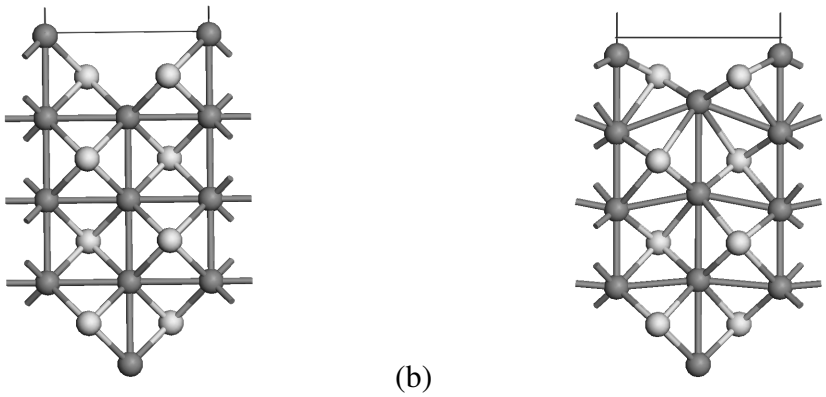

(a) (b)

Figure 3.16 (a), (b) – The (a) unrelaxed {110} surface structure viewed along the *b* axis and (b) relaxed {110} surface structure viewed along the *b* axis.

Examining the electron diffraction experiments of Lennie *et al.* (1995), single crystals of approximately stoichiometric mackinawite were found to produce patterns consistent with mackinawite lying with its {001} plane parallel to the carbon film substrate on which it was deposited. This to some extent confirms our finding that the {001} surface is the most chemically important surface in terms of stability and hence in the crystal morphology of mackinawite. The selected area electron diffraction (SAED) patterns obtained by Ohfuji & Rickard (2006) of both freeze-dried and precipitated mackinawite show clearly the {001} to be the most stable surface, followed in decreasing stability by the {101}, {200} (equivalent to the {100} surface) and {111} planes. These findings are in excellent agreement with the hierarchy of surface energies predicted by our derived potential model. The failure to observe experimentally the {110} surface reflections is explained by its relatively high surface energy, causing this surface not to be expressed in the calculated crystal morphology, as shown in figure 3.17. The faint occurrence of the {111} surface reflection can be explained via its relatively higher surface energy compared to the {100} and {101} surface and its relatively small contribution to the crystal morphology.

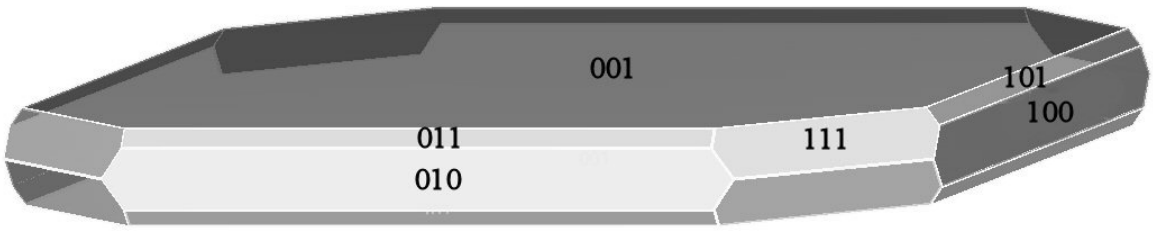


Figure 3.17 – The calculated crystal morphology of mackinawite, from the derived FeS potential. The crystals grow in tabular forms, with the {001} surface highly prominent.

Ohfuji & Rickard (2006) describe the mackinawite crystals grown as being thin and tabular in form, in excellent agreement with the calculated morphology.

### 3.3.3 Summary

This section has taken the values predicted from the previous DFT calculations of the phonon modes and elastic constants of a single mackinawite layer and, together with the experimental structural parameters, fitted them to interatomic potential parameters which reproduce these values accurately. This IP is then used to find the unrelaxed and relaxed surface energies and structures of lower-order surfaces of mackinawite, and from these the crystal morphology is calculated. The predicted morphology is in excellent agreement with that observed experimentally.

## 3.4 Impurities in Mackinawite

### 3.4.1 Introduction

As mentioned in section 3.1.2, naturally occurring mackinawite, such as that located in lake sediments, is often found with transition metal atoms incorporated into the structure. Studies have found that these impurities include Ni (up to 20%), Co (up to 20%), Cu (up to 10%) and Cr (up to 10%) (Clark, 1969; Vaughan, 1969). More recently, a number of studies have found that mackinawite is able to capture heavy metal atoms on both the (001) surface and inside the octahedral interstitial sites (Moyes *et al.*, 2002, Liu *et al.*, 2008, Mullett *et al.*, 2004). It is also plausible that any surplus Fe in the structure would occupy these sites, and this may explain why the

composition of naturally occurring mackinawite is Fe-rich or S-deficient with the formula $Fe_{1-x}S$ (where $0 < x < 0.07$) (Vaughan & Ridout, 1971). Previous work found that the hardness of mackinawite increases with increasing impurity content (Vaughan, 1969; Clark, 1970a) even for small amounts of impurities, an effect ascribed to the substitution of transition metal impurities into the Fe spaces (Clark, 1969). Studies have also indicated that increasing Co concentration (up to 20-25%) in the mackinawite structure leads to a decrease in both the *a* and *c* lattice parameters, opposite to that found for Ni where the lattice parameters increased with the impurity concentration. As to the location of the impurity atoms in the mackinawite structure, Vaughan (1970) noted that the layered structure of mackinawite allows the incorporation of additional interstitial layers between the Fe-S, which has opened up the possibility of introducing novel new layers into these locations (Peng *et al.*, 2009).

In order to ascertain the effects of the presence of these interstitial impurities on the mackinawite structure, GGA calculations were undertaken with impurity atoms introduced into the interstitial octahedral positions. The bonding, or lack thereof, of the impurity atoms and the S atoms will be examined. Based on the calculations of the pure mackinawite structure, non-magnetic GGA calculations with no applied $U_{eff}$ value are used in all simulations. As it was also determined that, for a range of Ni-S materials, a $U_{eff}$ value is not required in order to achieve a good description of the material properties (Wang *et al.*, 2007), no $U_{eff}$ value is applied to the Ni atom in these simulations. The same can be argued for Cu impurities, since work (Sadtler *et al.*, 2009) using the VASP code and pure GGA has provided an excellent description of the $CuS_2$ (chalcocite) phase, and similarly the sulfide compounds of both Co and Cr modelled by Hobbs and Hafner (1999).

### 3.4.2 Interstitial Nickel

A doping level of 20% interstitial nickel is equivalent to one nickel atom per unit cell, giving a compound with the formula $Ni_{0.5}FeS$. To simulate this scenario a single Ni atom is placed at the centre of the unit cell, located at the interstitial octahedral site in the mackinawite structure (Figure 3.18).

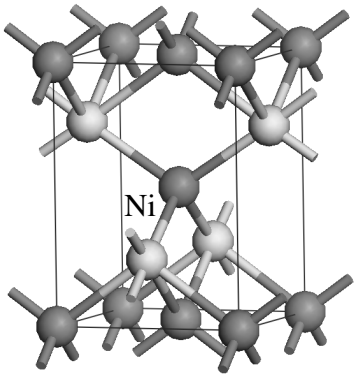


Figure 3.18 – Ni atom placed at the centre of the mackinawite unit cell. Fe atoms are shown in dark gray, S atoms in light gray.

The *c* lattice parameter is fixed at the experimental value of 5.033 Å, in the same manner as the simulations of the pure mackinawite unit cell in section 3.2.4, and both the *a* and *b* parameters are varied from 3.40 Å to 4.0 Å in order to determine the minimum internal energy for this atomic configuration. The cell volume and size are fixed in each calculation, and only the internal ionic coordinates are permitted to relax. An energy cut-off of 400 eV is used in this instance, with a dense Monkhorst-Pack k-point mesh of 11x11x11, a Gaussian smearing parameter of 0.02 eV and an electronic self-consistent loop break condition of $10^{-5}$. Figure 3.19 presents the results of these calculations.

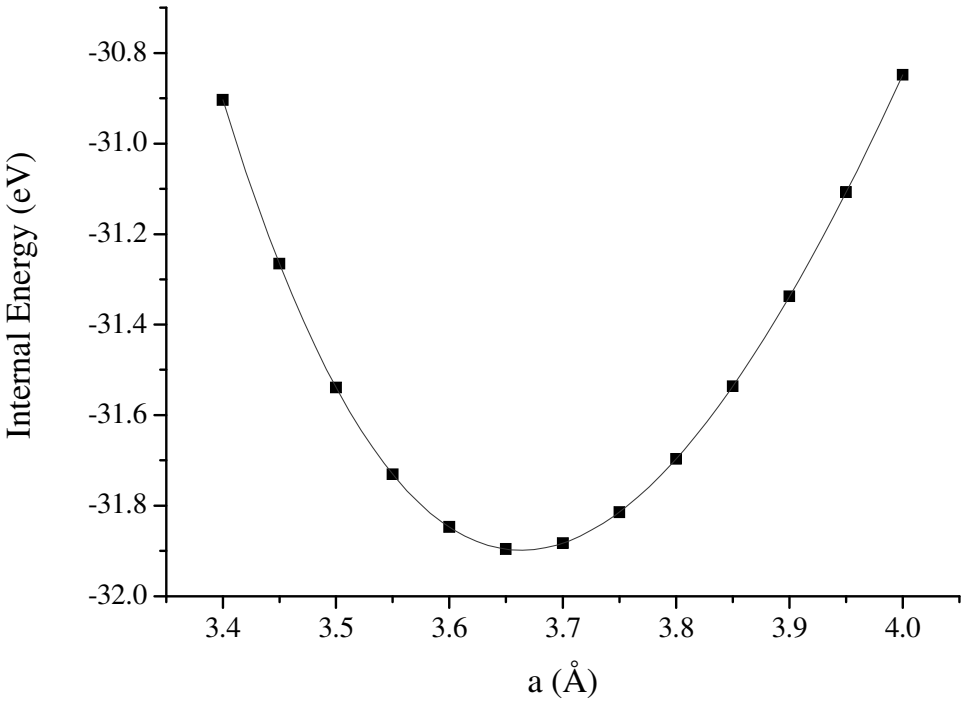


Figure 3.19 – Plot of the internal energy of the $Ni_{0.5}FeS$ structure versus *a* (and *b*) lattice parameter for ionic coordinate relaxation only. The *c* parameter is fixed at 5.033 Å. The line of best fit is a $5^{th}$ order polynomial.

The energy minimum of figure 3.19 occurs at an *a* parameter of 3.664 Å, which is very close to the quoted experimental *a* parameter for the undoped mackinawite structure, 3.6735 (± 0.0001) Å, and is closer to this experimental value than that calculated for the undoped mackinawite *a* parameter (3.612 Å) in section 3.2.4. It is noted that the variation in the internal energy is not symmetrical about its minimum, and at values of *a* lower than the minimum in energy the gradient of the curve is greater than at higher values, indicating that the presence of the Ni atom makes compression of the structure in the plane of the layers more difficult than expansion in the same plane.

The effect of the Ni interstitial atom on the stability of the *c* parameter of the

mackinawite structure is also important. In order to test the GGA description of this relation, the *a* and *b* parameters were fixed to the calculated value of 3.664 Å and the *c* parameter varied in order to determine the most energetically favourable value for *c*. The same simulation parameters are used as in the previous case. The results of these calculations are presented in figure 3.20.

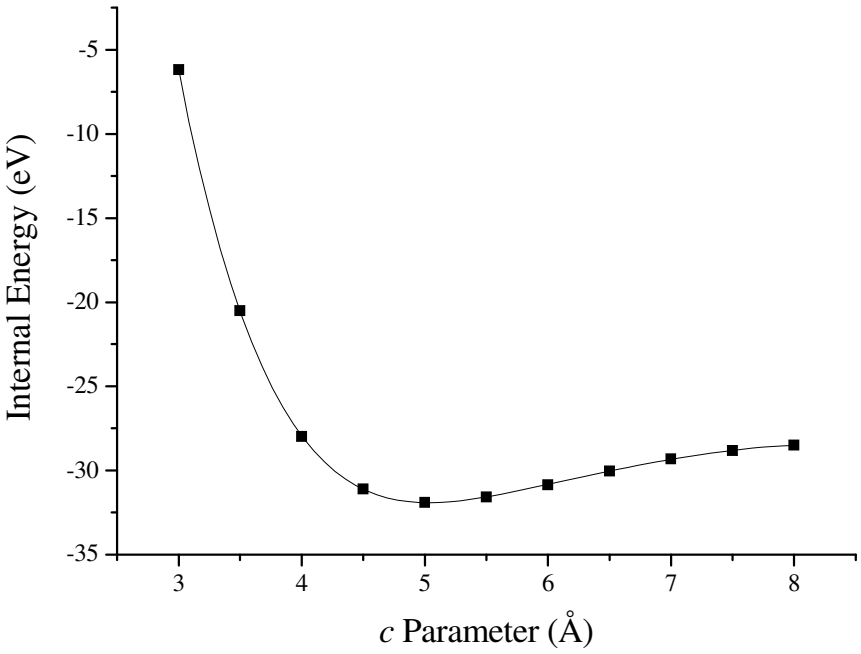


Figure 3.20 – Variation of internal energy with *c* parameter for Ni doped mackinawite.

Figure 3.20 shows a clear energy minimum for the *c* parameter, located at 5.034 Å, in contrast with the situation found for the undoped mackinawite case, where no clear minimum in the energy was found (figure 3.2). The predicted *c* parameter at minimum internal energy is close to that of the experimental undoped mackinawite structure, $c = 5.0328 (\pm 0.0001)$ Å.

These results, showing clear energy minima with respect to all three lattice directions, indicate that a full relaxation of the unit cell and internal coordinates of this structure is possible without errors arising from the GGA method being unable to

account for the interlayer dispersive forces. Full cell relaxations at a range of basis set cut-off energies were undertaken for both spin-polarised and non-spin-polarised situations, followed by relaxations of only the internal ionic coordinates and a final singlepoint electronic relaxation to obtain the ground state energy. The results of these calculations, and their convergence with basis set cutoff energy, are presented in Table 3.14.

Table 3.14 – Lattice parameters and internal energies for both non-spin-polarised and spin-polarised Ni doped mackinawite structure relaxation calculations.

| **Cutoff (eV)** | **Non-spin polarised** | | | **Spin-polarised** | | |
|---|---|---|---|---|---|---|
| | **a (Å)** | **c (Å)** | **Internal Energy (eV)** | **a (Å)** | **c (Å)** | **Internal Energy (eV)** |
| 400 | 3.657 | 5.042 | -31.899 | 3.658 | 5.041 | -31.899 |
| 500 | 3.661 | 5.047 | -31.909 | 3.659 | 5.047 | -31.909 |
| 600 | 3.661 | 5.047 | -31.909 | 3.659 | 5.047 | -31.909 |
| 700 | 3.661 | 5.047 | -31.909 | 3.661 | 5.047 | -31.909 |
| 800 | 3.661 | 5.047 | -31.909 | 3.661 | 5.047 | -31.909 |

Convergence occurs at an energy cutoff of 500eV for the non-spin polarised case. No final magnetic moment on either the Fe or Ni atoms is found to be supported in the spin-polarised calculations for any basis set cut-off energy. The full relaxation of both the unit cell dimensions and the internal coordinates yields a unit cell with lattice parameters $a = b = 3.661$ Å and $c = 5.047$ Å, and the first S coordinate is found to be 0.2369.

The final singlepoint calculation has used the tetrahedral method with Blöchl corrections in order to produce the electronic DOS for this structure (Figure 3.21). A sampling space of 3000 energy data points was used.

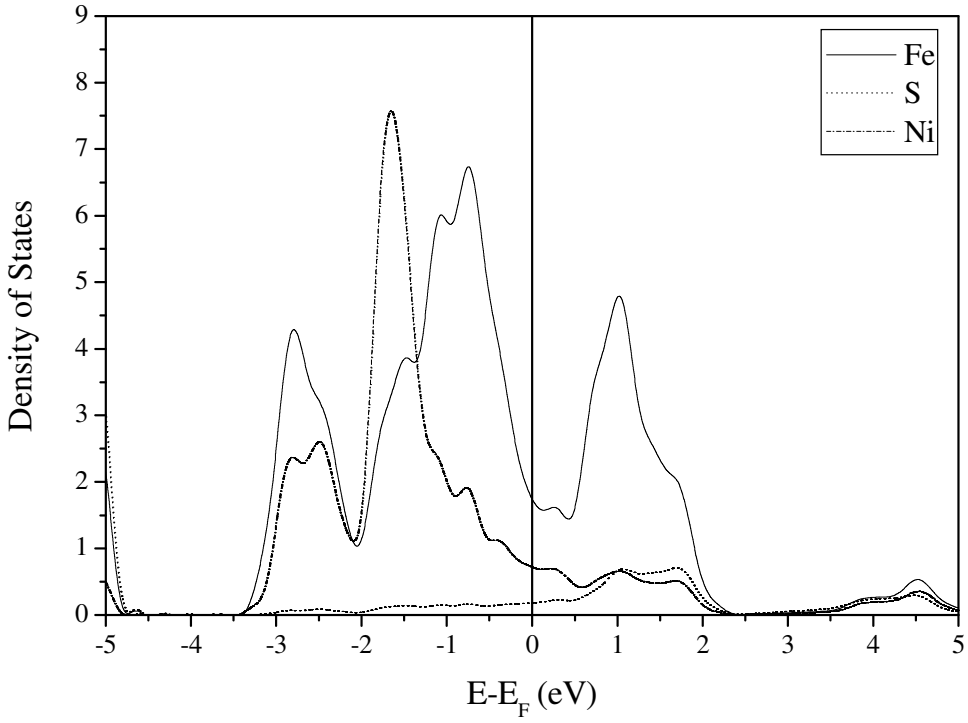


Figure 3.21 – Electronic DOS graph for mackinawite structure with 20% interlayer Ni atoms. The Fe contribution is shown with a solid black line, the S contribution a dotted line and the Ni contribution a dashed line.

The DOS for the Ni-doped mackinawite structure demonstrates that both the Ni atom and the Fe atoms provide accessible bands at the Fermi level, indicating that the electrons are delocalised, and that the Ni atom contributes considerably to this delocalisation.

The comparison of the Bader populations of $Ni_{0.5}FeS$ and pure mackinawite (table 3.15) shows that the introduction of the Ni atom has the effect of breaking the charge symmetry of the two Fe atoms to a small degree, such that the Fe atom at (0, 0, 0) has 0.07 electrons less than the Fe at (0, 0.5, 0.5).

Table 3.15 – Calculated Bader populations of $Ni_{0.5}FeS$ structure. FeS Bader charges for FeS are shown for comparison (from section 3.2.4).

| Atom | $Ni_{0.5}FeS$ Bader Charge (e) | FeS Bader Charge (e) |
|---|---|---|
| $Fe^1$ | +0.82 | +0.85 |
| $Fe^2$ | +0.75 | +0.85 |
| $S^1$ | -1.02 | -0.85 |
| $S^2$ | -1.02 | -0.85 |
| Ni | +0.47 | - |

The Ni atom has a Bader charge of +0.47, an appreciable level of oxidation and comparable to that found by Wang *et al.* (2007) when they modelled a range of Ni-S materials. By analogy with the predominantly covalent materials, it can be deduced that there is a high level of covalent nature predicted for the Ni-S bonds in $Ni_{0.5}FeS$. The Bader analysis also shows that both the Fe atoms, to different degrees, have an increased Bader population in the doped Ni structure relative to pure mackinawite, suggesting that the presence of the Ni atom in the octahedral site affects both Fe. The calculated $Ni_{0.5}FeS$ structure predicts a Ni-Fe distance of 2.524 Å; this is actually slightly lower than the Fe-Fe distance of 2.589 Å The distance between Ni-Ni atoms in the plane of the layers is found to be 3.661 Å, indicating that direct conduction between these species is unlikely for this level of doping, and the delocalisation of the Ni valence electrons is unlikely to be caused by direct Ni-Ni interaction.

With the method to reliably find the ground state of 20% doped FeS determined, the other impurity atoms that have been found in natural mackinawite are tested to investigate the effect each has on the properties of mackinawite.

### 3.4.3 Interstitial Cobalt

Replacing the interstitial Ni atom with a Co atom, the relaxation on both unit cell and internal coordinates at a variety of basis-set cut-off energies and both spin-polarised and non-spin-polarised cases are repeated. The results of these calculations at a range of basis set cutoff energies are presented in table 3.16.

Table 3.16 – Calculated lattice parameters and internal energies for both non-spin-polarised and spin-polarised Co doped mackinawite structure relaxation calculations.

| ENCUT (eV) | Non-spin polarised | | | Spin-polarised | | |
|---|---|---|---|---|---|---|
| | a (Å) | c (Å) | Internal Energy (eV) | a (Å) | c (Å) | Internal Energy (eV) |
| 400 | 3.623 | 5.004 | -33.226 | 3.623 | 5.005 | -33.226 |
| 500 | 3.626 | 5.009 | -33.238 | 3.626 | 5.009 | -33.238 |
| 600 | 3.626 | 5.009 | -33.239 | 3.626 | 5.009 | -33.239 |
| 700 | 3.626 | 5.009 | -33.239 | 3.626 | 5.009 | -33.239 |

The relaxed lattice parameters are determined to be a = 3.626 Å and c = 5.009 Å, with no observable difference between non-spin-polarised and spin-polarised calculations suggesting that the system cannot support a net magnetisation. Convergence occurs at a basis set cutoff energy of 500eV.

The calculated electronic DOS (figure 3.22) is similar in form to that found in the case of Ni; however the Co atom is noted to provide a slightly larger number of available states at the Fermi level compared to the Ni-doped case.

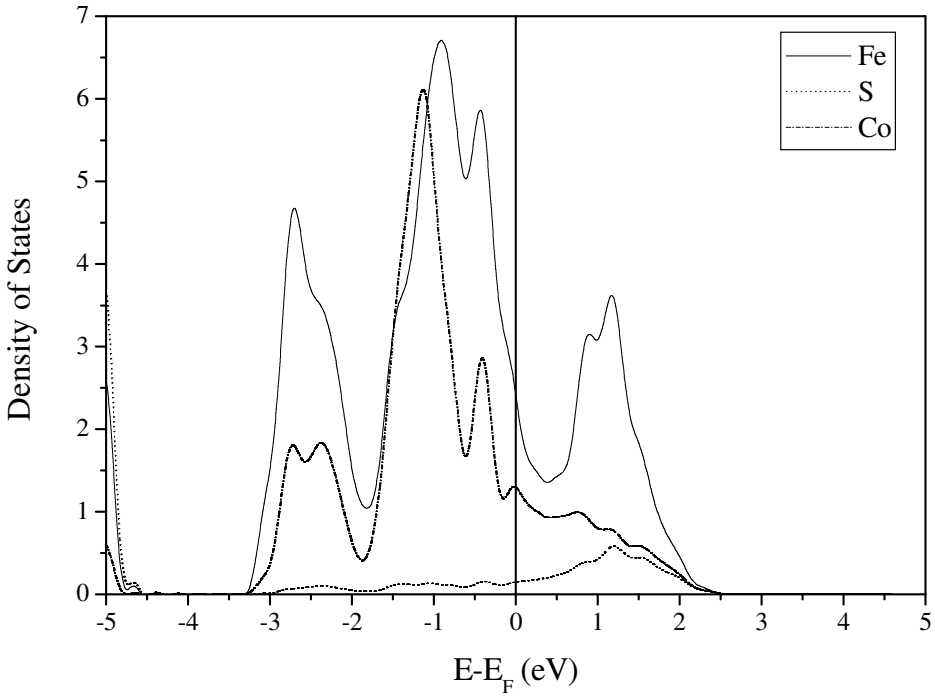


Figure 3.22 - Calculated electronic DOS for $Co_{0.5}FeS$.

Bader analysis of the electronic ground state for $Co_{0.5}FeS$ is given in table 3.17.

Table 3.17 – Calculated Bader populations of $Co_{0.5}FeS$ structure.

| Atom | $Co_{0.5}FeS$ Bader Charge (e) | FeS Bader Charge (e) |
|---|---|---|
| $Fe^1$ | +0.80 | +0.85 |
| $Fe^2$ | +0.71 | +0.85 |
| $S^1$ | -1.04 | -0.85 |
| $S^2$ | -1.05 | -0.85 |
| Co | +0.58 | - |

A greater fraction of electrons are donated from the Co atom to the S atoms compared to the Ni case, suggesting that the bond is likely to be stronger. This is also indicated by the slightly reduced *c* parameter, which suggests that the Co atom has more of a binding effect with the layers than the Ni atoms, and by the calculated Co-Fe bond length of 2.505 Å, slightly shorter than that found for $Ni_{0.5}FeS$. The

calculated charge difference between the two Fe atoms for $Co_{0.5}FeS$ is almost 0.1 electrons, a significant difference. According to the Bader calculations, the Co atom has donated 0.58 electrons to the Fe-S system.

### 3.4.4 Interstitial Copper

Cu is introduced into the structure in the same manner as Ni and Co. Convergence with basis set cutoff energy is found to occur at 500eV, where the relaxed structure is found to possess the lattice parameters $a = b = 3.689$ Å and $c = 5.266$ Å. Bader charge analysis of the electronic ground for this structure state is presented in table 3.18.

Table 3.18 – Calculated Bader populations of $Cu_{0.5}FeS$ structure.

| Atom | $Cu_{0.5}FeS$ Bader Charge (e) | FeS Bader Charge (e) |
|---|---|---|
| $Fe^1$ | +0.80 | +0.85 |
| $Fe^2$ | +0.73 | +0.85 |
| $S^1$ | -1.03 | -0.85 |
| $S^2$ | -1.03 | -0.85 |
| Cu | +0.53 | - |

The Bader charge analysis of $Cu_{0.5}FeS$ indicates that, in a similar manner to that seen for Ni and Co, the Cu atom contributes significant electron density to the Fe-S system. The calculated electronic DOS for the $Cu_{0.5}FeS$ structure is given in figure 3.23.

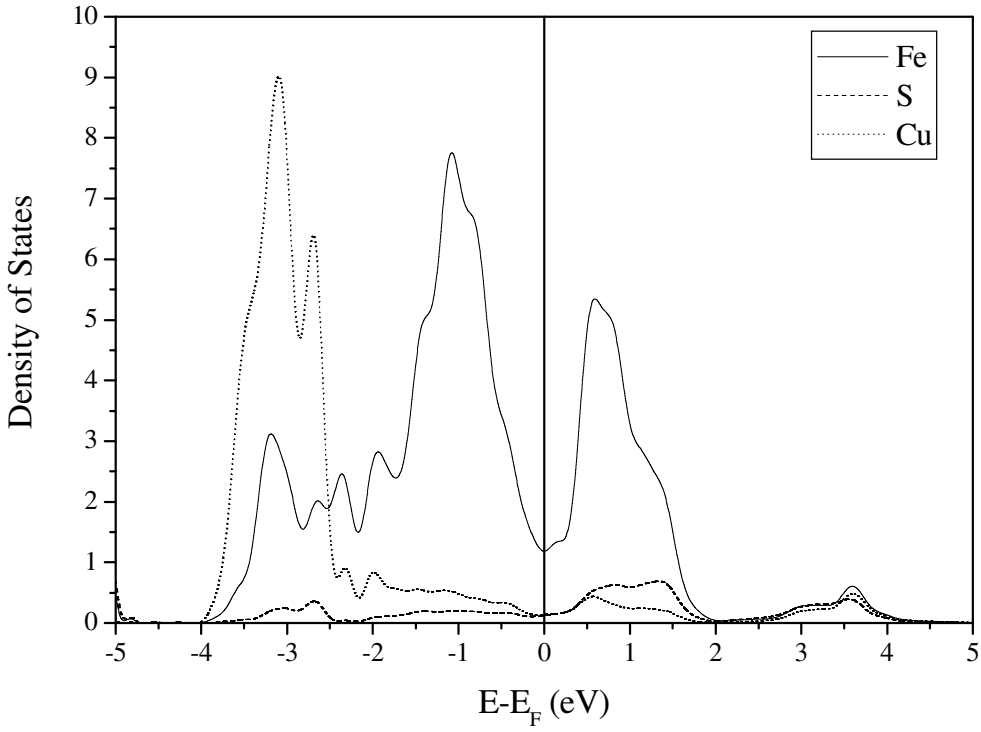


Figure 3.23 – Calculated electronic DOS for $Cu_{0.5}FeS$.

The Fermi energy cuts the conduction band of the Fe atoms, with little contribution from the Cu or S atoms. This is in marked contrast to the Ni and Co doped cases, where the interstitial transition metal ions contributed a number of states at the Fermi level. It is noted in this respect that the Cu-Fe distance is 2.633, which is around 0.1 Å longer than either the Ni-Fe or Co-Fe distances.

### 3.4.5 Interstitial Chromium

Finally, full cell relaxations are repeated for a Cr dopant atom in the interstitial octahedral site. Convergence occurs at a basis set cutoff of 600eV, which produces a tetrahedral structure with the lattice parameters $a = b = 3.595$ Å and $c = 5.241$ Å. A Bader analysis of the electronic groundstate of this structure is given in table 3.19.

Table 3.19 – Bader charge analysis for $Cr_{0.5}FeS$.

| Atom | $Cr_{0.5}FeS$ Bader Charge (e) | FeS Bader Charge (e) |
|---|---|---|
| $Fe^1$ | +0.75 | +0.85 |
| $Fe^2$ | +0.63 | +0.85 |
| $S^1$ | -1.33 | -0.85 |
| $S^2$ | -1.33 | -0.85 |
| Cr | +1.28 | - |

The Bader charge analysis for this structure shows that the Cr atoms are oxidised to a greater extent than those calculated for the other impurities; 1.28 electrons have been removed from the Cr atom, which suggests that the Cr ion in mackinawite exists in an oxidation state greater than +2, the posited oxidation state for the other impurities tested.

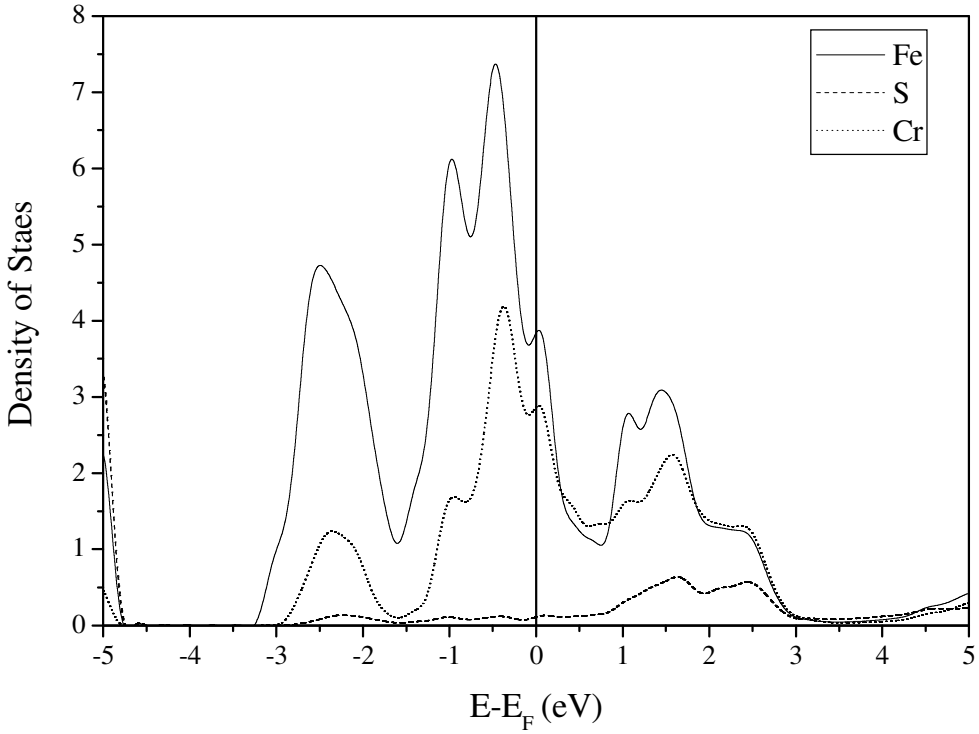


Figure 3.24 – Calculated electronic DOS for $Cr_{0.5}FeS$.

The calculated electronic DOS for $Cr_{0.5}FeS$ is depicted in figure 3.24. The Cr

atoms contribute roughly as many states at the Fermi level as the Fe atoms, with a Cr-Fe bond distance of 2.621 Å.

### 3.4.6 Summary

The results for the 20% Ni-, Co-, Cr- and Cu-doped FeS calculations are summarised in table 3.20.

Table 3.20 – Calculated lattice parameters, oxidation states for each atom and M-Fe bond lengths for the doped mackinawite structure, where M = Ni, Co, Cr and Cu. The charge is calculated from the Bader population on each atom.

| | Lattice Parameters | | Net Bader Charge (e) | | | | |
|---|---|---|---|---|---|---|---|
| | **a (Å)** | **c (Å)** | **$Fe^1$** | **$Fe^2$** | **S** | **M** | **M-Fe Bond Length (Å)** |
| **Ni** | 3.661 | 5.048 | +0.815 | +0.742 | -1.014 | +0.474 | 2.524 |
| **Co** | 3.626 | 5.009 | +0.801 | +0.712 | -1.045 | +0.577 | 2.505 |
| **Cu** | 3.689 | 5.266 | +0.805 | +0.729 | -1.032 | +0.531 | 2.633 |
| **Cr** | 3.595 | 5.241 | +0.752 | +0.628 | -1.330 | +1.280 | 2.621 |

These results show that the inclusion of impurity atoms into the mackinawite structure is likely to have only a small effect on the lattice parameters, compared to the undoped mackinawite case. An increase in the *c* parameter for the Cu- and Cr-doped structures of around 0.2 Å is the most significant effect measurable using crystallographic methods. This is further shown by the longer M-Fe bond lengths for these dopants.

From the calculated Bader charges, the approximate oxidation states of the atoms can be estimated. The Fe atoms within the layers show only small variations from the pure mackinawite case, indicating that these remain in the 2+ state regardless of the dopant atom species. The Ni, Co and Cu atoms bader charges are

approximately half of that calculated for Fe, suggesting that these atoms are in the 1+ formal oxidation state. Finally, the Cr atom has a bader charge of around three times that of the Ni, Co and Cu, suggesting that $Cr^{3+}$ is present.

The finding that there is a direct interaction between the interstitial doping atom and the neighbouring S atoms in the plane of the layer leads to the conclusion that, when such impurities are present the interstitial impurities acting to stabilise the mackinawite structure, by replacing the weak dispersive forces between layers with chemically bonded interactions between the S and the doping atoms. This is likely to have a significant impact upon the surface energies of the doped mackinawite structure compared to the undoped, and the crystal habit of doped mackinawite will deviate from that of figure 3.17. Similarly, the transition of mackinawite to other Fe-S structures will likely be affected by the presence of impurities, particularly the transition to the greigite structure which chiefly involves movement of the Fe sub-lattice.

The DOS for each of these indicates that doping with Cr will lead to the greatest number of available states at the Fermi level. The Cr atom is also oxidised to a greater extent that that other impurities tested, evidenced by the oxidation state of +1.28. The bulk of these electrons have transferred to the S atoms, which are appreciably more reduced by Cr than for the other impurities tested.

It is noted that the calculated M-Fe bond lengths are close to the Fe-Fe bond length (2.65 Å) in the layers which leads to the metallic behaviour of mackinawite.

## 3.5 Conclusions

DFT-GGA calculations used to simulate the mackinawite structure have shown that the energetically most favourable stable arrangement is the metallic non-magnetic case. The DOS calculations show that at all values for the $U_{eff}$ parameter in the GGA+U formalism the Fermi level of mackinawite cuts the Fe *d*-orbital band, indicating the presence of mobile charge carriers in the plane of the mackinawite layers. In comparison with iron oxides, GGA predictions regarding mackinawite are most precise without an applied $U_{eff}$ parameter, a fact ascribed to the delocalisation of the Fe 3*d* electrons in the individual mackinawite layers. In more highly correlated materials the *d* electrons usually need to be localised by the $U_{eff}$ parameter, but in mackinawite values other than $U_{eff}$ = 0 eV give incorrect predictions of the magnetic nature. Rohrbach *et al.* (2003) indicates three aspects of the GGA modelling of transition metal sulfides that are predicted incorrectly; semiconducting gap, too low magnetic moment and too small an equilibrium volume. All these properties are improved by the inclusion of the Hubbard $U_{eff}$ parameter. Mackinawite, however, is a non-magnetic metallic compound, where inclusion of the changes associated with $U_{eff}$ values would be incorrect.

The physical parameters predicted using a single layer structure were utilised for the fitting of an interatomic potential, which predicts the elastic constants of the normal mackinawite structure to be $c_{11}$ = 145.6 GPa, $c_{12}$ = 99.1 GPa, $c_{13}$ = 8.5 GPa and $c_{31}$ =13.0 GPa. Calculations of both relaxed and unrelaxed surface energies have highlighted the stability of the {001} surface with S atom termination compared to all other surfaces, indicating that this surface is the most important in the crystal morphology. The calculated surface energies and resulting morphology are in excellent agreement with experimental findings regarding the most stable surfaces of

synthetic crystals of mackinawite. Finally, the derived interatomic potential model is an excellent basis for future work on crystal growth and adsorption processes at the surfaces of mackinawite.

Calculations show that the presence of transition metal impurity atoms in the octahedral interstitial site has the effect of stabilising the mackinawite structure, and the ionic bonding due to the M-S interaction dominates the interlayer attraction, over and above that of the Van der Waal's forces between S atoms, where M = Ni, Co, Cu or Cr. This would seem to indicate that the presence of interstitial transition metal atoms is a notable factor in the stabilisation of the mackinawite structure.

# 4. Greigite

## 4.1 Introduction

The iron sulfide mineral greigite ($Fe_3S_4$) was first defined as a mineral by Skinner *et al*. (1964) from a Californian lacustrine sediment sequence and has since been found in many natural environments with ages of up to several million years (Dekkers *et al.*, 2000). Due to its ubiquity in sedimentary rocks, greigite is now considered to be a common magnetic material (Roberts, 2005).

This phase has been implicated as an important catalyst in the development of proto-metabolism due to its similarity with the cubane cluster structure $Fe_4S_4$ (Russell and Hall, 1997), which is widespread in the active sites of a variety of enzymes (Nair 2008). In addition, greigite has been found in magnetotactic bacteria (Pósfai *et al.*, 1998a), where the magnetic nature of the mineral causes the bacteria to orientate along geomagnetic field lines. It is believed that a similar property explains its presence in the scales of a deep sea gastropod (Suzuki *et al.*, 2006). Due to its ferrimagnetic behaviour, it is an important material in paleomagnetism (Letard *et al.*, 2005), where it holds a record of the Earth's magnetic field. Biogenic $Fe_3S_4$ has also been found in soil samples (Stanjek *et al.*, 1994).

### 4.1.1 Structure

Greigite is the sulfide analogue of the iron oxide mineral magnetite ($Fe_3O_4$), and possesses the same cubic crystalline spinel structure (Letard *et al.*, 2005) with space group *Fd3m* (227). As such, the unit cell of greigite contains 56 atoms of which 24 are Fe and 32 are S. The Fe atoms are divided into two sub-lattices, with 8 Fe occupying tetrahedrally coordinated sites (hereafter referred to as A sites) and 16 on octahedral sites (B sites). In turn, the sulfur anions are bonded in a close-packed cubic lattice (Uda, 1965). The greigite unit cell structure is depicted in figure 4.1.

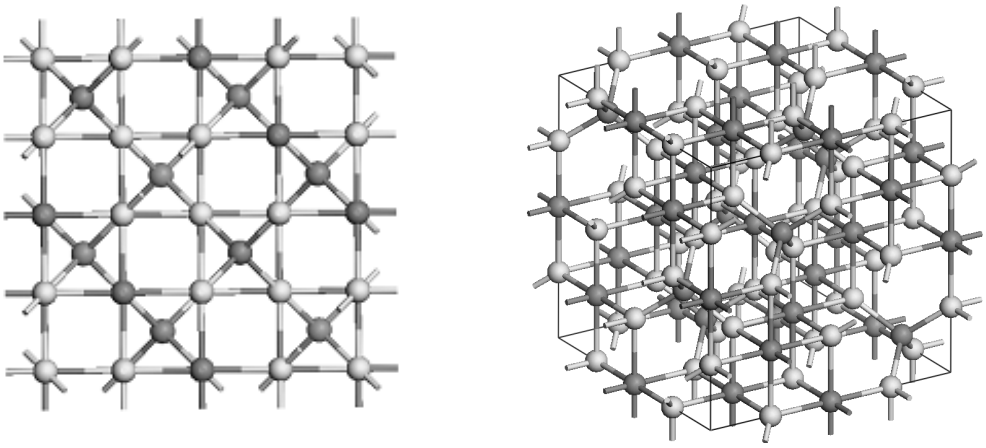

Figure 4.1 – Structure of Greigite, viewed along the c-axis (left) and off-axis (right)). The S atoms are shown in light gray and the Fe atoms dark gray.

It is not clear to what level impurities occur in natural greigite samples. It has been suggested that greigite possesses localised valence electrons, and that this limits the amount of transition metal impurities, such as Ni, Cu or Co in the greigite structure, since stable solid solutions could not be formed (Rickard & Luther, 2007).

### 4.1.2 Formation of Greigite

Prior to its discovery in nature, greigite was successfully synthesized in its pure form by Yamaguchi & Katsurai (1960) and later by Uda (1967), the latter as a precipitate of the reaction between Mohr's salt and sodium sulphate, and since then greigite has been successfully synthesised many times (*e.g.* Horiuchi *et al.*, 1970; Horiuchi *et al.*, 1974; Wada, 1977; Lennie *et al.,* 1995). Recently, both 1-dimensional rods (He *et al.*, 2006) and 2-dimensional nanosheets (Han & Guo, 2008) of greigite have been successfully synthesised. The micro-rods of greigite were selectively assembled using an *in situ* magnetic-field-assisted hydrothermal route using S precursors, of which cysteine was found to effectively produce exclusively $Fe_3S_4$. The presence of a magnetic field of 45 mT was found to contribute to the formation of $Fe_3S_4$ at higher temperature, and to have a large effect on the morphology of the crystals grown. In regard to the synthesised nanosheets, reaction temperature and precursor were again found to be the key factors in the phase of iron sulfide formed. It was found by Chang *et al.* (2008) that synthetic greigite, which is judged to be stoichiometric, grows in particles with equi-dimensional cubo-octahedral crystal habits, with elongation of the [111] or [100] crystallographic habits. This leads to the growth of plate-like or prism-like crystals.

In anhydrous condition, the greigite phase is believed to form only from mackinawite ($Fe^{2+}S^{2-}$) via oxidation of two-thirds of the $Fe^{2+}$ cations, together with re-arrangement about the close-cubic packed S anions (Lennie *et al.*, 1997) which in turn undergoes a small volume reduction of around 12% (Lennie *et al.*, 1995). In the absence of any other species, this solid state transformation is thought to proceed according to the equation:

$$4FeS_{mack} = Fe_3S_4 + Fe(0) \qquad \Delta G_r^\circ = +84.5 \text{ kJ mol}^{-1}$$

at 25°C (Rickard & Luther, 2007), making this thermodynamically unlikely. It is possible that $O_2$ present in the reaction chamber will catalyse this reaction (Lennie *et al.*, 1995).

In solvated environments the transition from $FeS_{mack}$ to $Fe_3S_4$ is thought to take the form (Rickard & Luther, 2007):

$$3FeS_{mack} + S^0 = Fe_3S_4 \qquad \Delta G_r^\circ = -13.7 \text{ kJ mol}^{-1}$$

at 25°C, and that this is much more probable in freshwater than marine environments, explaining the ubiquity of greigite in these milieus.

### 4.1.3 Experimental Studies: Electronic Structure

A number of studies of greigite are detailed in the literature, performed on both naturally occurring and synthetically fabricated $Fe_3S_4$ samples. The first Mössbauer spectroscopy study of synthetic greigite was conducted by Morice *et al.* (1969) who found that at room temperature, magnetic hyperfine structure is present and that the hyperfine fields found are consistent with the assignment of covalent ferrous ($Fe^{2+}$) iron. Vaughan and Ridout (1970) also synthesised greigite for Mössbauer measurements to investigate the spectra down to temperatures of 4.2K. The spectrum at 4.2K is interpreted to consist of three sets of magnetic hyperfine spectra, corresponding to iron in *three* different crystallographic positions in the spinel structure. The isomer shifts, quadrupole splitting and hyperfine fields of these three different types of iron suggests the presence of high-spin $Fe^{3+}$ in tetrahedral and octahedral sites, and high-spin $Fe^{2+}$ occupying only octahedral sites. This magnetic arrangement corresponds to that of an inverse spinel with the formula $(Fe^{3+})_A(Fe^{2+}Fe^{3+})_BS_4$. The tetrahedral and octahedral sub-lattices are aligned in an anti-parallel manner, rendering greigite ferrimagnetic.

The magnetisation, electrical conductivity and Mössbauer spectra of greigite were investigated by Spender *et al.* (1972), although the stoichiometry and quality of the samples used in this study are in some doubt, since both octahedral-site vacancies and water absorbed on particulate surfaces may have corrupted the $Fe_3S_4$. Magnetisation measurements were taken from 4.2K up to 300K, and the magnetic moment for three separate non-stoichiometric samples of greigite was measured to be 2.05, 2.04 and 1.58 $\mu_B$ / formula unit (f.u.), corrected to give an estimated value of $2.2 \pm 0.3$ $\mu_B$ / f.u. for pure stoichiometric greigite. The Mössbauer study on the purest samples at 4.2 K produces a complex spectrum, which is resolved to two magnetic sub-lattices. The moments on these sub-lattices are antiparallel, and the extrapolated zero field data indicates that the hyperfine field is almost the same for both tetrahedral and octahedral sites, counter to a previous finding (Morice *et al.*, 1969) that greigite contains both ferric and ferrous Fe on B sites. Electrical conductivity measurements found that the conductivity decreased by a factor of four from 300K to 4.2K, and that no sharp changes were found, suggesting that no Verwey-type transition is present, or can be evidenced from conductivity measurements. In order to explain the electronic structure of $Fe_3S_4$, two band schemes are suggested to explain the reduced magnetic moment:

(i) The first scheme is based upon the assertion that greigite has an average of ferric and ferrous Fe on B sites. Using the suggestion of Goodenough (1969) for the $Ni_3S_4$ and $Co_3S_4$, covalency effects in the sulfides can be accounted for by the $t_2$(A) and $e_g$(B) electrons becoming delocalised into a σ* band, which itself is unpolarised. For the case of greigite, the $t_{2g}$(B)↓ band overlaps σ*. The conduction mechanism would be due to electrons in the σ* band, different to that seen in magnetite where it is caused by the single $t_{2g}$(B)↓ electron (Coey *et al.*, 1971). This band scheme is

pictured in figure 4.2, and is similar to that found in magnetite (Sasaki, 1997). This scheme suggests that $Fe_3S_4$ is semi-metallic in nature, due to electron hopping between ferric and ferrous octahedral sites.

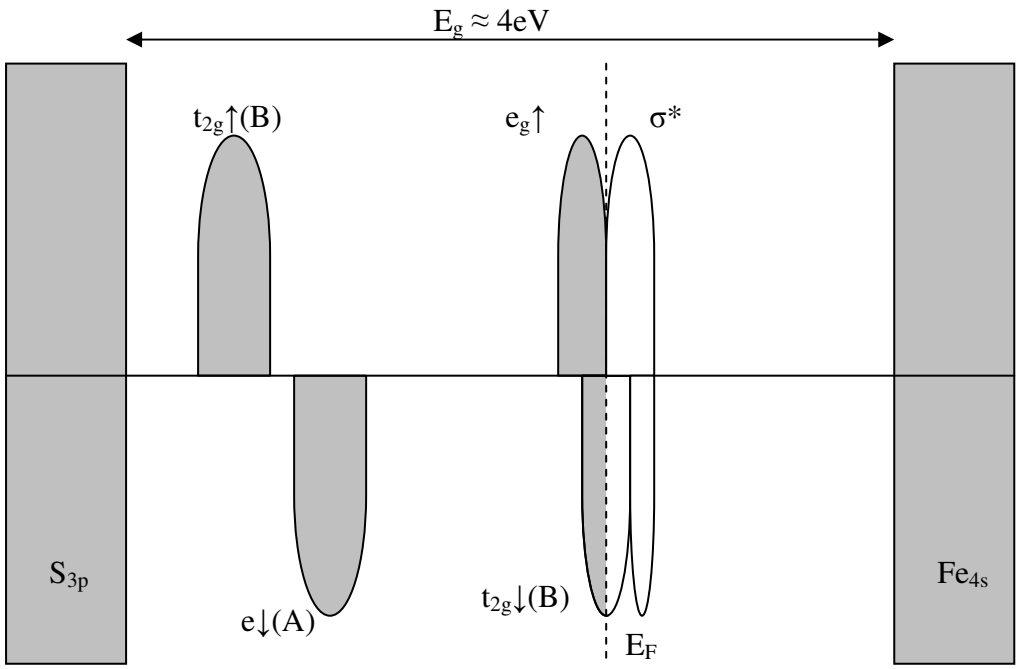


Figure 4.2 – Proposed one electron band scheme for greigite, band scheme (i). Adapted from Spender *et al.* (1972). The unoccupied $3d\uparrow(A)$ and $e_g\uparrow(B)$ are not shown.

(ii) The second band scheme derives from the assertion that greigite possesses only $Fe^{2+}$ iron on B sites, and is schematically depicted in figure 4.3. In this case the S present in one $Fe_3S_4$ unit must reduce one $Fe^{3+}$ ion per molecule ($Fe_3S_4$) to the $Fe^{2+}$ state, and this leads to one hole in the valence band per $Fe_3S_4$ formula unit. In this scenario the $Fe^{2+}$ levels are below the top of this band, and conduction in this model is attributed to the holes in the valence band. It is further hypothesised that when Fe is coordinated with S in a lattice environment, the iron is always reduced to $Fe^{2+}$ and

where necessary charge neutrality is achieved via holes in the valence band. This scheme implies that greigite is not semi-metallic in nature.

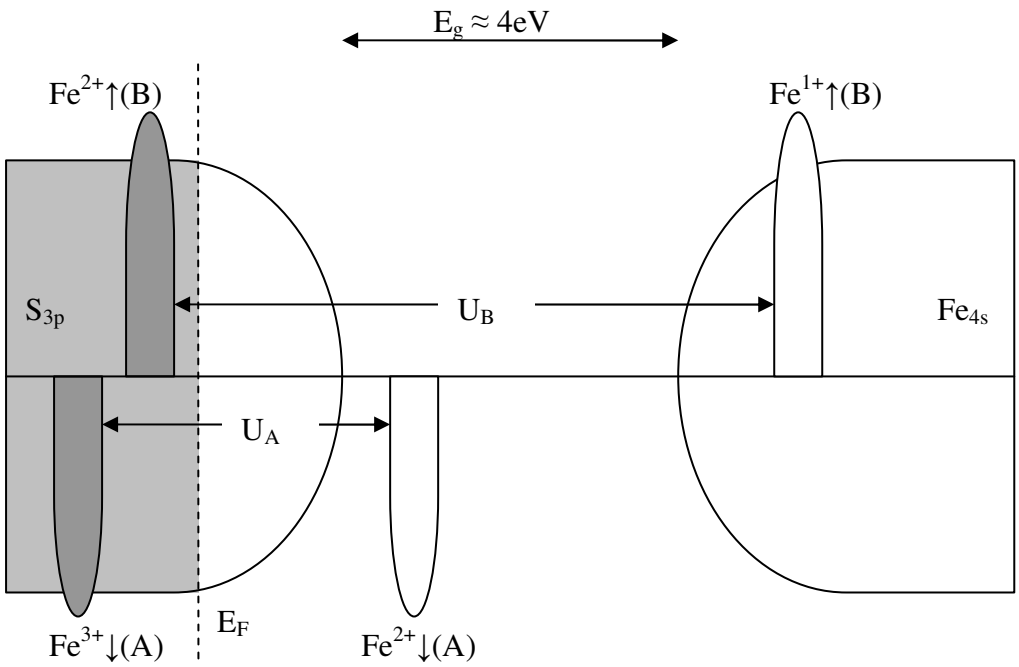


Figure 4.3 – Band scheme for the (ii) scenario of Spender. There is one hole per formula unit, responsible for conduction (note the location of the Fermi level within the $S_{3p}$ band). The ionic terms only are shown, not the one-electron orbitals of figure 4.2. $U_A$ and $U_B$ are the energy required to promote electrons to bands $Fe^{2+}\downarrow(A)$ and $Fe^{1+}\uparrow(B)$ respectively.

Spender *et al.* were unable to determine which, if either, of these band schemes is correct.

A further Mössbauer study of naturally occurring greigite was conducted by Vandenberghe *et al.* (1991) at a range of temperatures from 4.2K up to 500K. It was found that the hyperfine fields for A and B sites "cross-over" at around 300K, and at 5K isomer shifts of 0.37 mm/s for A sites and 0.71 mm/s for B sites were detected, which is interpreted as $Fe^{3+}$ on the A sites and either $Fe^{2+}$ or a mix of $Fe^{2+}$ and $Fe^{3+}$ in

B sites. It is also found that these greigite samples were thermodynamically stable up to at least 480K. In this study no evidence for a low temperature transition was found, and a further study also detected no such transition (Roberts, 1995).

It was suggested by Mott (1980) and tested for greigite by Dekkers *et al.* (2000) that it is possible that many spinel structures do not show a Verwey-type transition upon cooling due to insufficiently stoichiometry samples. Any B-site vacancies present in the structure will lead to the occurrence of localised $FeS_2^{2-}$ via induced non-stoichiometry. It is also possible that such a transition would not be seen using magnetic detection techniques on the greigite samples, although the lack of any abrupt changes in the conductivity upon cooling would seem to suggest that there is no transition (Dekkers *et al.*, 2000). The magnetic behaviour of greigite at low temperatures revealed that the saturation remnant magnetisation increases slowly by 20-30 percent on cooling from room temperature to 4K, with a broad maximum observed at 10K, indicating that a low-temperature transition *may* be present.

Letard *et al.* (2005) explored the possibility that Fe vacancies, leading to non-stoichiometry in the greigite structure, are the reason for the low value of the observed magnetic moment. They note from their X-ray magnetic circular dichroism (XMCD) spectra that of the two samples they examine, one natural and one synthetic, both present similar isotropic cross sections, although their XCMD spectra differ. The XMCD spectrum shows clear signs of Fe-S hybridization. They conclude that the $Fe_3S_4$ structure may be capable of accommodating various electronic and crystallographic modifications ($Fe^{3+}/Fe^{2+}$ ratio or presence of vacancies) so that similar phases could yield quite different XMCD spectra. This is illustrated by an analogy to maghemite ($\gamma$-$Fe_2O_3$) and magnetite ($Fe_3O_4$), where the XMCD signals of $\gamma$-$Fe_2O_3$ and $Fe_3O_4$ are quite different although they are almost indistinguishable by

X-ray diffraction techniques. They attribute features of the difference between $Fe_3S_4$ and $Fe_3O_4$ to a contribution of $Fe^{2+}$ in octahedral sites weaker in $Fe_3S_4$ than in $Fe_3O_4$. It is concluded that the difference observed between the XMCD spectra of $Fe_3S_4$ and $Fe_3O_4$ can be explained by the presence of iron vacancies in $Fe_3S_4$ leading to a lacunary iron sulfide similar to the lacunary iron oxide maghemite $\gamma$-$Fe_2O_3$.

The most recent study of Chang *et al.* (2008) has transformed the understanding of the magnetic behaviour of greigite. It was found that, presumably due to poor stoichiometry of previous samples, the magnetic moment of greigite has been underestimated to a considerable degree. Measurements via high-field experiments give a room temperature value of 3.13 $\mu_B$ / f.u., which increases to 3.35 $\mu_B$ / f.u when extrapolated to 0 K, due to decreased thermal excitation. This contrasts greatly with the value measured previously by Spender *et al.* (1972). Both of these measured values fall short of the value of 4.0 $\mu_B$ / f.u. measured in magnetite (Aragón, 1992), which is also the value predicted from a purely ionic model (4 $\mu_B$ on $Fe^{2+}$ and 5 $\mu_B$ on $Fe^{3+}$). Using the Bloch spin wave expansion method the spin wave stiffness of $Fe_3S_4$ was estimated to be around 193 meV·Å$^2$ from low-temperature saturation magnetisation measurements. The corresponding exchange constant, which quantifies the super-exchange coupling between the two Fe sub-lattices via intermediate S atoms, is estimated to be $J_{AB} \approx 1.03$ meV. This value is also lower than that determined for magnetite (Where $J_{AB} \approx 2.88$ meV) (Uhl & Siberchicot 1995), which is indicative of a smaller degree of magnetic coupling in the sulfide.

Greigite has been reported to possess a very high gyromagnetic remanence (Stephenson & Snowball, 2001), higher than any other material in the literature, and 10 times greater than that observed in magnetite. The gyromagnetic remanence of a material is related to a predominant sense of flip of moments inside the sample as it

rotates in a magnetic field. The origin of this behaviour in greigite is unknown.

It is further reported that the easy axis of greigite is that of the [100] axis (Yamaguchi, 1961), as opposed to the [111] axis seen in magnetite (Heywood *et al.*, 1990). It is unclear how this change in the magnetisation axis arises. No value for the Curie temperature ($T_C$) has been determined for greigite, due to thermal decomposition of this material at elevated temperature (See Dekkers *et al.*, 2000 for a review).

### 4.1.4 Theoretical Studies

Theoretical studies on the greigite structure have met with limited success. Braga *et al.* (1988) undertook spin-polarised multiple scattering calculations for $FeS_6^{n-}$(where n = 8, 9, 10) clusters, where the iron is octahedrally coordinated with the sulfur atoms. This method was unable to offer much insight into the band structure of greigite, and does not answer the questions regarding the origins of electrical conductivity, cation valences or the Fe magnetic moment(s). It does indicate, however, that the Fe-S bonding in greigite is predominately covalent. This would be expected from the simple Pauling model of electro-negativity (Pauling, 1988), which predicts around 20% ionic character for the chemical Fe-S bond, compared to about 50% for the Fe-O bond. It was further suggested by McCammon *et al.* (1992), by analogy with cubanite ($CuFe_2S_3$), that the valences of the Fe atoms represent a rapid electron transfer of delocalised electrons between $Fe^{2+}$ and $Fe^{3+}$ for the greigite octahedra, lending greigite a metallic nature.

It was indicated by Gibbs *et al.* (2007) that the tetrahedral Fe ions in greigite may be tetravalent (4+), based upon considerations of the Fe-S bond length of 2.147 Å and the calculated electron density distributions, $\rho(\mathbf{r})$. The evidence is far from

conclusive, although they venture that the presence of $Fe^{4+}$ would explain the reactivity of greigite. Using the CRYSTAL98 program, the electronic structure was relaxed and bond lengths and theoretical electron density distributions were found. It is determined that the calculated electron density for the tetrahedral Fe-S bond in greigite (0.73e/Å$^3$) was commensurate with the oxidation state of the tetrahedrally coordinated Fe in greigite taking the value 4+, although no attempts were made to optimise the structure or account for magnetic moments. By analogy with the $H_4FeS_4$ molecule, which has tetravalent $Fe^{4+}$, they find a very similar bond length (2.130 Å) and electron density (0.73e/Å$^3$) to that observed for greigite, while the Laplacian $\nabla^2\rho(\underline{r}_c)$ for greigite (4.88 e/ Å$^5$) is overestimated by about 15% to that found for the $H_4FeS_4$ molecule (4.30 e/ Å$^5$). Bader charges of the Fe atoms in the sulfides are determined and values of $Fe^{0.93+}Fe_2^{1.03+}S_4^{0.75-}$ are found for greigite. This is again compared to the $H_4FeS_4$ molecule with values of $H_4^{0.02+}Fe^{0.88+}S_4^{0.20+}$. It is noted however that as the atomic basins for a gas-phase molecule like $H_4FeS_4$ are of infinite dimension and those for a crystal like greigite are finite, it is not clear to what extent the charges for the two systems can be compared.

### 4.1.5 Monoclinic $Fe_3S_4$

Fleet *et al.* (1982) studied a new phase of $Fe_3S_4$, termed monoclinic $Fe_3S_4$, found in pyrrhotite grains. This phase was found to be isostructural with monoclinic $Fe_3Se_4$ (Okazaki and Hirakawa, 1956) and monoclinic $Cr_3S_4$ (Jellinek, 1957), which both take a derivative NiAs structure. This phase consists of $Fe_2S_2$ layers alternating with vacancy layers (figure 4.4), producing a layered structure of sheets. Although this phase of monoclinic $Fe_3S_4$ is polymorphic with greigite, it is extremely unlikely that

this phase is related to any reversible low-temperature transition in greigite, due to the massive structural rearrangement which would be required.

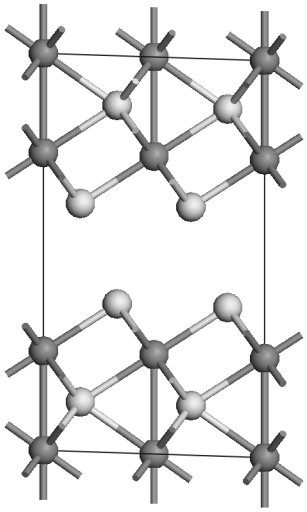

Figure 4.4 – Structure of monoclinic $Fe_3S_4$, determined by Fleet (1982), viewed along the y axis.

### 4.1.6 The Verwey Transition

Upon cooling at ambient pressure, magnetite ($Fe_3O_4$) undergoes a Verwey transition at 121K (Verwey & Haayman, 1941) where resistivity drops 2 order of magnitude, a band gap of ~0.14eV opens and the spinel structure (*Fd3m*) lowers its symmetry to the monoclinic *Cc* structure. The resulting structure is depicted in figures 4.5(a), (b) and (c).

(a)

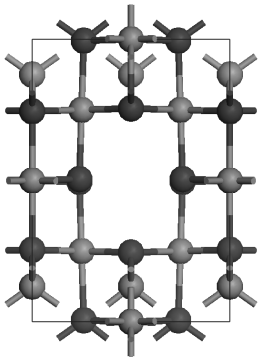

(b)

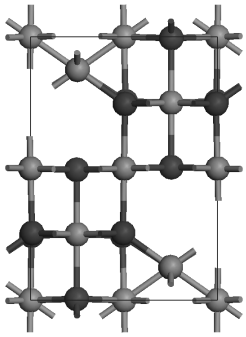

(c)

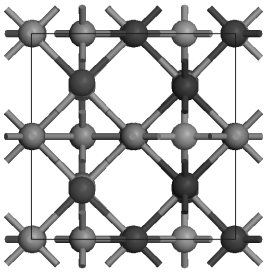

Figure 4.5 (a), (b), (c) – Monoclinic structure of magnetite viewed along the x (a), y (b) and z (c) axes (Wright, 2002). Fe atoms are shown in light gray, S atoms in dark gray.

This monoclinic form of $Fe_3O_4$ has a 28-atom unit cell, due to a halving in the *c* lattice parameter, and its electronic and magnetic structure is a major research topic in solid state physics. It would be of interest to investigate whether a similar transition takes place in isostructural greigite, $Fe_3S_4$.

## 4.2 Greigite Modelling: Spinel Structure

### 4.2.1 Introduction

There remain a number of important questions regarding the properties and behaviour of greigite which are well suited to investigate by using DFT techniques. Both the electronic and magnetic behaviour remain unclear, with reports of inverse spinel behaviour in the majority, but a confusing variety of Mössbauer spectroscopy data which has proved difficult to interpret. In addition, the most recent measure of the magnetic moment per formula unit has substantially increased the estimate of its value from 2.2 μB to 3.35 μB, and theories developed to explain the former value require

revision. Low-temperature studies of greigite have been unable to provide a definitive confirmation of the existence of any structural transition in greigite, analogous to the Verwey transition in magnetite. It is also possible that such a transition may not be discernable using the empirical methods applied so far.

The central aim of this chapter will be to investigate the electronic structure of $Fe_3S_4$. In the same vein as recent studies into magnetite (Anisimov *et al.*, 1997; Pinto & Elliot, 2006; Piekarz *et al.*, 2007), the importance of on-site Fe electronic correlation, represented by the Hubbard $U_{eff}$ parameter, is investigated. A monoclinic form of greigite is proposed in analogy to that found in low-temperature magnetite, and its electronic structure is determined.

### 4.2.2 Spinel Structure

This section uses the GGA and GGA+U formalisms of DFT in order to reproduce the experimental properties of greigite, and hence to offer an insight into this iron sulfide. The experimental greigite structure of Uda is taken as the starting point (Uda, 1965). The tetrahedrally coordinated Fe are henceforth referred to as $Fe_A$, and the octahedral as $Fe_B$.

### 4.2.3 Preliminary GGA Results

The first calculations perform full relaxations of the unit cell volume and shape, in addition to the ionic and electronic coordinates. The Hubbard $U_{eff}$ is set to 0 eV, and three initial magnetic arrangements are:

1. *Non-magnetic arrangement* – No magnetic moments specified.

2. *Normal spinel arrangement* – 8 $Fe^{3+}$ in tetrahedral coordination (5 electrons) and 16 $Fe^{2+}$ in octahedral coordination.
3. *Inverse spinel arrangement* – Possesses 8 $Fe^{2+}$ in tetrahedral coordination and 16 $Fe^{2.5+}$ in octahedral coordination.

A Monkhorst-Pack grid of even numbers of k-points is tested for convergence, along with the Gaussian smearing method with a smearing parameter of 0.02 eV. The electronic convergence condition is set to 0.0001 eV and energy cutoff values of 500, 600 and 700eV are selected in order to test for convergence with respect to basis set size.

Table 4.1 – Summary of results for $U_{eff}$ = 0 eV fully relaxed greigite spinel structure with ENCUT = 500 eV for the three initial magnetic arrangements. [a] is from (Skinner *et al.*, 1964) and [b] from (Chang *et al.*, 2008).

| | a (Å) | S coordinate | Mag mo. ($\mu_B$ / f. u.) | Energy (eV) |
|---|---|---|---|---|
| **NM** | 9.48 | 0.2549 | 2.08 | -351.37 |
| **Inverse** | 9.48 | 0.2549 | 2.08 | -351.37 |
| **Normal** | 9.48 | 0.2549 | 2.08 | -351.37 |
| **Expt.** | 9.88 | 0.2505[a] | 3.35[b] | |

Table 4.1 presents the results of the relaxations for the three initial magnetic arrangements using a basis set energy cutoff of 500eV. All initial magnetic arrangements produce the same ferrimagnetic final structure, which is cubic with a relaxed lattice parameter of 9.48Å, in fair agreement with the experimentally determined $Fe_3S_4$ structure. Table 4.2 repeats the relaxation of the greigite structure using a basis set energy cutoff of 600 eV.

Table 4.2 – Summary of results for U = 0 eV fully relaxed greigite spinel structure with ENCUT = 600 eV. [a] is from (Skinner *et al.*, 1964) and [b] from (Chang *et al.*, 2008).

| MAGMOM | a (Å) | Mag mo. ($\mu_B$ / f. u.) | Energy (eV) |
|---|---|---|---|
| **NO** | 9.48 | 2.17 | -351.39 |
| **INVERSE** | 9.48 | 2.17 | -351.39 |
| **NORMAL** | 9.48 | 2.17 | -351.39 |
| **Expt.** | 9.88[a] | 3.35[b] | |

As for the case with ENCUT = 500 eV, all initial starting magnetic arrangements relax to the same ferrimagnetic structure. The same relaxations were undertaken at 700eV, and exactly the same results were obtained, indicating that convergence with basis set cutoff energy occurs at 600 eV.

The convergence of the k-point grids was tested for Monkhorst-Pack grids of 2x2x2, 4x4x4 and 6x6x6, for cell relaxations at a basis set cutoff energy of 600eV. The results of these calculations are given in table 4.3.

Table 4.3 – Convergence of lattice parameters and internal energies with k-point grid.

| | | Full Cell Relax | Ionic Relax | Singlepoint |
|---|---|---|---|---|
| **k-points** | **a (Å)** | **Energy (eV)** | **Energy (eV)** | **Energy (eV)** |
| 2x2x2 | 9.48 | -351.53 | -351.51 | -351.51 |
| 4x4x4 | 9.48 | -351.40 | -351.39 | -351.39 |
| 6x6x6 | 9.47 | -351.42 | -351.40 | -351.40 |

The simulations demonstrate good convergence using a k-point grid of 4x4x4, which provides a good balance between accuracy and efficient use of processor time. The relaxation using a k-point grid of 6x6x6 was found to be computationally expensive and was unnecessary for the very small improvement in convergence.

In summary, all of these results demonstrate that the calculations are well converged using a k-point grid of 4x4x4 and a basis set energy cutoff of 600 eV. The

lattice parameters predicted from this simulation fall short of the experimentally determined values by 4%, and the unit cell volume by a considerable 13%. In addition to the difficulties in predicting the structure, the calculated magnetic moment of 2.17 $\mu_B$ / f.u. is also underestimated compared with the value of 3.35 $\mu_B$ / f.u. predicted by Chang *et al.*, (2008). The calculated magnetic moment can be broken down into individual contributions from each sub-lattice (table 4.4).

Table 4.4 – Bader charges and magnetic moments for atomic sites in greigite spinel for pure GGA calculations

| Sub-lattice | Population | Bader Charge (e) | Mag. Mo. ($\mu_B$) |
|---|---|---|---|
| $Fe_{tet}$ | 8 | +1.00 | -1.68 |
| $Fe_{oct}^{(1)}$ | 4 | +1.15 | +1.88 |
| $Fe_{oct}^{(2)}$ | 4 | +1.15 | +1.93 |
| $Fe_{oct}^{(3)}$ | 8 | +1.15 | +1.95 |
| S | 32 | -0.83 | +0.00 |

The Bader charges associated with each atom indicate that a lower number of electrons is associated with the Fe atoms on tetrahedral sites, and these can be considered roughly as $Fe^{3+}$. Greater numbers of electrons are associated with the octahedral sites, and these are presumably $Fe^{2+}$. Thus for the $U_{eff}$ = 0 eV case, greigite could be described as having character closer to normal spinel than inverse. There is no breaking of the S sub-lattice atom electronic symmetry; all S atoms reduce 0.83 $e^-$ from the Fe sublattice. The $Fe_B$ sites show a very small variability with regard to magnetic moment, but none with respect to Bader charge.

These results show that pure GGA is unable to describe the greigite structure or magnetic arrangement accurately. The investigation is extended to test the application of a Hubbard U value to these calculations.

### 4.2.4 GGA+U Simulations

In order to determine whether the introduction of a $U_{eff}$ parameter improves the GGA description of greigite, suitable values for this parameter are introduced into full cell relaxation simulations for this structure. The same procedure is used as in the pure GGA simulations described in section 4.2.3, with a full relaxation of cell size, shape and internal coordinates, followed by a relaxation of only the internal ionic coordinates and a final single-point relaxation of the electronic energy only. $U_{eff}$ values from 0.5 eV to 5 eV are applied, in intervals of 0.5 eV. The calculation parameters which ensured convergence in the pure GGA case of section 4.2.3 are used: a basis set cut-off energy of 600 eV and a k-point grid of 4x4x4.

The cell relaxations produce a cubic unit cell structure for all $U_{eff}$ values tested, with all three lattice parameters equal and all angles at 90°. As was seen in the $U_{eff}$ = 0 eV simulation, the initial applied magnetic moment has no impact on the eventual result; as long as the calculations are spin-polarised and sensible magnetic moments are set, the calculations converge to identical structures. Magnetically, stable ferrimagnetic structures are found for all $U_{eff}$ values under investigation. The calculated lattice parameters for each value of $U_{eff}$ are shown in figure 4.6.

The introduction of the $U_{eff}$ parameter has a significant impact upon the predicted lattice parameters, acting to compensate for the overbinding effect seen in the pure GGA case and yielding the experimentally determined lattice parameters at a $U_{eff}$ of between 1 and 1.5 eV.

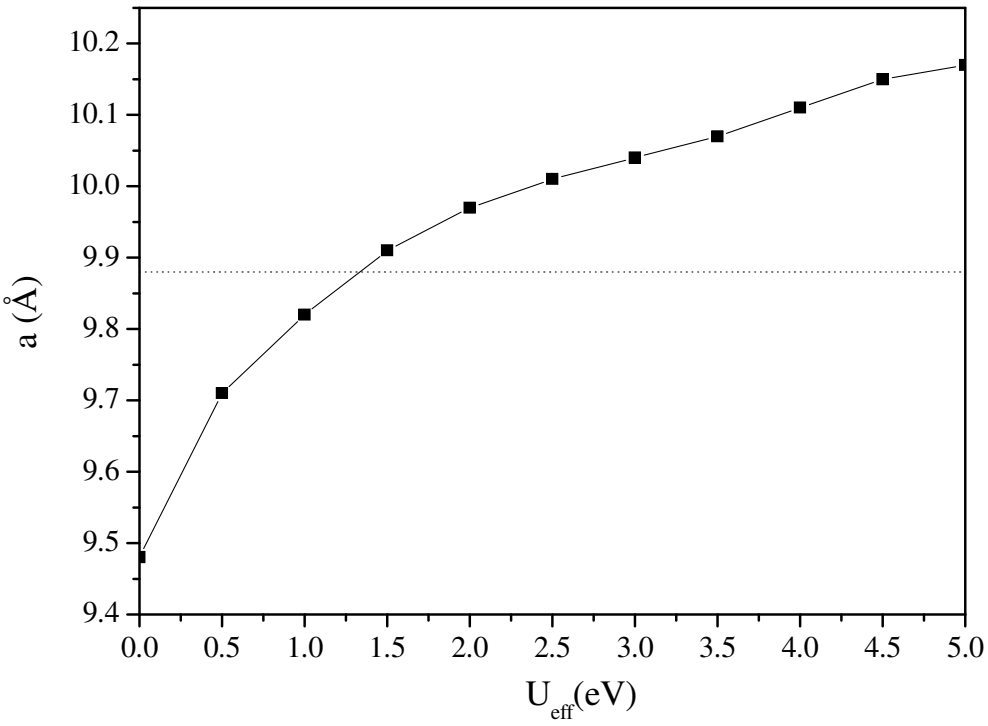


Figure 4.6 – Plot of the calculated lattice parameter for the cubic spinel structure of greigite as a function of the effective Hubbard parameter $U_{eff}$. The dashed line shows the experimentally determined value for the *a* lattice parameter (Uda, 1965).

It is worth noting that this value is similar to the value of $U_{eff}$ found to give an accurate description of troilite (Hexagonal FeS); indeed the relationship between predicted unit cell volume (the cube of figure 4.6) and $U_{eff}$ is similar to that seen for troilite (Rohrbach *et al.*, 2003). The experimental value for the S *u* parameter (0.2505), which represents the first internal S coordinate within the unit cell, is well reproduced for all $U_{eff}$ values.

A plot of the magnetization per formula unit versus $U_{eff}$ for the spinel structure is given in figure 4.7(a), and a plot of the magnitude of the individual magnetic moment from each sublattice is shown in figure 4.7(b).

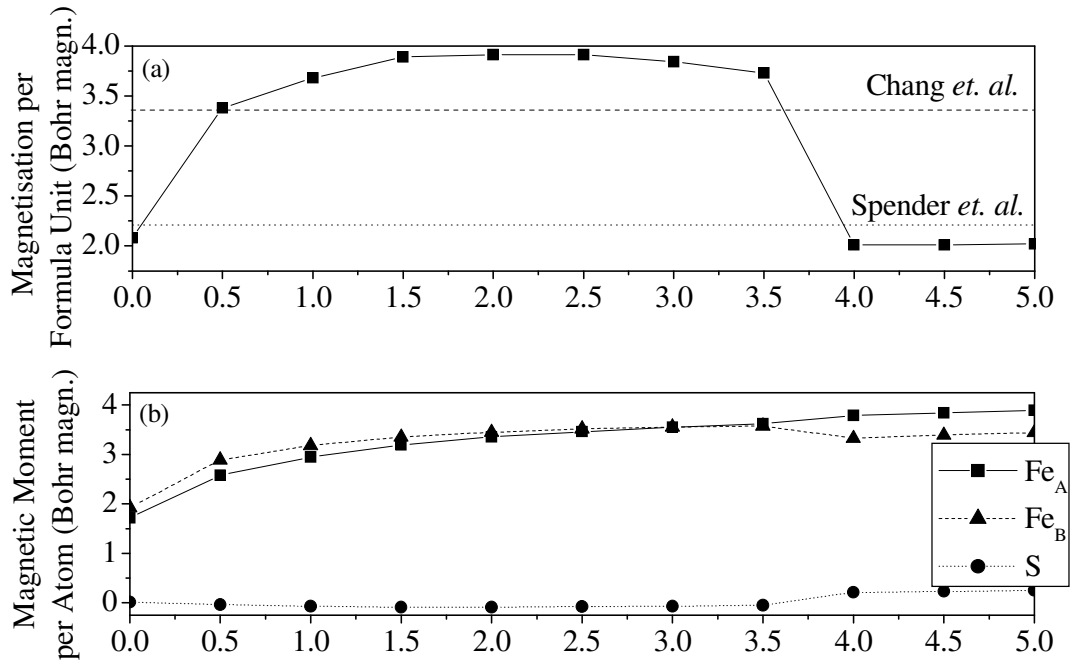


Figure 4.7 (a), (b) – (a) Magnetisation per formula unit versus $U_{eff}$ for the spinel structure of greigite. The dashed line gives the experimental value of Chang *et al.* (2008) and the dotted line the value of Spender *et al.* (1972). (b) Magnitude of the magnetic moments on each sublattice of greigite versus $U_{eff}$. Note that the tetrahedral and octahedral moments are aligned in an anti-parallel manner.

The magnetic moment on each site is found using a Bader analysis, where the electron spin density associated with each atom is integrated over the Bader volume of the atom in question (Bader *et al.*, 1987). The use of Bader analysis is justified by the fact that the effective radius of an ion changes with the oxidation state, and therefore it is not correct to perform the integration around a sphere of constant radius, when considering mixed-valence systems such as greigite. This eliminates one source of arbitrariness arising from variable atomic radius.

The magnetic moments associated with the Fe atoms in the $U_{eff}$ = 0 eV

simulation are calculated to be much lower than either the value reported for the tetrahedral sites in the case of magnetite of -3.82 $\mu_B$ (there are no reported values for the octahedral sites) (Rakcecha and Satya Murthy, 1978) or those which would occur in the purely ionic case of integer unpaired electrons (4.0 $\mu_B$ / f.u.). In total, these moments give a net magnetisation per formula unit of only 60 % the experimentally determined value (Chang *et al.*, 2008). It is concluded that this low value arises from an overestimation of the covalency of the Fe-S bond by the pure GGA, leading to unphysical pairing of electrons.

Introducing the $U_{eff}$ parameter leads to a marked increase in the total magnetisation, caused by an underlying increase in the magnetic moments on both the $Fe_A$ and $Fe_B$ sites. For an applied $U_{eff}$ value of 2 eV, the total magnetisation reaches a maximum of 3.9 $\mu_B$ / f.u., close to the value of 4 $\mu_B$ / f.u. predicted by a purely ionic model. At this $U_{eff}$ value the magnetic moments associated with the $Fe_A$ and $Fe_B$ atoms are determined as -3.26 $\mu_B$ / f.u. and 3.44 $\mu_B$ / f.u. respectively. The magnetic moment on the octahedral Fe atoms reaches a maximum magnitude of 3.61 $\mu_B$ at $U_{eff}$ = 3.5 eV, and at this point the magnetic moments of both the tetrahedral and octahedral sites are equal in magnitude. For the range of applied $U_{eff}$ from 0 to 3.5 eV the S atoms possess negligible magnetic moments; however from $U_{eff}$ = 4 eV upwards each S atom possesses a nonzero magnetic moment of magnitude 0.2 $\mu_B$, parallel in direction to that of the $Fe_A$ atoms. Associated with this, a difference of 0.44 $\mu_B$ develops between the magnetic moments of the Fe atoms on the tetrahedral and octahedral sites, with magnitudes of 3.84 $\mu_B$ and 3.30 $\mu_B$ on the tetrahedral and octahedral sites respectively. These two factors act to reduce the net total magnetic moment to a value of only 2.0 $\mu_B$ / f.u. for values of $U_{eff} \geq$ 4eV. It is noted that the experimentally determined value for the magnetic moment of 3.35 $\mu_B$/f.u. is achieved

at around $U_{eff}$ = 0.5 or 3.7 eV.

The variation in the Bader charge population associated with the $Fe_A$, $Fe_B$, and S sites with the applied $U_{eff}$ parameter is shown in figure 4.8.

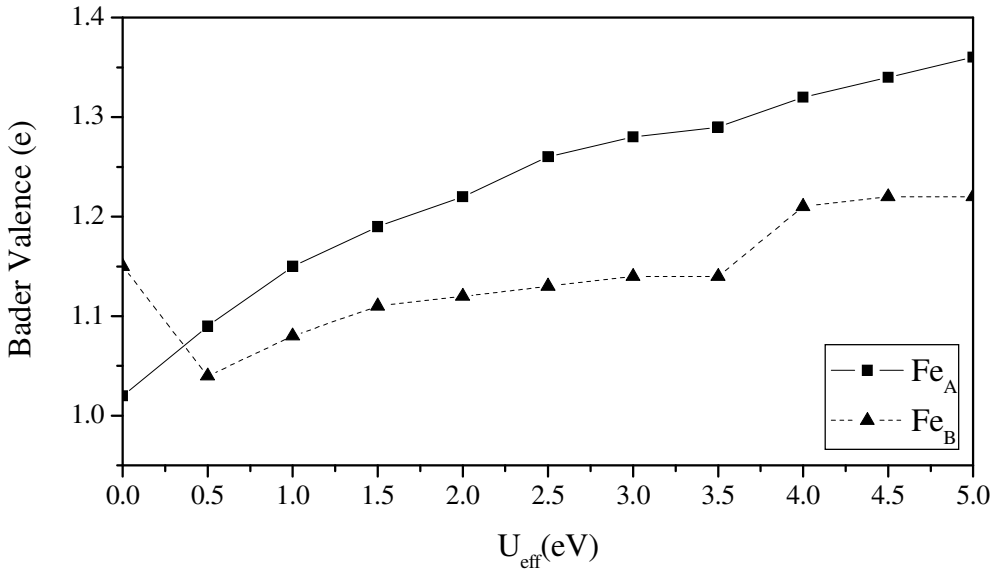


Figure 4.8 – $Fe_A$ and $Fe_B$ atomic Bader valences versus $U_{eff}$ value.

For the case of $U_{eff}$ = 0 eV, these populations indicate that there is a greater number of electrons on the $Fe_A$ atoms than the $Fe_B$; such an arrangement corresponds to the electronic structure of a normal spinel (based on the assumption that the greater number of electrons signifies a valence of $Fe^{2+}$ and a lesser number of electrons denotes a share of $Fe^{2+}$ and $Fe^{3+}$). The introduction of the $U_{eff}$ parameter, even a value of only 0.5 eV, causes the valence of the $Fe_A$ sites to increase relative to those of the $Fe_B$ sites with the effect that there is a crossover of the valences of these sub-lattices. Thus more valence electrons are associated with the B sites than the A sites, a situation which corresponds to that of an inverse spinel. This remains true for all simulations that apply non-zero $U_{eff}$ values. It can be inferred from these results that

the introduction of the $U_{eff}$ parameter has the effect of shifting the electronic structure of greigite from that of the normal spinel to that of the inverse spinel. Since it is the inverse spinel that is observed experimentally, this is a strong indication of the importance of the $U_{eff}$ parameter in the description of greigite. Between values of $U_{eff}$ = 3.5 and $U_{eff}$ = 4 eV, the $Fe_B$ atoms experience a sudden increase in Bader valence, where 0.06 $Fe_B$ electrons are transferred to the S atoms (the S act to reduce the $Fe_B$). This scenario is noted to correspond to the second band picture suggested by Spender *et al.* (1972), where the $Fe_B$ are reduced by S.

Figures 4.9(a), (b), (c) show the electronic density of states (DOS) of the spinel form of greigite for the $U_{eff}$ = 0, 1 and 5 eV cases respectively. The DOS determined in the case where $U_{eff}$ = 0 eV (figure 4.9(a)) shows that the available states at the Fermi level arise from both the spin-down $Fe_B$ sites and the spin-up $Fe_A$ sites. This situation is very different from that seen in similar simulations of the magnetite structure using $U_{eff}$ = 0 eV (Piekarz *et al.*, 2006), where even for the pure GGA the $Fe_A$ do not contribute available states at the Fermi level.

The strong effect of the $U_{eff}$ parameter upon the $Fe_A$ bands around the Fermi level is clearly seen in the DOS for the $U_{eff}$ = 1 eV case (figure 4.9(b)). In this case a gap of 0.3 eV opens between the *e* and $t_2$ 3*d* energy levels of the $Fe_A$ band, while the $Fe_B$ band is largely unaffected compared to $U_{eff}$ = 0 eV. This leads to a semi-metallic band structure for greigite, with the spin-down $Fe_A$ minority band providing states at the Fermi energy and a band gap in the $Fe_A$ spin-up band.

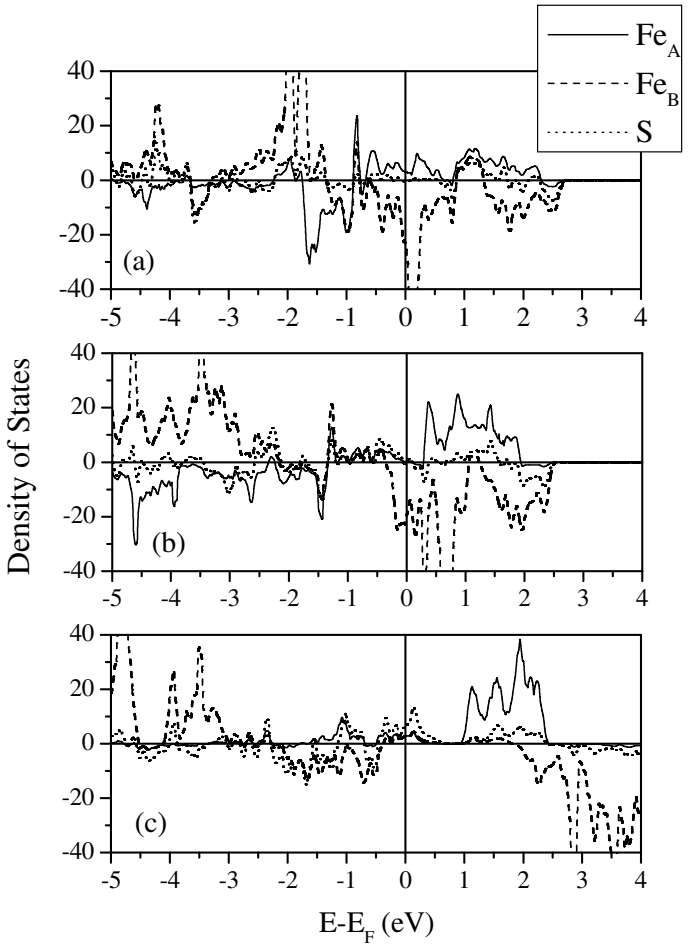


Figure 4.9 (a), (b), (c) – Electronic DOS for the spinel form of greigite for (a) $U_{eff}$ = 0 eV, (b) $U_{eff}$ = 1 eV and (c) $U_{eff}$ = 5 eV. The contributions from each sublattice are plotted.

Figure 4.9(c) shows the DOS for simulations with an applied $U_{eff}$ = 5 eV, and this shows that for large $U_{eff}$ values a splitting of the spin-down $Fe_B$ band occurs, clearly revealing the $t_{2g}$ and $e_g$ energy levels of the *3d* orbital. The $Fe_B$ *d*-orbital spin-down band no longer occupies the energies around the Fermi level, and the semi-metallic behaviour seen in the $U_{eff}$ = 1 eV case disappears. The majority of states are provided by holes in the spin-up S band, with small spin-up contributions from both the tetrahedral and octahedral Fe sub-lattices.

## 4.3 Greigite Modelling: Monoclinic Structure

### 4.3.1 Introduction

As mentioned in section 4.1.3, experimental investigations carried out at low temperature have been unable to provide a definitive answer as to the existence of any Verwey-type temperature-dependent transition in the greigite structure. The difficulties which arise when examining this problem theoretically stem from the lack of any starting structure that a hypothetical form of low-temperature $Fe_3S_4$ may take.

It is noted that studies using the GGA+U theoretical framework have proved successful in the description of the low temperature monoclinic form of magnetite (Piekarz *et al.*, 2007). DFT calculations with a suitable applied $U_{eff}$ parameter working at 0 K have successfully simulated the monoclinic structure and demonstrated that it possess a lower energy than the spinel. $U_{eff}$ values of 3.2 eV (Piekarz *et al.*, 2007) and 3.8 eV (Pinto & Elliot, 2006) have provided good matches to structural and electronic properties in both spinel and monoclinic $Fe_3O_4$. It is logical that if a low-temperature form of greigite does exist, it would be close to isostructural with its oxide relative. By analogy with this structure, a hypothetical monoclinic form of greigite is postulated, and GGA+U simulations are used to determine its energetic stability compared to the spinel structure.

The postulated monoclinic $Fe_3S_4$ structure is based upon the monoclinic $Fe_3O_4$ structure determined by Wright *et al.* (2002) (figure 4.5(a), (b), (c)). In order to account for the larger anion radius in the sulfide compared to the oxide the lattice parameters are scaled accordingly. The scaling constant for each orthogonal lattice direction is given by the ratio of the $Fe_3S_4$ spinel lattice constant $a_{grei}$ to that of the corresponding $Fe_3O_4$ spinel lattice constant $a_{mag}$, giving $a_{grei}/a_{mag} = 9.88/8.39 = 1.18$.

Scaling each monoclinic $Fe_3O_4$ lattice parameter by this factor gives values of $a$ = 6.99 Å, $b$ = 6.98 Å and $c$ = 19.75Å for the hypothetical monoclinic $Fe_3S_4$ structure. The β angle applied to the structure is the same as that seen in monoclinic magnetite, 90.237° (Wright *et al.*, 2002).

### 4.3.2 GGA+U Simulations

The same simulation procedure as for the spinel structures are repeated for a range of $U_{eff}$ values from 0 eV to 5 eV, in steps of 1 eV. The applied basis set cutoff energy is 600eV, and the k-point grid is adjusted to 4x4x2 to account for the doubling of the lattice in the $c$ lattice direction. A supercell of 1x1x2 is used so that the correct 56 atoms are considered, and the results directly comparable with the spinel case. All relaxations yield stable monoclinic structures, with lattice parameters given in Table 4.5. The angle β is predicted to be very close to 90° for all applied $U_{eff}$ value.

Table 4.5 – Calculated lattice parameters and band gap width for the theoretical monoclinic form of greigite, for a range of $U_{eff}$ tested. The differences in the internal energies ΔE of the 56-atom unit cells of the spinel and monoclinic forms of greigite over the range of $U_{eff}$ values modelled are also given.

| $U_{eff}$ (eV) | a (Å) | b (Å) | c (Å) | Band Gap (eV) | ΔE (eV) |
|---|---|---|---|---|---|
| 0 | 6.57 | 6.75 | 18.99 | 0.00 | 1.15 |
| 1 | 6.79 | 6.87 | 19.52 | 0.00 | 2.69 |
| 2 | 6.93 | 6.96 | 19.84 | 0.06 | 3.69 |
| 3 | 6.96 | 6.99 | 20.02 | 0.16 | 4.55 |
| 4 | 7.09 | 7.16 | 20.21 | 0.14 | 2.71 |
| 5 | 7.29 | 7.24 | 20.61 | 0.29 | 0.92 |

The variation in total magnetisation per formula unit for the 56-atom monoclinic unit cell of greigite with $U_{eff}$ is shown in figure 4.10. For values of $U_{eff}$

less than 4eV monoclinic structures with net magnetisations of 1.7 to 2 $\mu_B$ / f.u. are found (figure 4.10), indicating that if a transition to this structure did occur at low temperatures it would be accompanied by a large, observable reduction in the magnetic moment.

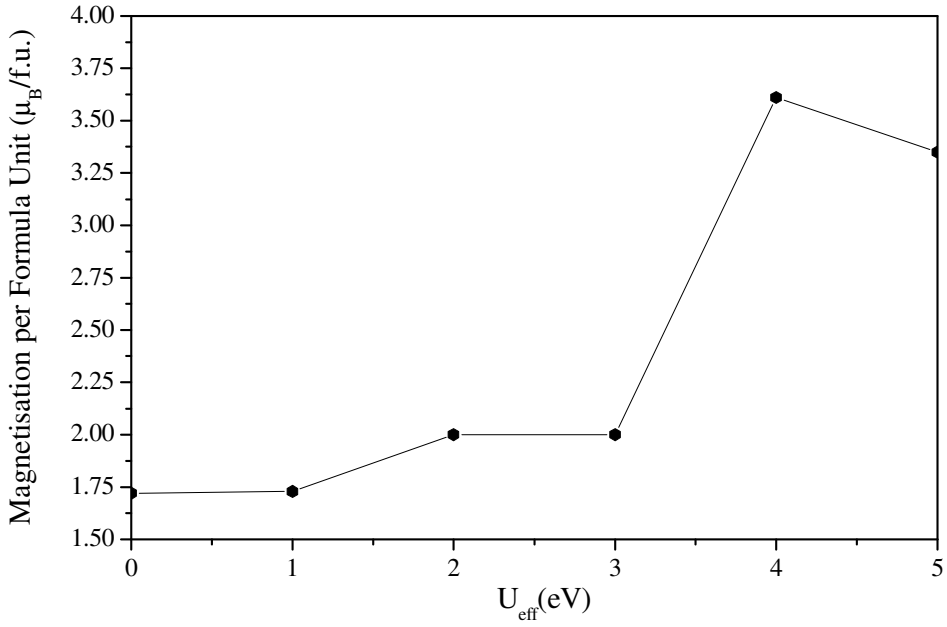


Figure 4.10 – Plot of magnetisation per formula unit versus applied $U_{eff}$ value.

For values of $U_{eff}$ of 4eV and greater, the predicted magnetisation is around 3.7 $\mu_B$ / f.u., similar to that seen in the spinel case. Examining the sub-lattice contributions to the magnetisation per formula unit, it is noted that for low $U_{eff}$ values there is a splitting of the symmetry of the $Fe_B$ sites to the degree that the magnetic moment of half of these sites is 60% greater than that of the other half. For values of $U_{eff} \geq$ 4eV, the electronic structure becomes even more complex, with four groups of four $Fe_B$ sites. This symmetry splitting occurs in a manner similar to the charge disproportionation seen in the low-temperature phase of magnetite (Pinto & Elliot, 2006). The values of the band gap for each $U_{eff}$ value are listed in Table 4.5.

The electronic DOS for the monoclinic form of greigite for $U_{eff}$ values of 0 eV, 1eV and 5 eV are shown in figures 4.11(a), (b) and (c) respectively.

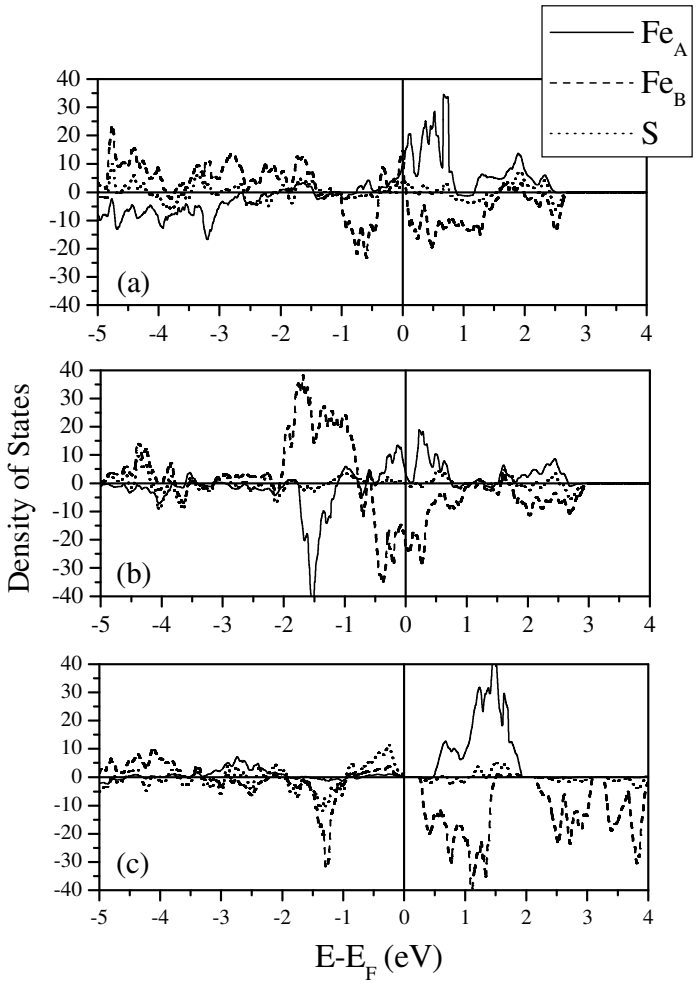


Figure. 4.11 (a), (b), (c) – Electronic DOS for the monoclinic form of greigite with (a) $U_{eff}$ = 0 eV, (b) $U_{eff}$ = 1 eV and (c) $U_{eff}$ = 5 eV. Contributions from each of the atomic sublattices are plotted.

For the case of $U_{eff}$ = 0eV, the available states at the Fermi level are all up-spin, with contributions from $Fe_A$, $Fe_B$ and S sub-lattices. As $U_{eff}$ is increased to 1 eV a band gap is seen to open in the $Fe_A$ band. For $U_{eff}$ = 5 eV a band gap for both $Fe_A$ and $Fe_B$ sub-lattices opens and the structure becomes insulating, similar to that

observed in simulations of monoclinic magnetite (Piekarz *et al.*, 2007).

The difference in the internal energies of the spinel and monoclinic structures ($\Delta E$) for the range of $U_{eff}$ values is given in Table 4.5. This shows that from the calculated total energies of the two structures the monoclinic form is only metastable with respect to the spinel. The precise energy difference between the two depends on the values of $U_{eff}$, but for all values the spinel structure is energetically favoured.

## 4.4 Summary

In this section a rigorous GGA+U approach has been used to investigate the energetic, electronic and magnetic properties of spinel and calculated monoclinic form of $Fe_3S_4$. Simulations of the spinel structure over the range 0 eV $\leq U_{eff} \leq$ 5 eV result in stable ferrimagnetic structures, with Fe atoms on the tetrahedral and octahedral sub-lattices aligned in an anti-parallel manner in accord with published experimental findings. GGA in the absence of any $U_{eff}$ correction leads to a large underestimation of the lattice parameter and the magnetic moment, as well as an electronic arrangement whereby the Bader charges of the tetrahedral and octahedral Fe sites form a normal spinel arrangement. These errors are thought to arise from the GGA failing to take into account the electron correlation associated with the Fe atoms. The experimentally determined inverse spinel structure is correctly simulated upon the introduction of the local Coulomb interaction accounted for by $U_{eff}$. Small values of $U_{eff}$, of the order of 1 eV, produce a crucial improvement in the description of greigite, with the experimentally determined values for the lattice parameters and magnetic moments reproduced accurately. $U_{eff}$ values greater than 3 eV produce solutions where the net magnetic moment is reduced by the occurrence of a magnetic moment on individual S

atoms, anti-parallel to that found on the octahedral Fe sites. This is accompanied by a decrease in the number of electrons associated with the octahedral Fe atoms, which are transferred to the S atoms.

The two band schemes suggested by Spender *et al.* (1972) for the electronic structure of greigite can now be reconsidered in the light of these results. The first scheme, where the octahedral Fe sites of greigite are occupied by a combination of ferric and ferrous iron is the scenario supported by our calculations for $U_{eff} \leq 3$ eV. The second scheme, where the S ions reduce the ferric Fe ions so that all Fe in greigite is ferrous, is seen when $U_{eff} \geq 3.5$ eV. It is not possible to discern the most correct value of $U_{eff}$, based only on the results presented here. However, since the experimental magnetisation and the cell parameters are better reproduced at low $U_{eff}$ values, we would suggest the use of $U_{eff} = 1$ eV for the GGA+U modelling of greigite. For this $U_{eff}$ value the band structure calculations show greigite to be a semi-metal, with the minority-spin band of the Fe octahedral sites providing charge carriers at the Fermi level. Further experimental investigations would be necessary in order to test this prediction.

Simulations of the theoretical monoclinic structure of greigite, based upon the low-temperature magnetite structure, have shown that this form is not energetically favourable compared to the spinel structure for any $U_{eff}$ values between 0 eV and 5 eV, indicating that greigite should not experience any Verwey-type transition to a monoclinic structure at low temperatures. Whilst the mechanics of the Verwey transition are still an open area of research with many unanswered questions, previous *ab initio* calculations (Piekarz *et al.*, 2007) have highlighted the importance of electron correlations in the transition, represented by a $U_{eff}$ correction of around 3.2 eV or greater. Our calculations have shown that the stabilisation of the monoclinic

greigite structure with respect to the spinel would require unrealistically high values of $U_{eff} > 5$ eV. Since it has been shown in this study that an accurate description of greigite is provided by a much lower $U_{eff}$ value of 1 eV, it is postulated that the electron correlation associated with the Fe atoms in greigite is insufficient to facilitate a Verwey-type transition.

The finding that greigite is a ferrimagnetic semi-metal, which conducts in only one spin-polarisation, places greigite within a very select group of materials with important applications in the field of spintronics (Wolf *et al.*, 2001), which could be particularly relevant since iron sulfides offer scope for doping and other manipulations not possible in oxides (Katsnelson *et al.*, 2008). In addition, greigite offers a much better example of a low-temperature iron spinel than magnetite, since it does not undergo a spinel transformation at low temperature.

# 5. Cubic FeS

## 5.1 Introduction

The iron sulfide mineral "cubic FeS" was first identified by de Médicis (1970) as a corrosion product of metallic Fe in aqueous $H_2S$ solution and the absence of air; the product was found to be metastable when not in contact with the $H_2S$ solution. Cubic FeS has since been found in certain strains of magnetotactic bacteria, and its presence is thought to explain the puzzling identification of pyrite in some magnetosome crystals (Mann *et al.*, 1990), presumably due to the difficulty in distinguishing between pyrite and cubic FeS using SAED (Selected Area Electron Diffraction) patterns (Pósfai *et al.*, 1998b). The observation that this phase may be a biogenic material (Rickard & Morse, 2005) proved to be an important factor in the interpretation of FeS minerals found in the Martian meteorite ALH84001 (Pósfai *et al.*, 1998a).

### 5.1.1 Room-Temperature Structure

Cubic FeS is the Fe end-member of the sphalerite series, $Zn_{1-x}Fe_xS$, where

x = 1 corresponds to cubic FeS. This phase takes the same ambient temperature sphalerite structure as the other members of this mineral family, zincblende ($F\bar{4}3m$; space group 216; face centered cubic unit cell). XRD measurements by de Médicis

(1970) found this phase possesses the lattice parameters $a = b = c = 5.423 \pm 0.001$ Å at 25ºC, with a Fe-S bond length of 2.348 Å. This structure is depicted in figure 5.1.

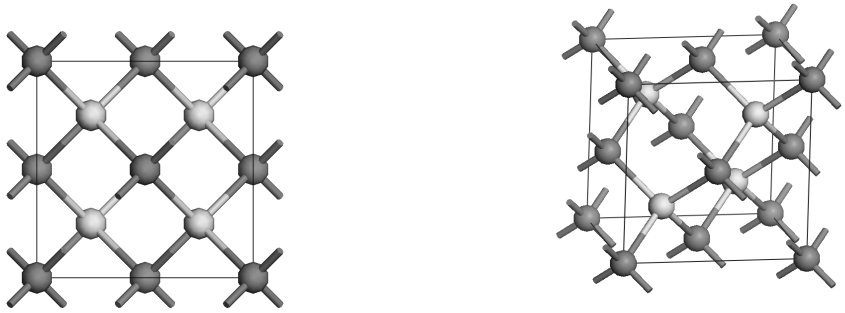

(a) (b)

Figure 5.1 (a), (b) – The sphalerite (zincblende) structure of cubic FeS at ambient temperature, viewed along the *a* axis (a), and off-axis (b). The S atoms are arranged on the nodes of a face-centered cubic lattice, while one half of the tetrahedral holes are occupied by the Fe atoms (de Médicis, 1970).

Cubic FeS was also reported by Takeno *et al.*, (1970), who found (at room temperature) the strongest X-ray diffraction reflections from the (111), (220) and (311) planes of cubic FeS together with a lattice parameter of $a = 5.417 \pm 0.004$ Å, confirming the structure predicted by de Médicis. A small non-stoichiometry in favour of Fe surplus was found (a range of $Fe_{1.003}S$ to $Fe_{1.102}S$). A later study using Mössbauer spectroscopy (Wintenberger *et al.*, 1978) found the Fe atoms in cubic FeS to be exclusively high-spin and in the +2 oxidation state. The high-temperature magnetic structure was determined to be that of a paramagnet.

Little empirical research exists on the electrical behaviour of cubic FeS, however it was found by Deulkar *et al.* (2002) that the electronic bandgap in Fe-rich sphalerite decreases with increasing Fe concentration, suggesting either semiconducting or metallic behaviour for the cubic FeS endmember.

### 5.1.2 Formation of Cubic FeS

Murowchick & Barnes (1986) studied the formation of cubic FeS crystals from iron metal in $H_2S$ solution. This phase was found to compete with both troilite and mackinawite, with the best-formed cubic FeS crystals deposited at pH between 4 and 5, and temperatures between 35°C and 60°C. The resulting cubic FeS crystals took slightly modified tetrahedral, negative tetrahedral, and on rare occasions cubic, crystal habits. It is suspected that cubic FeS is a significant corrosion product of steel pipes when in contact with hydrogen sulfide saturated water, although cubic FeS tends to only form in situations of short timescales and is rarely observed (Shoesmith *et al.*, 1980).

### 5.1.3 Conversion to other FeS phases

It has been found that cubic FeS converts to greigite via the mackinawite phase (Murowchick & Barnes, 1986). Investigations into the transformation of cubic FeS into mackinawite found that this was a solid-state process, and occurred over a period of 35 to 96 hours at 21°C; incomplete conversion leads to the presence of cubic FeS grains in mackinawite crystals and their existence was found to stabilise the thermal decomposition of the resulting mackinawite (Shoesmith *et al.*, 1980). It has been noted that Cubic FeS only differs significantly from the tetrahedral mackinawite structure in the distribution of Fe atoms, and the close structural similarity between these structures is considered to account for the ease of transition between these phases (Murrowchick & Barnes, 1986).

### 5.1.4 Low Temperature Transition

Wintenberger *et al.* (1978) studied cooled samples of cubic FeS using XRD and determined that this phase undergoes a first order crystallographic transition at 234K. This takes the form of a structural symmetry change from cubic to orthorhombic, with the unit cell lattice parameters becoming:

$$a' = 5.54 \text{ Å} \quad b' = 5.487 \text{ Å} \quad c' = 5.195 \text{ Å}$$

when measured at 81K. The only space group corresponding to this observed unit cell is F222 (symmetry number 22) with Fe in 4a(000) symmetry 222 (D2) and S in 4c Wyckoff positions. The Fe-S bond length was found to be 2.342 Å.

Further to these measurements, Mössbauer spectroscopy and neutron diffraction measurements (Wintenberger & Buevoz, 1978) of this orthorhombic phase have shown that a first order magnetic transition occurs around 237K, and below this temperature the Mössbauer spectra is indicative of an ordered magnetic phase. The first order magnetic transition at 237K and the first order crystallographic transition at 234K are almost certainly related, and the suggestion that there is a range of transition temperatures due to slight non-stoichiometry suggests with reasonable certainty that there is a simultaneous crystallographic and magnetic first order transition around 234K. The Mössbauer data of the low temperature phase show that every Fe atom behaves like a standard ferrous ($Fe^{2+}$) ion. The neutron diffraction measurements indicate that the magnetic moments are either parallel or anti-parallel to the *a* axis, aligned in ferromagnetic (001) planes that couple antiferromagnetically. The magnetic moment of the iron atoms in the orthorhombic low temperature structure is reported as $3.45 \pm 0.15\ \mu_B$ at a temperature of 40 K. This falls short of the saturation moment of the $Fe^{2+}$ ion of 4 $\mu_B$, indicating a degree of covalency in the Fe-S bond. The magnetic space group is reported to be F22'2'. The experimentally determined

structure and magnetic moment arrangement for this low-temperature orthorhombic structure is shown in figure 5.2.

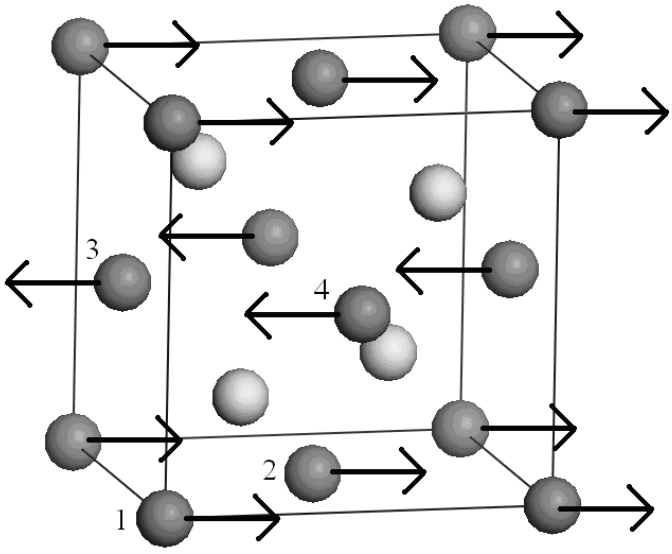


Figure 5.2 – Crystal structure of the antiferromagnetic low-temperature orthorhombic phase of cubic FeS. The directions of the magnetic moments of the Fe atoms are shown with arrows. The different Fe atoms in the unit cell are denoted by the indices 1-4.

Wintenberger *et al.* (1978) suggested three possible mechanisms for the cubic to orthorhombic low-temperature transition: (i) Generalised exchange interactions in the presence of orbital degeneracy; (2) Exchange magnetostriction in the presence of Jahn-Teller coupling; and (3) Spin-orbit coupling of magnetisation and Jahn-Teller distortions. Of these explanations, (1) is considered to be possible, whilst the other two mechanisms are unlikely to be sufficiently strong to cause a structural transition.

### 5.1.5 Computational Studies

Welz and Rosenberg (1987) undertook the modelling of cubic FeS using the linear

muffin tin orbital approach of DFT. Non-magnetic calculations found the structure to be a conductor of electrons, with the Fermi level cutting the continuous Fe 3*d* band. The Fe-S bond is considered to be of predominantly ionic character, and differences between this phase of FeS and mackinawite are chiefly attributed to the Fe-Fe interaction in mackinawite. Spin-polarised calculations on the cubic FeS structure reveal two stable self-consistent magnetic solutions, where the result depends on the initial splitting of the bands. Both of these cases are ferromagnetic, and the moments on the Fe atoms are given as 0.78 $\mu_B$ and 3.34 $\mu_B$ respectively, with the smaller value obtained for an initial splitting below 1 $\mu_B$. They attribute the slightly lower than expected value for pure $Fe^{2+}$ as due to the contribution of Fe *d* electrons to the Fe-S bond. In the case of ferromagnetic spin polarisation the phase remains metallic, but this does not definitely preclude the possibility that a gap opens for antiferromagnetic polarisation as observed for the transition-metal monoxides (Terakura *et al.*, 1984) or chalcopyrite (Hamajima, 1981). Calculations on Fe-S clusters by Lie & Taft (1983) gave a similar outcome, where an isolated ($FeS_4$) cluster was found to possess a moment of 3.43 $\mu_B$.

Neither of these studies is able to account for the low-temperature orthorhombic distortion, and in addition to reproducing the experimentally determined antiferromagnetic polarisation with planes of uniform spin orientation parallel to one of the cubic faces, a realistic magnetic calculation should also take into account the orthorhombic distortion of the low-temperature magnetically ordered state. It is of note that DFT has met with good success in the description of sphalerite, ZnS (Steele *et al.*, 2003), however it should be noted that the magnetic ordering of cubic FeS poses many extra challenges to its description. The next section will apply the computational techniques used in previous sections to the description of both the

high- and low-temperature structures of cubic FeS.

## 5.2 Cubic FeS: Modelling

### 5.2.1 Introduction

In the previous sections it has been demonstrated that, with suitably applied $U_{eff}$ parameters, the GGA+U method is able to provide a successful description of the Fe-S materials mackinawite and greigite. The following section will apply this method, in addition to the interatomic potential derived for mackinawite (section 3.3), in the description of the both the cubic FeS high-temperature and the orthorhombic FeS low-temperature structures.

Two sets of GGA+U calculations are performed. The first use the high-temperature cubic FeS structure of de Médicis (1970) as the initial structure; the second begin with the low-temperature orthorhombic FeS structure determined by Wintenberger *et al.* (1978). Each of these structures is simulated using 4 different starting magnetic arrangements:

1. *Non-magnetic* – non-spin-polarised;
2. Spin-polarised with no initial magnetic moments on the Fe atoms;
3. *Ferromagnetic* **-** all Fe magnetic moments are aligned in a parallel manner. Since the Fe atoms are thought to occur in the +2 oxidation state there are 6 *d*-orbital electrons present, of which 4 are unpaired in the high spin configuration. Thus a magnetic moment of +4 $\mu_B$ is applied to each Fe atom;
4. *Antiferromagnetic* – Due to the presence of four Fe atoms in the unit cell, there

exist 3 possible antiferromagnetic arrangements, consisting of two sets of two opposing Fe magnetic moments. In these calculations the spin arrangement experimentally determined by Wintenberger & Buevoz (1978) is used, and it is this arrangement which is illustrated in figure 5.2. The other possible antiferromagnetic arrangements are presented in figure 5.3.

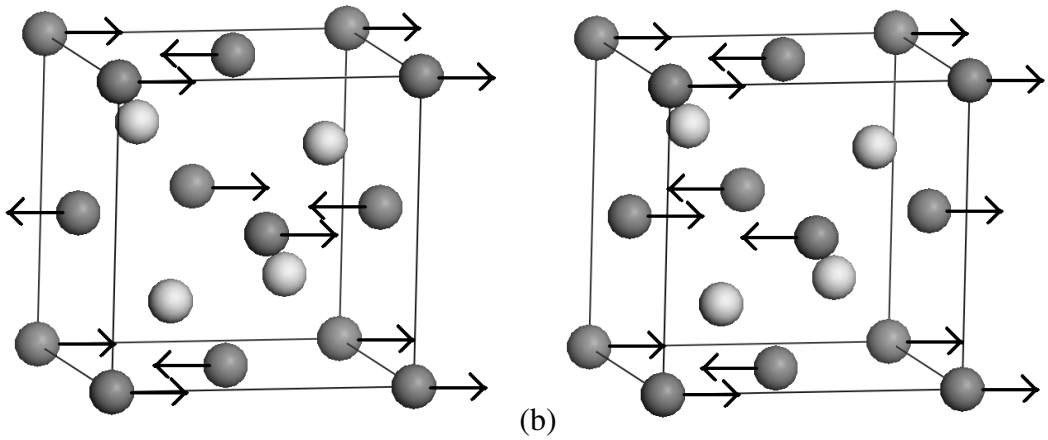


Figure 5.3 (a), (b) – Antiferromagnetic magnetic moment arrangements for the orthorhombic FeS structure. (a) is henceforth referred to as scenario (2), and (b) scenario (3).

Each of these four magnetic arrangements will be tested in both the pure GGA and GGA+U formulations of DFT. A dense Monkhorst-Pack k-point grid of 11x11x11 is used in all calculations, along with Gaussian smearing of the electronic free energy in the vicinity of the Fermi level, where a smearing parameter of 0.02 eV is applied.

All calculations perform, in the following order:

1. Full cell relaxations of the unit cell dimensions, unit cell shape and internal ionic coordinates, together with relaxation of the electronic structure of cubic FeS;
2. This is followed by full relaxations of the ionic coordinates in order to obtain

the ground state ionic configuration;

3. A final relaxation, of the electronic structure only, is undertaken in order to obtain the ground state.

### 5.2.2 Cubic FeS Calculations: Basis Set Convergence

This section details the GGA convergence tests of the basis set cutoff energy for each magnetic arrangement of cubic FeS. Table 5.1 presents the convergence test simulations of the non-spin polarised cubic FeS structure.

Table 5.1 – Basis set cut-off energy with predicted lattice parameter and calculated internal energies for the cubic FeS structure, modelled using non-spin-polarised GGA. The three phases of relaxation of the structure described in the previous section give the calculated lattice parameter and internal energy and given by (1) (cell shape and volume, ionic coordinates and electronic structure), (2) (ionic coordinates and electronic structure) and (3) (electronic structure only).

| | (1) | | (2) | (3) |
|---|---|---|---|---|
| **ENCUT (eV)** | **a (Å)** | **Energy (eV)** | **Energy (eV)** | **Energy (eV)** |
| **400** | 4.945 | -51.972 | -51.926 | -51.930 |
| **500** | 4.946 | -51.940 | -51.940 | -51.944 |
| **600** | 4.946 | -51.946 | -51.946 | -51.944 |
| **700** | 4.946 | -51.942 | -51.940 | -51.944 |

An energy cutoff of 500 eV is found to be sufficient in order to prevent any Pulay stresses on the unit cell, to obtain convergence of the cell parameters and to ensure convergence of the internal energy of the unit cell to within 1 meV.

Table 5.2 presents the results of the convergence calculations using GGA spin-polarised simulations of the cubic FeS structure with no initial Fe magnetic moment.

Table 5.2 – Basis set cut-off energy with predicted lattice parameter, internal energies and Fe magnetic moments for the cubic FeS structure, modelled using spin-polarised GGA with no applied magnetic moment.

| | Full Relax | | Internal Relax | Singlepoint | |
|---|---|---|---|---|---|
| **ENCUT (eV)** | **a (Å)** | **Energy (eV)** | **Energy (eV)** | **Energy (eV)** | **MM/Fe ($\mu_B$)** |
| **400** | 4.947 | -51.972 | -51.926 | -51.941 | 0.42 |
| **500** | 4.946 | -51.949 | -51.940 | -51.954 | 0.42 |
| **600** | 4.946 | -51.946 | -51.941 | -51.944 | 0.00 |
| **700** | 4.946 | -51.961 | -51.959 | -51.944 | 0.00 |

Convergence of all parameters occurs at an energy cutoff of 600eV, and the resulting structure is precisely the same as that found in the non-spin-polarised calculation. This suggests that it will be necessary to introduce initial magnetic moments onto the Fe atoms in order to obtain ordered magnetic arrangements in the pure GGA simulations.

The next convergence test calculations apply magnetic moments to each Fe atom, and these moments are aligned in a ferromagnetic arrangement. The calculated lattice parameters, internal energies and magnetic moments for a range of basis set cutoff energies are given in table 5.3.

Table 5.3 – Basis set cut-off energy with predicted lattice parameters, internal energies and Fe magnetic moments for the cubic FeS structure, modelled using spin-polarised GGA with an applied ferromagnetic magnetic moment.

| | Full Relax | | Internal Relax | Singlepoint | |
|---|---|---|---|---|---|
| **ENCUT (eV)** | **a (Å)** | **Energy (eV)** | **Energy (eV)** | **Energy (eV)** | **MM/Fe ($\mu_B$)** |
| **400** | 4.952 | -51.968 | -51.945 | -51.942 | 0.43 |
| **500** | 4.967 | -51.938 | -51.932 | -51.953 | 0.46 |
| **600** | 4.968 | -51.936 | -51.932 | -51.935 | 0.48 |
| **700** | 4.968 | -51.933 | -51.932 | -51.935 | 0.48 |

These calculations show that the ferromagnetic nature of the structure is only supported in a low-spin form, with very low magnetic moments on each Fe atom of 0.48 $\mu_B$.

The final convergence calculations of the cubic FeS structure in the GGA apply the antiferromagnetic starting magnetic moment arrangement. The results of these calculations are presented in table 5.4.

Table 5.4 – Basis set cut-off energy with predicted lattice parameters, internal energies and Fe magnetic moments for the cubic FeS structure, modelled using spin-polarised GGA with an applied antiferromagnetic magnetic moment arrangement.

| | Full Relax | | | | Internal Relax | Singlepoint | |
|---|---|---|---|---|---|---|---|
| **ENCUT (eV)** | **a (Å)** | **b (Å)** | **c (Å)** | **Energy (eV)** | **Energy (eV)** | **Energy (eV)** | **MM/Fe ($\mu_B$)** |
| **400** | 4.979 | 4.979 | 5.062 | -52.028 | -51.986 | -51.986 | 1.41 |
| **500** | 4.985 | 4.985 | 5.069 | -52.006 | -51.999 | -51.999 | 1.45 |
| **600** | 4.988 | 4.988 | 5.090 | -51.999 | -51.999 | -51.999 | 1.54 |
| **700** | 4.988 | 4.988 | 5.090 | -51.999 | -51.999 | -51.999 | 1.54 |

It is noted that convergence occurs at 600 eV, and since this ensures convergence for all magnetic arrangements tested this value will be used in all calculations throughout this chapter.

### 5.2.3 GGA Simulations

The calculations on the cubic FeS structure for the non-magnetic, spin-polarised (without initial Fe magnetic moments), ferromagnetic and antiferromagnetic arrangements all converge well to ground states. The calculated lattice parameters, internal energies and magnetic moments for each relaxed structure are presented in

table 5.5.

Table 5.5 – Summary of GGA calculations of the cubic FeS structure. The resulting magnetic structures, lattice parameters, internal energies and magnetic moments of the Fe atoms are shown. [a]The experimental data of de Médicis (1970).

| | a (Å) | b (Å) | c (Å) | Energy (eV) | MM/Fe ($\mu_B$) |
|---|---|---|---|---|---|
| **Non-Magnetic** | 4.946 | 4.946 | 4.946 | -51.944 | - |
| **Ferromagnetic** | 4.968 | 4.968 | 4.968 | -51.953 | 0.48 |
| **Antiferromagnetic** | 4.988 | 4.988 | 5.093 | -51.999 | 1.54 |
| **[a]Exp.** | 5.423 | 5.423 | 5.423 | - | - |

The non-spin-polarised, and spin-polarised with no applied magnetic moment, calculations both converge to the same non-magnetic solution; as such these results are henceforth labelled the relaxed non-magnetic structure. For this non-magnetic case the predicted lattice parameter of 4.946 Å and the Fe-S bond distance, calculated to be 2.142 Å (compared to the experimental value of 2.348 Å), indicate a large degree of overbinding predicted in this structure by pure GGA. The non-magnetic calculations also predict Bader charges of 0.93 e for each Fe and -1.07 e for each S atom, indicating that the difference in the charges on each ion is less than 0.15e, and only half the value determined in the non-magnetic pure GGA mackinawite simulations of section 3.2.6. This suggests that the predicted character of the Fe-S bond for the non-magnetic arrangement is more covalent than ionic, and this may cause the overbinding demonstrated in the GGA cubic FeS calculations.

Both the non-magnetic and ferromagnetic starting arrangements converge to similar cubic structures, with no magnetic moment present on the Fe atoms in the non-magnetic starting arrangement and a small magnetic moment of 0.48 $\mu_B$ on the ferromagnetic structure. This is thought to correspond to a low-spin Fe solution for these simulations. The predicted ferromagnetic structure, in a very similar manner to that seen in the non-magnetic case, underestimates the lattice parameters by 12%; this

indicates a large degree of overbinding in the ferromagnetic pure GGA case.

The predicted structure for the antiferromagnetic arrangement also displays overbinding of the lattice parameters, similar to the non-magnetic and ferromagnetic arrangements. The relaxed antiferromagnetic arrangement also demonstrates a very small tetrahedral distortion from the cubic structure, where the *c* parameter is slightly expanded in relation to the *a* and *b* parameters. A magnetic moment of 1.5 $\mu_B$ is found on the Fe atoms, which may also indicate low-spin Fe, although this value is three times that found for the ferromagnetic Fe arrangement, suggesting some kind of intermediate spin state.

The large discrepancies between the experimentally determined lattice parameters and those calculated using the pure GGA indicates that this method is unable to give a good description of cubic FeS in the high-temperature cubic form, regardless of the applied magnetic arrangement.

### 5.2.4 GGA+U Calculations

This section introduces the $U_{eff}$ parameter into the GGA method to test whether this additional term improves the DFT description of the high temperature cubic FeS phase. A range of $U_{eff}$ values, from 0 eV and 4 eV are tested, a range in accordance with previous studies of Fe oxides (Piekarz *et al.*, 2007; Grau-Crespo *et al.*, 2006). All calculations were performed using a basis set cutoff energy of 600eV, with the range of $U_{eff}$ values from 0 to 4 eV separated into intervals of 0.5 eV.

### 5.2.5 Non-Magnetic GGA+U

The predicted lattice parameters and Bader charges for the GGA+U non-magnetic

calculations are given in table 5.6. All simulations, regardless of the applied $U_{eff}$ value, predict cubic structures with $a = b = c$. For all values of the applied $U_{eff}$ parameter the predicted lattice parameters are substantially underestimated. This shows that the overbinding seen in the non-magnetic pure GGA simulations of cubic FeS is not corrected by the introduction of the $U_{eff}$ parameter; in fact the introduction of the $U_{eff}$ parameter to the non-magnetic arrangement has almost no effect upon the description of this material. This is further demonstrated by the lack of any correlation between the applied $U_{eff}$ value and the Bader charge associated with the Fe atoms, which stays fairly constant regardless of the $U_{eff}$ value applied.

Table 5.6 – Calculated *a* lattice parameter and Fe Bader charges from the non-magnetic GGA+U calculations for Cubic FeS.

| **$U_{eff}$ (eV)** | **a (Å)** | **Fe Bader Charge (e)** |
|---|---|---|
| 0 | 4.946 | 0.93 |
| 0.5 | 4.943 | 0.97 |
| 1 | 4.942 | 0.98 |
| 1.5 | 4.940 | 0.98 |
| 2 | 4.939 | 0.98 |
| 2.5 | 4.941 | 0.96 |
| 3 | 4.943 | 0.96 |
| 3.5 | 4.949 | 0.93 |
| 4 | 4.956 | 0.98 |

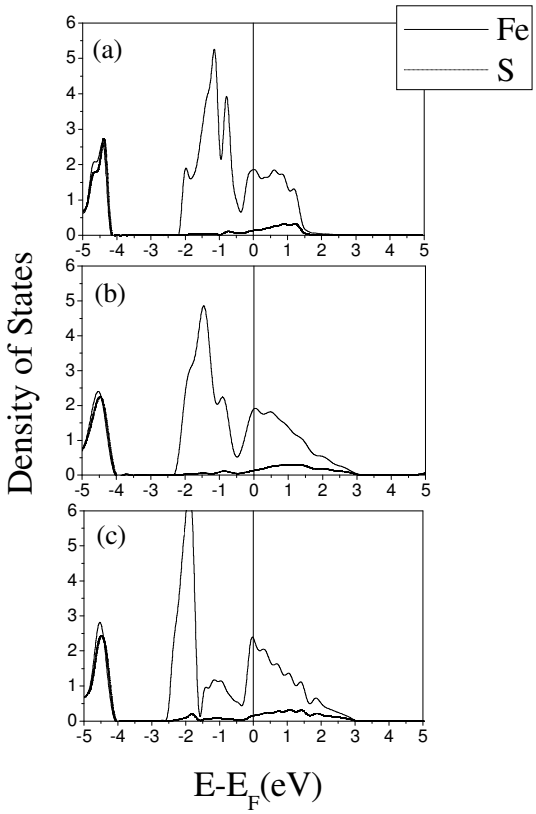


Figure 5.4 (a), (b), (c) – Atomic site contributions to the electronic DOS graphs for the non-magnetic GGA+U calculations with $U_{eff}$ values of (a) 0, (b) 2 and (c) 4 eV for the cubic form of FeS.

The electronic DOS for the non-magnetic cubic FeS GGA+U simulations with U = 0, 2 and 4 eV is presented in figures 5.4(a), (b) and (c). These plots demonstrate that the $U_{eff}$ parameter has little effect on the electronic structure of the non-magnetic arrangement. It is noted that the predicted band structure is similar in form to that found for mackinawite in section 3.2.7, with available Fe bands at the Fermi level indicating a metallic nature.

### 5.2.6 Spin-Polarised GGA+U

Further calculations test the GGA+U method using spin-polarised calculations

without initial Fe magnetic moments for the cubic FeS structure. The results of these calculations are presented in table 5.7.

Table 5.7 – Calculated *a* lattice parameter and Fe magnetic moments from the spin-polarised GGA+U calculations (with no initial Fe magnetic moments) for Cubic FeS.

| $U_{eff}$ (eV) | a (Å) | MM / Fe ($\mu_B$) |
|---|---|---|
| 0 | 4.946 | 0.00 |
| 0.5 | 4.945 | 0.00 |
| 1 | 4.943 | 0.00 |
| 1.5 | 4.940 | 0.00 |
| 2 | 4.941 | 0.00 |
| 2.5 | 5.430 | 3.63 |
| 3 | 5.501 | 3.65 |
| 3.5 | 5.442 | 3.67 |
| 4 | 5.528 | 3.70 |

All simulations, regardless of the applied $U_{eff}$ value, predict cubic structures with $a = b = c$. The introduction of the $U_{eff}$ parameter into GGA+U spin-polarised calculations (with no initial Fe magnetic moment applied) leads to a non-magnetic result for values of $U_{eff}$ less than 2.5 eV. The structures predicted in this case have Fe-S bond lengths and structural lattice parameters which are underestimated compared with experimental values.

Higher values of $U_{eff}$, those greater than 2.5 eV, predict ferromagnetic structures with high-spin Fe, which possess lattice parameters very close to those seen experimentally for the high-temperature, paramagnetic cubic FeS phase.

### 5.2.7 Ferromagnetic GGA+U

Figures 5.5(a) and 5.5(b) (over the page) show the variation of the calculated lattice parameters and Fe magnetic moment, respectively, for the ferromagnetic cubic FeS

arrangement with the range of $U_{eff}$ values applied. For all $U_{eff}$ values the relaxed structures are cubic. Figure 5.5(a) shows that the predicted structures show dramatic increases in both the predicted lattice parameters of the structure and the magnetic moment on each Fe atom due to the introduction of the $U_{eff}$ parameter, and this trend applies even for small values of $U_{eff}$. The predicted lattice parameters for values of $U_{eff}$ between 1.5 eV and 4 eV are very close to those found experimentally, with a value of $U_{eff}$ = 2 eV providing the most accurate match to the experimental value.

Figure 5.5(b) demonstrates that the cubic FeS structure is found to support high-spin Fe magnetic moments for any applied $U_{eff}$ greater than zero. It is further noted, however, that the predicted values for the magnetic moment on the Fe atoms is less than would be expected if all the Fe *d*-orbital electrons were involved in the magnetic moment, suggesting that there is either a degree of covalency in the Fe-S bonds, or that there exists a degree of delocalisation of these electrons, which would be evidenced by a metallic nature similar to that observed in the mackinawite structure.

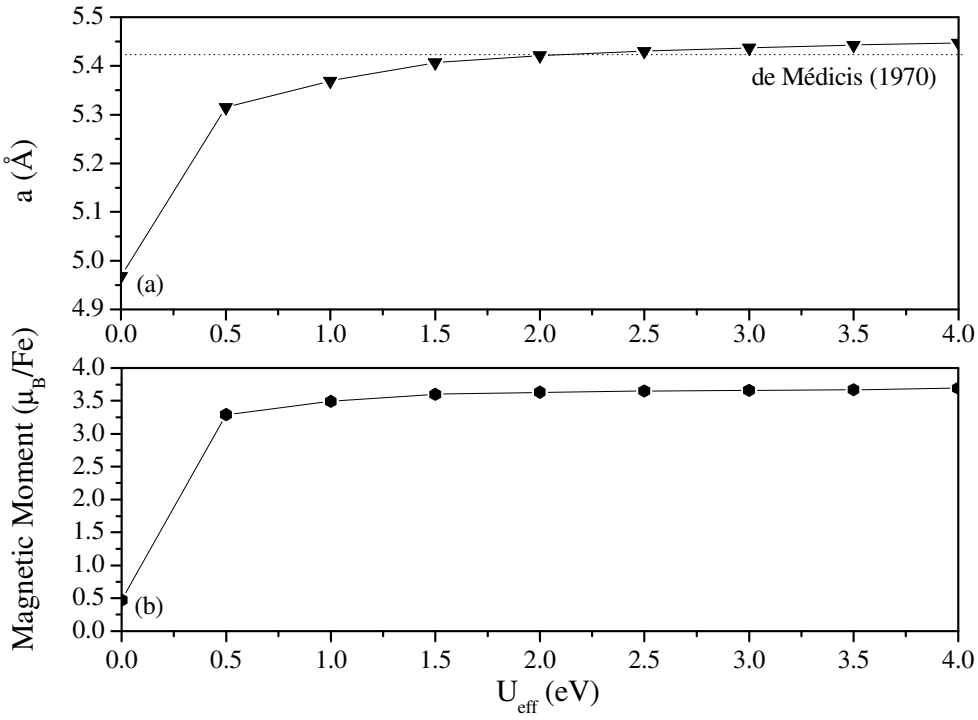


Figures 5.5 (a), (b) – Plots of calculated (a) lattice parameter and (b) magnetic moment encapsulated within Fe Bader basin for the ferromagnetic arrangement of cubic FeS for the range of $U_{eff}$ values tested. The experimentally determined lattice parameter (de Médicis, 1970) for the paramagnetic high-temperature cubic structure is denoted by the dotted line.

Comparing the dramatic difference in the lattice parameters predicted for the non-magnetic and ferromagnetic structures studied so far indicates that, contrary to finding of a previous study (Welz & Rosenberg, 1986), the presence of spin-polarisation has a signficant effect upon the predicted cubic FeS structure, and leads to a far better agreement between the predictions of the lattice parameters in the ferromagnetic case and the experimental values than for the non-magnetic case.

The electronic DOS for the ferromagnetic simulations of the cubic FeS structure are plotted in figures 5.6(a), (b) and (c) for $U_{eff}$ values of 0, 2 and 4 eV

respectively.

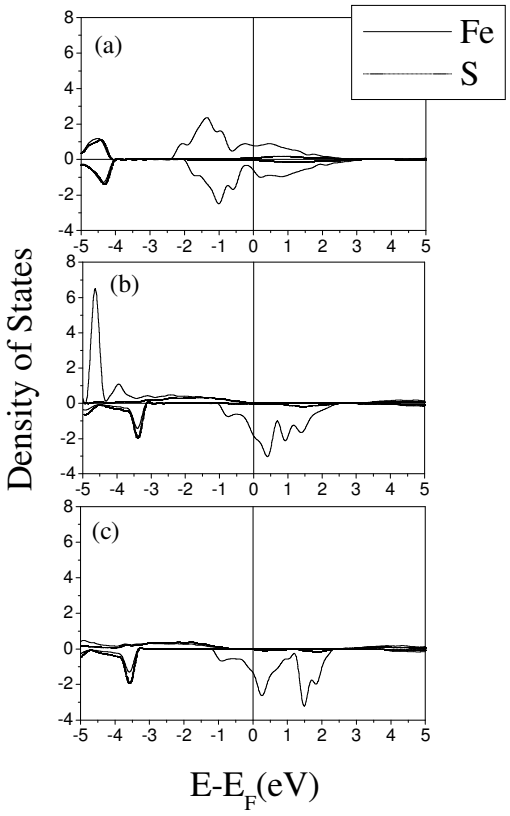


Figure 5.6(a), (b), (c) – Atomic site contributions to the electronic DOS graphs for the ferromagnetic calculations, with $U_{eff}$ values of (a) 0, (b) 2 and (c) 4 eV respectively, for the cubic form of FeS.

The ferromagnetic electronic DOS provide a more nuanced band picture than that of the non-magnetic case. The introduction of the $U_{eff}$ value splits the symmetry of the up- and down- spin polarised bands of the Fe *d*-orbitals. For $U_{eff}$ values of both 2 eV and 4 eV the predicted band structure is that of a semi-metal, where the available states at the Fermi level lie solely in one spin polarisation, with a band gap of approximately 4 eV opening in the other spin direction. However, due to the paramagnetic nature of the high-temperature phase, this would not be seen experimentally due to rapidly changing spin directions in actual samples from thermal

effects. There is no contribution from any S orbitals at the Fermi level, suggesting that conduction arises solely from the electrons occupying Fe *d*-orbitals.

### 5.2.8 Antiferromagnetic GGA+U

Figure 5.7(a) shows the variation of the lattice parameters with $U_{eff}$ in the cubic FeS structure with an initial antiferromagnetic moment arrangement, while figure 5.7(b) shows the analogous relationship between the Fe magnetic moment and $U_{eff}$.

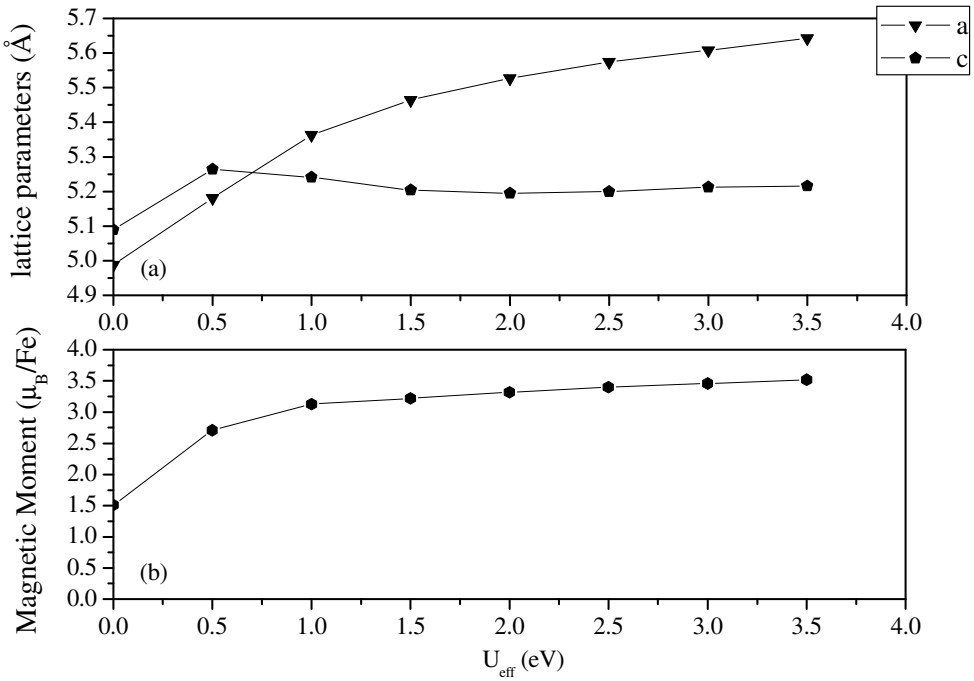


Figures 5.7 (a), (b) – Plots of calculated (a) lattice parameters *a* and *c* and (b) Fe magnetic moment encapsulated within the Bader basin for range of $U_{eff}$ values, for the antiferromagnetic arrangement of cubic FeS.

At all $U_{eff}$ values less than 4 eV a tetrahedral unit cell is predicted, with $a = b$. An elongated *c* parameter with respect to *a* is found for values of $U_{eff} < 1$ eV. This situation is reversed for values of $U_{eff} \geq 1$ eV, where it is predicted that the structure is

instead elongated in both the *a* and *b* direction compared to the *c* direction, due to a significant extension in the *a* and *b* parameters rather than any major change in the *c* direction. At a $U_{eff}$ value of 4 eV, a ferromagnetic cubic structure is predicted, suggesting that applying a large degree of on-site Fe electronic correlation induces a high level of lattice symmetry, making the antiferromagnetic structure collapse to the more symmetric ferromagnetic. None of the values of $U_{eff}$ tested show evidence of causing any orthorhombic distortion in the structure, since for all cases $a = b$. For the antiferromagnetic arrangement, increasing $U_{eff}$ leads to the magnetic moment on each Fe atom increasing in a roughly linear fashion.

Figures 5.8 (a) and (b) show the electronic DOS for the antiferromagnetic arrangement of the cubic FeS structure at $U_{eff}$ values of 0 and 2 eV (the $U_{eff}$ = 4 eV antiferromagnetic arrangement does not exist) respectively.

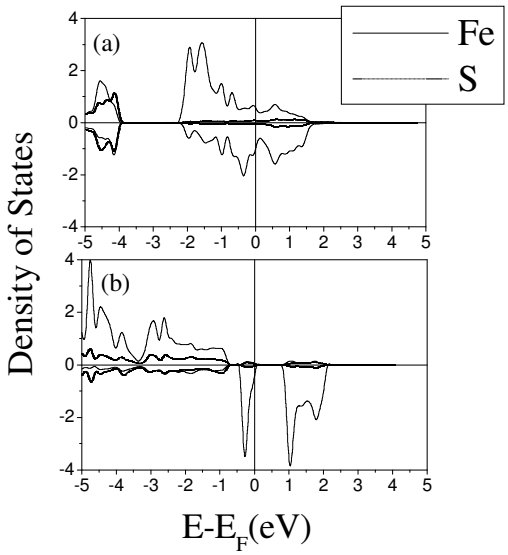


Figure 5.8 (a), (b) – Atomic site contributions to the electronic DOS graphs for the antiferromagnetic case with $U_{eff}$ values of (a) 0 and (b) 2 eV for the cubic form of FeS. Only the electronic DOS for a single spin-polarisation is shown in each case.

The antiferromagnetic electronic DOS demonstrates a similar splitting of the up and down Fe *d*-bands to the ferromagnetic arrangement, where the introduction of the $U_{eff}$ parameter causes the opening of a band-gap, slightly above the Fermi level, in the case of $U_{eff}$ = 2 eV. Since this DOS applies to only one spin-polarisation, it is concluded that the antiferromagnetic structure consists of planes of parallel-polarised Fe atoms behaving in this manner.

### 5.2.9 Comparison of Structures

Figure 5.9 shows the normalised energy differences between the calculated magnetic arrangements for the range of $U_{eff}$ values tested.

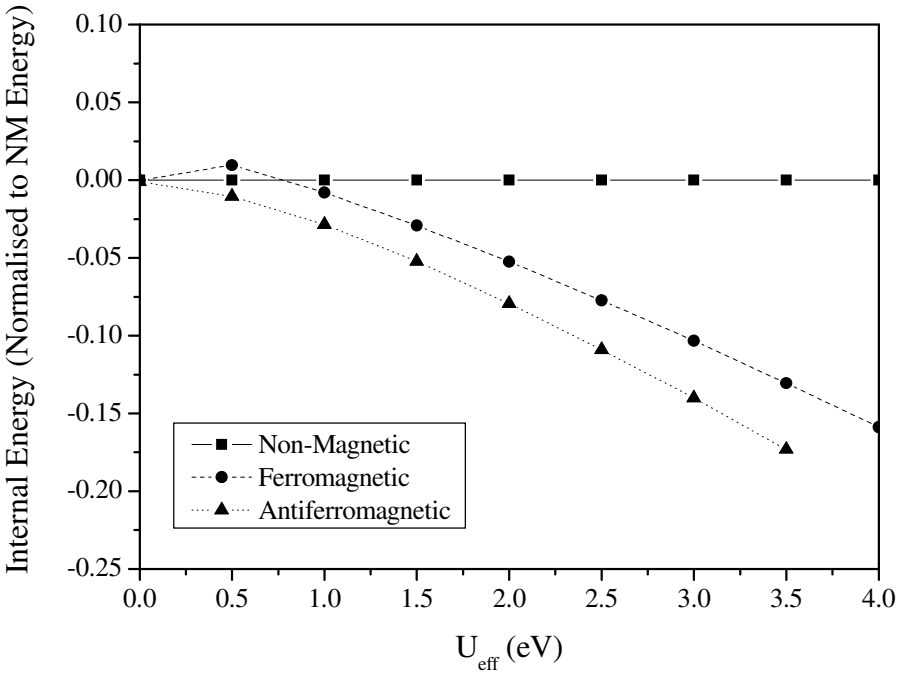


Figure 5.9 – Plot of unit cell internal energy against $U_{eff}$ value for the three magnetic arrangements of the Cubic FeS structure. All energies are normalised to the non-magnetic energies.

With the exception of $U_{eff}$ = 0 eV and 4 eV the antiferromagnetic structure possesses the lowest energy, by a roughly constant margin of around 1.5 eV compared with the ferromagnetic arrangement. The non-magnetic case is the least stable for all $U_{eff}$ values tested with the exception of $U_{eff}$ = 0.5 eV, where the ferromagnetic arrangement is the least stable. These results indicate that the ferrous ion in cubic FeS has a strong preference for a high-spin electron configuration for all $U_{eff}$ values tested, even if this leads to a breaking of the cubic symmetry of the lattice. For $U_{eff}$ = 4 eV, the structure is unable to support an antiferromagnetic arrangement and instead collapses to the ferromagnetic structure. The relaxed structures calculated for the non-magnetic case show only negligible changes upon introduction of the $U_{eff}$ parameter; the lattice parameters remain underestimated to the same degree as in the pure GGA simulations.

### 5.2.10 Interatomic Potential Model: Cubic FeS Structure

Following from the GGA+U calculations of the cubic FeS sturcture, the interatomic potential derived for the mackinawite structure is used to simulate cubic FeS. Since the formal oxidation states of the Fe and S atoms present in cubic FeS are the same as those found in mackinawite, the potential may be applied in this way. It is a measure of the success of a potential that it is transferable to other structures of the same atoms. For this purpose, both the unit cell and the internal coordinates were relaxed. This produces the cubic structure correctly, although the predicted lattice parameter is underestimated at $a = b = c$ = 4.86 Å, i.e. within 0.1 Å of the non-spin-polarised structure that the GGA simulations predict, indicating that the presence of the magnetic moment has considerable magneto-structural effects associated with it; the non-magnetic FeS potential derived for mackinawite is unable to account for such

effects. However, the fact that the interatomic potential predicts the cubic structures to within 0.1 Å of the non-magnetic GGA value is a considerable success for the $Fe^{2+}$, $S^{2-}$ potential derived in this thesis.

## 5.3 Orthorhombic FeS: Modelling

### 5.3.1 Introduction

These calculations use the orthorhombic experimental structure of Wintenberger *et al.* (1978) in order to test if, from this initial structure which does not possess cubic symmetry, the GGA or GGA+U methods are capable of predicting and describing the low-temperature structure. As before, the simulations apply the four initial Fe magnetic moment arrangements. Finally the interatomic potential is tested to determine its ability to predict the orthorhombic structure.

### 5.3.2 GGA Simulations

The first calculations test the GGA method without the $U_{eff}$ parameter, and the results are presented in table 5.8. The pure GGA calculations show the same overbinding tendency in the description of the orthorhombic FeS structure as in the cubic structure, which for all three initial magnetic arrangements leads to a considerable underestimation of each lattice parameter. A very small orthorhombic distortion is seen in the antiferromagnetic simulation, with an elongated *c* parameter and a slightly reduced *b* parameter compared to *a*. The predicted magnetic moments in each case are similar to those found for the initial cubic FeS starting structure.

Table 5.8 – GGA simulation results for the orthorhombic FeS structure. Resulting magnetic structures, lattice parameters, internal energies and magnetic moments of the Fe atoms are shown.

| | a (Å) | b (Å) | c (Å) | Energy (eV) | MM/Fe ($\mu_B$) |
|---|---|---|---|---|---|
| **Non-Magnetic** | 4.952 | 4.949 | 4.937 | -51.944 | - |
| **Ferromagnetic** | 4.955 | 4.955 | 4.954 | -51.956 | 0.45 |
| **Antiferromagnetic** | 4.984 | 4.981 | 5.079 | -51.999 | 1.48 |

These results show that, for the pure GGA, both the cubic and orthorhombic FeS starting structures relax in similar ways for each magnetic arrangement, but that the lower symmetry of the orthorhombic structure gives relaxed structures which are also orthorhombic.

### 5.3.3 Non-Magnetic GGA+U

The effect of the Hubbard $U_{eff}$ parameter in the GGA calculations for the non-magnetic orthorhombic FeS system is simulated. These spin-polarised calculations, with no initial applied magnetic moment, may relax to configurations that are not seen should non-magnetic or high-spin initial starting conditions be applied. As before, a range of $U_{eff}$ values from 0.5 eV to 4 eV are tested in steps of 0.5 eV, for each of the three magnetic arrangements. The results of these calculations are presented in table 5.9.

These results demonstrate, in a similar manner to the cubic FeS starting structure, that the $U_{eff}$ value does not improve the non-magnetic description of the orthorhombic FeS structure if no magnetic moments are applied to the Fe atoms. Both the predicted lattice parameters and the Fe Bader charges show no trend with the $U_{eff}$ parameter.

Table 5.9 – Calculated *a*, *b* and *c* lattice parameters and Fe Bader charges from the non-magnetic GGA+U calculations for orthorhombic FeS.

| $U_{eff}$ (eV) | a (Å) | b (Å) | c (Å) | Fe Bader Charge (e) |
|---|---|---|---|---|
| 0 | 4.952 | 4.949 | 4.937 | 0.93 |
| 0.5 | 4.947 | 4.943 | 4.938 | 0.92 |
| 1 | 4.942 | 4.941 | 4.938 | 0.92 |
| 1.5 | 4.943 | 4.940 | 4.935 | 0.91 |
| 2 | 4.940 | 4.925 | 4.950 | 0.91 |
| 2.5 | 4.944 | 4.941 | 4.936 | 0.93 |
| 3 | 4.941 | 4.950 | 4.941 | 0.93 |
| 3.5 | 4.953 | 4.950 | 4.945 | 0.93 |
| 4 | 4.957 | 4.957 | 4.956 | 0.92 |

Figures 5.10 (a), (b) and (c) show the calculated electronic DOS for the orthorhombic FeS structures, for $U_{eff}$ = 0, 2 and 4 eV respectively, in the non-magnetic arrangement.

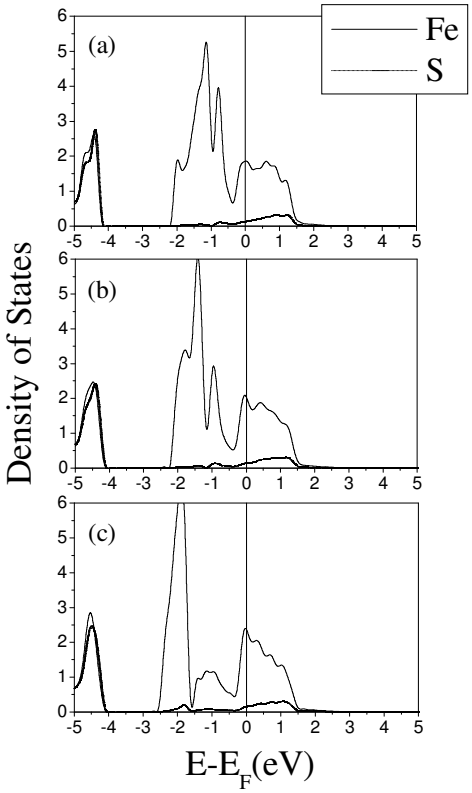


Figure 5.10 (a), (b), (c) – Electronic DOS graphs for the calculations on the

orthorhombic low-temperature structure of cubic FeS. The non-magnetic, ferromagnetic and antiferromagnetic cases are shown for $U_{eff}$ values of (a) 0, (b) 2 and (c) 4 eV.

The non-magnetic orthorhombic FeS DOS plots show very similar behaviour to their cubic FeS counterparts for corresponding $U_{eff}$ values.

### 5.3.4 Spin-Polarised GGA+U

Further calculations test the GGA+U method using spin-polarised calculations, without initial Fe magnetic moments, for the orthorhombic FeS structure. The results of these calculations are presented in table 5.10.

Table 5.10 – Calculated *a*, *b* and *c* lattice parameters and Fe magnetic moments from the spin-polarised GGA+U calculations with no initial Fe magnetic moments for orthorhombic FeS.

| $U_{eff}$ (eV) | a (Å) | b (Å) | c (Å) | MM / Fe ($\mu_B$) |
|---|---|---|---|---|
| 0 | 4.954 | 4.954 | 4.955 | 0.44 |
| 0.5 | 4.958 | 4.956 | 4.954 | 0.58 |
| 1 | 4.963 | 4.960 | 4.965 | 0.68 |
| 1.5 | 4.987 | 4.985 | 4.982 | 0.92 |
| 2 | 5.462 | 5.338 | 5.465 | 3.60 |
| 2.5 | 5.240 | 5.237 | 5.234 | 2.11 |
| 3 | 5.936 | 5.347 | 5.348 | 3.66 |
| 3.5 | 5.520 | 5.517 | 5.513 | 3.68 |
| 4 | 5.743 | 5.743 | 5.239 | 3.69 |

The structures predicted by these calculations demonstrate a clear change in both lattice parameters and magnetic moment between $U_{eff}$ values of 1.5 and 2 eV, even though all calculations predict ferromagnetic arrangements of Fe magnetic

moments. Below $U_{eff}$ = 2 eV the lattice parameters are underestimated as in the non-magnetic calculations, along with small Fe magnetic moments of less than 1 $\mu_B$. For $U_{eff} \geq 2$ eV antiferromagnetic arrangements are predicted, where both the predicted lattice parameters and the Fe magnetic moments are increased, although the relative sizes of each of the three lattice parameters show little correlation with the $U_{eff}$ parameter.

### 5.3.5 Ferromagnetic GGA+U

Figure 5.11(a) and (b) shows the effect of the $U_{eff}$ parameter on the predicted lattice parameters and Fe magnetic moments, respectively, for the initial orthorhombic FeS structure with a ferromagnetic magnetisation as initial arrangement.

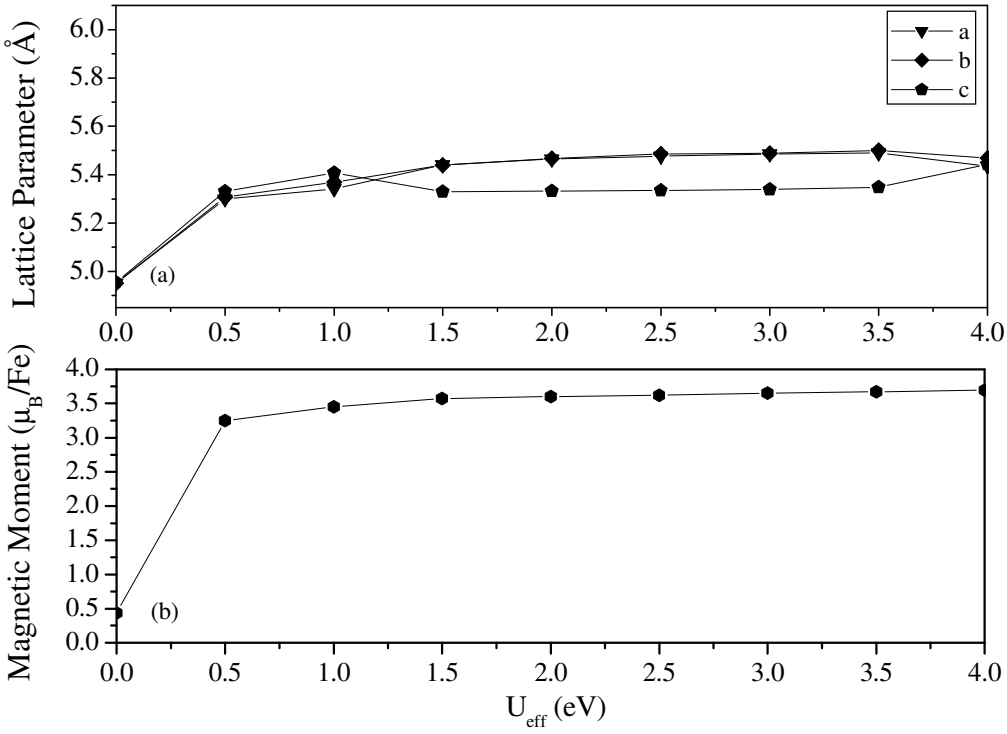


Figures 5.11 (a), (b) – Plots of calculated (a) lattice parameters *a* and *c* and (b) magnetic moment encapsulated within Fe Bader basin for range of $U_{eff}$ values applied

to calculations of the ferromagnetic arrangement of orthorhombic FeS.

The predicted lattice parameters and magnetic moments for the ferromagnetic arrangements show a dramatic increase in both the lattice parameters and magnetic moments with non-zero $U_{eff}$. The lattice parameters show a tendency to either form a cubic structure or show a slight distortion from that cubic structure with an elongated *c* ($U_{eff}$ = 2 eV) or *b* direction ($U_{eff}$ = 3 eV). The magnetic moments show a similar trend to that seen in the cubic case, where the introduction of the $U_{eff}$ parameter leads to a large increase in the magnetic moment. Such an increase can be described in terms of a shift from low-spin Fe for $U_{eff}$ = 0 eV to high-spin Fe for all non-zero $U_{eff}$ values.

Figures 5.12 (a), (b) and (c) show the calculated electronic DOS of the ferromagnetic orthorhombic FeS structure, for $U_{eff}$ = 0, 2 and 4 eV respectively.

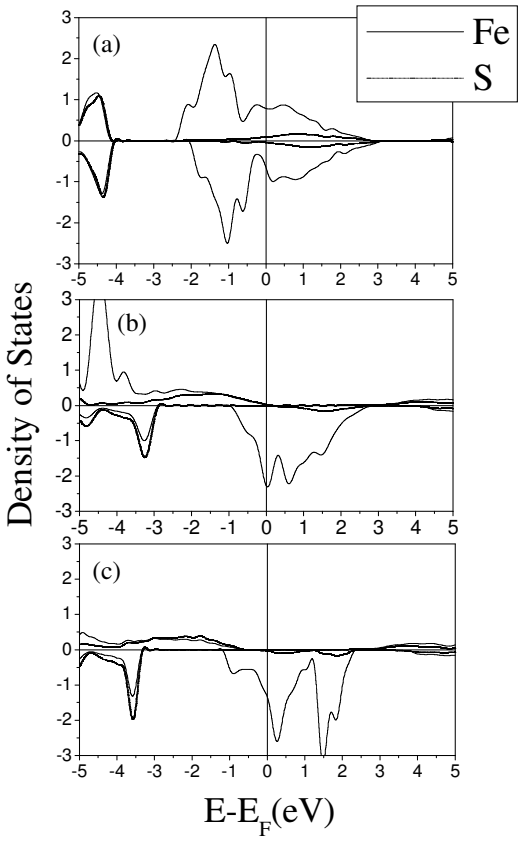

Figure 5.12 (a), (b), (c) – Electronic DOS graphs for the calculations of the ferromagnetic orthorhombic FeS structure for $U_{eff}$ values of (a) 0, (b) 2 and (c) 4 eV.

The ferromagnetic DOS plots show very similar behaviour to their cubic FeS counterparts for corresponding $U_{eff}$ values for the ferromagnetic arrangements, with their semi-metallic appearance when $U_{eff}$ = 2 or 4 eV where the available states at the Fermi level are provided by the spin-down Fe band.

### 5.3.6 Antiferromagnetic GGA+U

The antiferromagnetic calculations of the lattice parameters and Fe magnetic moment are given in figures 5.13 (a) and (b) respectively.

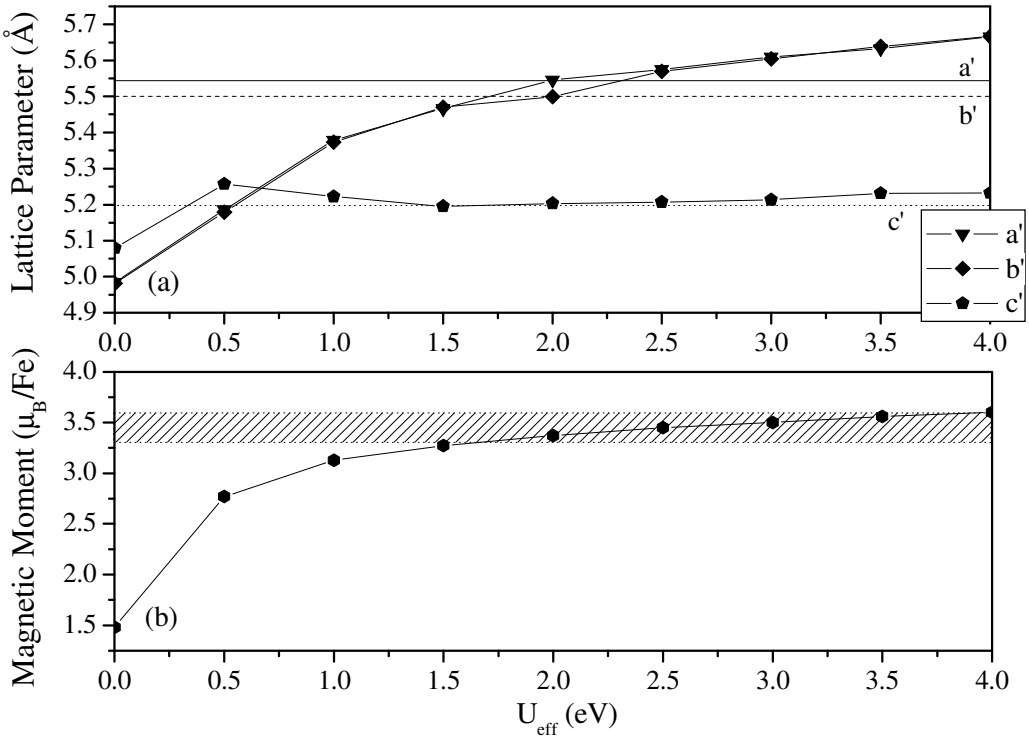


Fig 5.13 (a), (b) – (a) plots the calculated magnetic moment encapsulated within the Fe Bader basins and (b) the lattice parameters *a* and *c* for range of $U_{eff}$ values for the

antiferromagnetic arrangement of orthorhombic FeS. The experimentally determined values of Wintenberger *et al.* (1978) for the lattice parameters *a'*, *b'* and *c'* of the low-temperature orthorhombic structure are shown in (a) by solid, dashed and dotted lines respectively. The experimentally determined value for the magnetic moment, including the associated error in this value, is shaded in (b).

These plots demonstrate the importance of electron correlations in the form of the $U_{eff}$ parameter for the GGA+U description of the low-temperature form of cubic FeS. The antiferromagnetic arrangement predicts orthorhombic structures for all $U_{eff}$ values tested. The increase in the Fe magnetic moments is very similar to that seen in all other magnetic cases upon introduction of the $U_{eff}$ parameter. The *a* and *b* lattice parameters show a small amount of orthorhombic distortion for all $U_{eff}$ values, and for $U_{eff}$ = 2 eV the predicted *a*, *b* and *c* lattice parameters and the predicted Fe magnetic moment are in excellent agreement with the experimentally determined values. From these calculations it is apparent that the introduction of the $U_{eff}$ parameter correctly predicts the orthorhombic structure when used in conjunction with the experimental antiferromagnetic structure, and that a $U_{eff}$ value of 2 eV provides an excellent prediction of all three lattice parameters and the magnetic moment on each Fe atom; in fact all of these properties are predicted to within experimental error.

Figure 5.14 (a), (b) and (c) shows the calculated electronic DOS for the orthorhombic FeS structures, with $U_{eff}$ = 0, 2 and 4 eV respectively, in the antiferromagnetic arrangement. The electronic DOS for the case where $U_{eff}$ = 2 eV shows a band-gap opening with width 0.7 eV, at 0.1 eV above the Fermi level, which for $U_{eff}$ = 4 eV, has increased to a width of 2 eV.

Assuming, based upon the correct description provided of the lattice parameters and magnetic moment, that a $U_{eff}$ value of 2 eV is correct the DOS

calculations suggest that the low-temperature orthorhombic phase of cubic FeS is metallic at 0 K. It is important to note that the antiferromagnetic electronic DOS plot of figure 5.14 (b) only shows one spin-polarisation of the Fe atoms, suggesting that this corresponds to the DOS for one layer of Fe atoms, which lie in the *ab* plane. The next layer of Fe atoms have magnetic moments aligned in the opposing direction, and would have an electronic DOS equivalent to a mirror image, reflected in the y = 0 plane.

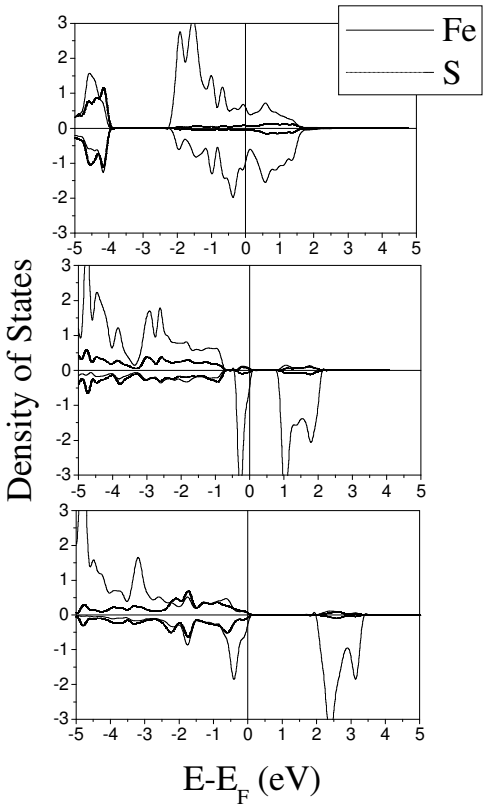


Figure 5.14 (a), (b), (c) – Electronic DOS graphs for the calculations on the antiferromagnetic arrangement of orthorhombic FeS. The cases shown are for $U_{eff}$ values of (a) 0, (b) 2 and (c) 4 eV.

### 5.3.7 Comparison of Structures

Figure 5.15 shows the relative internal energies for the three magnetic arrangements of the initial orthorhombic structure. It is clear from this relationship that the antiferromagnetic arrangement is the most stable for all $U_{eff}$ values tested, and the relative internal energies are similar to that found previously for the cubic structure, with the ferromagnetic structure more stable than the non-magnetic for all but $U_{eff}$ = 0.5 eV.

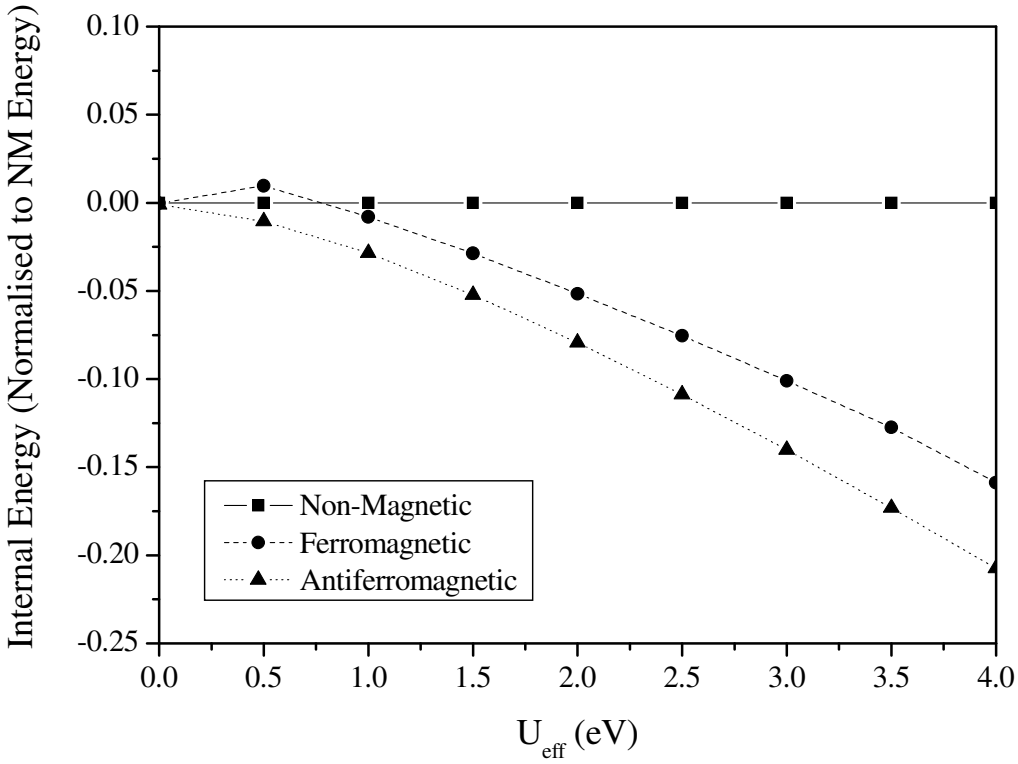


Figure 5.15 – Plot of the relative internal energies of the non-magnetic, ferromagnetic and antiferromagnetic arrangements for the low-temperature orthorhombic FeS structure for a range of $U_{eff}$. All energies are normalised to the non-magnetic energies

Increasing the applied $U_{eff}$ value leads to the non-magnetic solution becoming increasingly higher in energy than either the ferromagnetic or antiferromagnetic

solutions, suggesting that greater electron correlation make magnetic solutions far more likely. The finding that the antiferromagnetic arrangement is the most stable at $U_{eff}$ = 2 eV is in excellent accord with experiment.

### 5.3.8 Exchange Constant Calculations

Further calculations were undertaken to examine the exchange interactions between Fe-Fe nearest-neighbours for the antiferromagnetic and ferromagnetic phases, using the relaxed antiferromagnetic structure corresponding to scenario (1) (figure 5.2) and undertaking further calculations using scenarios (2) (figure 5.3 (a)) and (3) (figure 5.3 (b)). The internal energies of the resultant structures can then be used to predict the exchange constants $J_{ij}$ and constant paramagnetic energy $H_0$ for a range of $U_{eff}$ values using Equation (2.2.41). Table 5.11 shows that the predicted exchange constants agree with the proposed $|J_{12}| < |J_{13}|$ and $|J_{12}| < |J_{14}|$ stipulations of Wintenberger & Buevoz (1978) for $U_{eff}$ values of 2, 2.5, 3 and 4 eV only.

The predictions of the Néel temperature using Equation (2.2.42) for all but $U_{eff}$ = 0 eV lead to overestimations for this quantity, with $U_{eff}$ = 2 eV predicting $T_N$ to be 2178 K. These overestimations are almost certainly due to the failure of the mean field approximation when applied to Fe materials, and possibly the omission of Fe next-nearest-neighbour interactions (Swendsen, 1973)

Table 5.11 – Calculated exchange constants and constant paramagnetic energy $H_0$ for varying $U_{eff}$ for the orthorhombic FeS structure.

| U(eV) | $J_{12}$ (K) | $J_{13}$ (K) | $J_{14}$ (K) | $H_0$ (eV) |
|---|---|---|---|---|
| 0 | -5.431 | -5.396 | -4.440 | -25.982 |
| 0.5 | -48.727 | -48.675 | -48.263 | -25.004 |
| 1 | -46.374 | -46.488 | -45.573 | -24.351 |
| 1.5 | -52.999 | -52.920 | -45.994 | -23.791 |
| 2 | -57.833 | -68.025 | -57.893 | -23.311 |
| 2.5 | -75.838 | -75.984 | -75.952 | -22.881 |
| 3 | -91.263 | -91.429 | -92.494 | -22.471 |
| 3.5 | -108.806 | -108.568 | -110.826 | -22.087 |
| 4 | -127.586 | -127.708 | -130.854 | -21.728 |

### 5.3.9 Interatomic Potential Model: Orthorhombic FeS

The interatomic potential model originally derived for the mackinawite structure is applied to the FeS orthorhombic structure. Starting with the experimental structure of Wintenberger *et al.* (1978), the calculated lattice parameters and angles of the relaxed structure are given in table 5.12.

Table 5.12 – lattice parameters and angles of orthorhombic FeS calculated using the Fe-S interatomic potential.

| a (Å) | b (Å) | c (Å) | α (°) | β (°) | γ (°) |
|---|---|---|---|---|---|
| 5.30 | 5.74 | 4.63 | 89.94 | 89.98 | 90.00 |

There are large discrepancies between the experimentally observed lattice parameters and those calculated by the potential model. It is highly likely that the lack of any description of magnetism within the potential model leads to the large inaccuracies observed in the predicated structure since, as has been shown previously, the orthorhombic transition is magnetic in nature. Extension of the potential model to

include magnetic effects would be required to describe this effect using this method.

## 5.4 Summary

This study has sought to test the applicability of the GGA+U method in the description of both the high- and low-temperature structures of cubic FeS. For both structures it has been shown that pure GGA in the absence of a $U_{eff}$ value is unable to provide an adequate description, evidenced by large underestimations in both the lattice parameters and Fe magnetic moment. This is true regardless of the initial or resulting Fe magnetic moment arrangements, and in all cases the relaxed structures are predicted to possess cubic or very slightly distorted cubic structures, to be metallic in nature and to consist of low-spin Fe. These calculations clearly demonstrate that pure GGA is unable to accurately reproduce the experimentally determined lattice structure or the Fe magnetic moment for either the low- or high- temperature FeS structures. An interatomic potential treatment of the cubic structure, which does not consider magnetic interactions, is shown to agree well with these GGA results, suggesting that magneto-structural effects within the structure play a major role.

Upon introduction of the $U_{eff}$ parameter it is found that the antiferromagnetic arrangement of Fe magnetic moments is considerably more stable than the non-magnetic or the ferromagnetic for both cubic and orthorhombic structures, and that this holds for all $U_{eff}$ values between and including 0.5 eV and 4 eV. The non-magnetic solutions are the least stable arrangements for almost all $U_{eff}$ values tested, demonstrating the preference of the Fe atom to relax into the high-spin configuration in these structures. It is noted in all simulations that the introduction of the $U_{eff}$

parameter has very little effect upon the structure unless it is accompanied by an ordered configuration of magnetic moments. In the case of the cubic structure, the symmetry of the ferromagnetic arrangement preserves the cubic symmetry of the unit cell; this situation provides an analogy to the high-temperature paramagnetic structure where thermal fluctuations cause the Fe magnetic moments to randomise and lead to the cubic structural symmetry. The experimentally determined values for the lattice parameters of this structure are most accurately reproduced with an applied $U_{eff}$ of 2 eV, and for this value the predicted magnetic moment associated with each Fe atom is 3.63 $\mu_B$.

For all $U_{eff}$ values tested, relaxation of the cubic structure with an antiferromagnetic magnetic moment arrangement predicts a tetrahedrally distorted structure with $a = b \neq c$. $U_{eff}$ values below 1 eV produce a tetrahedral distortion such that the $c$ parameter is shorter than the $a$ parameter; for $U_{eff}$ values greater than 1 eV the opposite is true and the $c$ parameter is elongated compared to the $a$ parameter. This behaviour has little correlation to the magnetic moments present on each Fe atom, suggesting that it is instead related to the applied $U_{eff}$ value and hence the level of electron correlation on the Fe atoms.

For the low-temperature orthorhombic structure, introduction of the $U_{eff}$ parameter leads to similar predictions to that seen in the cubic case. The antiferromagnetic solution is the most stable for all $U_{eff}$ values tested. It is noted that even the ferromagnetic solution gives orthorhombic structures for $U_{eff}$ values of 2 eV and 3eV, suggesting an asymmetry introduced into the structure by this parameter regardless of the orientations of the applied magnetic moments. Consideration of the relaxed structures produced by antiferromagnetic magnetic arrangements show that the correct orthorhombic structure, where $a > b > c$, is correctly predicted for a $U_{eff}$

value of 2 eV. This value also leads to predictions for the lattice parameters and Fe magnetic moments for the low-temperature orthorhombic structures to within the error of the experimental methods used. Since this requires all three lattice parameters to assume different values this is an impressively accurate set of predictions by the GGA+U formulism of DFT.

Using the value of 2 eV to determine the electronic structure of the high-temperature form of cubic FeS, the electronic DOS demonstrates that the ferromagnetic form is semi-metallic. However this would not be seen experimentally since the spins are randomised, and instead metallic behaviour should be expected. The predicted electronic structure of the low-temperature antiferromagnetic orthorhombic phase is also metallic, with the Fermi level residing 0.1 eV from the top of a Fe *d*-band, and a band-gap of width 0.7 eV above this band.

Comparing the energies of the two phases for each magnetic arrangement, we note that the differences in energies between the cubic and orthorhombic structures are many times smaller than those between different magnetic arrangements. This may indicate that the transition between the two phases is likely to be driven by the ordering of the magnetic moments below the transition temperature. The suggestion that the orthorhombic phase of FeS contains low-spin Fe has been proved to be incorrect, and instead the Fe must be high spin, in the antiferromagnetic coordination of figure 5.2, in order to precipitate the experimentally observed transition. This would appear to support the first mechanism proposed for the transition (Wintenberger *et al.*, 1978) where it is caused by generalised exchange interactions in the presence of orbital degeneracy. Finally, the three exchange constants for the low-temperature orthorhombic structure have been determined at all $U_{eff}$ values tested, with a $U_{eff}$ value of 2 eV giving $J_{12}$ = -25.70 K, $J_{13}$ = -30.23 K and $J_{14}$ = -25.73 K.

Experimental scrutiny of these value would provide an excellent test of the model presented in this work.

# 6. Summary

This thesis has used both interatomic potential and *ab initio* materials modelling methods to provide descriptions of the iron sulfides mackinawite, greigite and cubic FeS. The materials examined have been found to demonstrate a wide range of properties and behaviour, and as such the models developed for each are individual to each material.

Simulations of mackinawite, FeS, have shown that DFT-GGA gives an excellent description of individual layers of this sulfide, with correct predictions for the metallic and non-magnetic behaviour. However, it has been found that GGA and GGA+U fail to account for the dispersive forces acting between layers. In response to this difficulty an interatomic potential has been derived which describes the {100}, {010}, {001}, {110}, {101}, {011} and {111} surfaces of mackinawite, and from considerations of the surface energies, reproduces the observed crystal morphology accurately. The GGA model is extended to examine the introduction of transition metal impurity atoms in the interstitial sites between layers. It is found that the impurity atoms contribute to the metallic behaviour of the mackinawite, where it is found that these atoms bond to the neighbouring S atoms.

The greigite ($Fe_3S_4$) structure has been examined using both the GGA and GGA+U DFT formalisms, where the experimentally determined lattice parameters, inverse spinel structure and magnetic moment are reproduced most accurately when a $U_{eff}$ value of 1 eV is applied. This phase is determined to be semi-metallic in nature,

similar to magnetite. A low-temperature monoclinic form of greigite is postulated, in analogy to that seen in magnetite below the Verwey transition, to test the existence of any low-temperature structural transition in the sulfide. Although this phase is found to exist at a potential energy surface minimum, it is found to be energetically unfavourable compared to the spinel form for all $U_{eff}$ values tested.

Cubic FeS is simulated using all three methods previously mentioned, namely GGA, GGA+U and the interatomic potential derived previously for mackinawite. It is found that GGA provides a poor description of both the high-temperature cubic and low-temperature orthorhombic structures, regardless of the magnetic ordering initially applied. This situation is seen to change dramatically upon introduction of the $U_{eff}$ parameter, where a value of 2 eV gives an excellent description of the high-temperature cubic lattice parameters, using a ferromagnetic ordered arrangement. This preserves the cubic symmetry seen experimentally in the paramagnetic structure, where the magnetic moments align in random directions. A $U_{eff}$ value of 2 eV (with the antiferromagnetic moment alignment) also provides a description of the low-temperature orthorhombic structure, providing predictions of all three lattice parameters and the Fe magnetic moment to within experimental error. The exchange parameters are calculated for the low-temperature structure, although the mean-field approximation is seen to predict the Néel temperature to be too high.

The range of properties these iron sulfides display has offered an excellent test of the theoretical methods implemented. Whilst DFT and IP methods have proved successful in previous studies of the iron sulfides pyrite and troilite, the metastable phases examined in this thesis are much more complex. The $U_{eff}$ parameter was originally designed to improve the description of Fe in oxidess; we have shown that its application to sulfides improves the description of these phases immensely, even

more so than in the oxides, although different $U_{eff}$ values are required to describe different material properties. This may be related to the lower level of electron correlation associated with the Fe atoms in the sulfides compared to the oxides, as evidenced by the lower values of $U_{eff}$ (0, 1 and 2 eV for mackinawite, greigite and cubic FeS respectively) required in the descriptions of the sulfides compared to the oxides (around 4 eV for magnetite (Piekarz *et al.* 2007) and hematite (Rollman *et al.*, 2004), and values of 3 or 5 for wüstite (Persson *et al.*, 2006)).

The complex magnetic behaviour of the iron sulfide family makes a complete description very difficult. For instance, the formation and transitions between the iron sulfides examined here could be predicted if the models for each were in the same form; unfortunately, what works for mackinawite, namely a non-magnetic interatomic potential description, is insufficient to describe either greigite or cubic FeS, where it has been shown that magnetism plays a major role. In fact, considering only the DFT descriptions of the three materials, the requirement for a different $U_{eff}$ value in each case means that the energies produced for each phase by these models can not be compared in any meaningful way.

The success of the models in the prediction of the Fe-S materials investigated in this thesis provides a platform on which further research can be undertaken. The description of greigite provided by the GGA+U simulations affords the opportunity of investigating the surfaces of this mineral, including its potential application as a catalyst. The simulations of the incorporation of impurity atoms into the mackinawite structure, Ni in particular, suggest that it should be straightforward to also dope the greigite structure with Ni impurities, offering the possibility of simulating the surfaces of greigite which resembles the “cubane clusters” and other ferrodoxin-type structures which are used in a many enzymes found in nature.

The success of the incorporation of impurities into the mackinawite structure suggests that research into removing heavy metals ions, including actinide atoms, from solution should be possible. Even without individual interatomic potentials for each impurity, small scale DFT calculations can be undertaken. Application of a previous DFT description of polydymite ($Ni_3S_4$) (Wang *et al.*, 2007), together with the description of greigite presented here opens up the possibility of studying both Fe-doped polydymite and Ni-doped greigite, as well as the intermediate phase violarite ($Fe^{2+}Ni_2{}^{3+}S$), an economically important constituent of Ni ores.

# References


Ahuja R., Auluck S., Söderlind P., Eriksson O., Wills J. M., Johansson B., *Phys. Rev. B*, **50**, 11183 (1994)

Amador C., Lambrecht W. R. L., Segall B., *Phys. Rev. B*, **46**, 1870 (1992)

Anisimov V. I., Zaanen J., Andersen O. K., *Phys. Rev. B*, **44**, 943 (1991)

Anisimov V. I., Solovyev I. V., Korotin M. A., Czyzyk M. T., Sawatzky G. A., *Phys. Rev. B*, **48**, 16929 (1993)

Anisimov V. I., Aryasetiawan F., Liechtenstein A. I., *J. Phys.: Condens. Matt.*, **9**, 767 (1997)

Aragón R., *Phys. Rev. B*, **46**, 5328 (1992)

Bader R. F. W., Carroll M. T., Cheeseman J. R., Chang C., *J. Am. Chem. Soc.*, **109**, 7968 (1987).

Ballone P., Galli G., *Phys. Rev. B*, **42**, 1112 (1990)

Benning L. G., Wilkin R. T., Barnes H. L., *Chemical Geology*, **167**, 25 (2000)

Berner R. A., *Science*, **137**, 669 (1962)

Berner R. A., *J. Geol*., **72**, 293 (1964)

Berner R. A., *Am. J. Sc.*, **265**, 773 (1967)

Bertaut E. F., Burlet P., Chappert J., *Solid State Comm.*, **3,** 335 (1965)

Bither T. A., Bouchard R. J., Cloud W. H., Donohue P. C., Siemons W., *J. Inorg. Chem*., **7**, 2208 (1968)

Blakemore R., *Science*, **190**, 377 (1975)

Blanchard M., Wright K., Gale J. D., Catlow C. R. A., *J. Phys. Chem. C***, 111**, 11390 (2007)

Bloch F., *Z. Physik*, **52**, 555 (1928)

Blöchl P. E., Jepsen O., Andersen O. K., *Phys. Rev. B*, **49**, 16223 (1994)

Boese A. D. Handy N. C., *J. Chem. Phys.*, **114**, 5497 (2001)

Born M. M., Huang K., *Dynamical Theory of Crystal Lattices*, Oxford University Press (1954)

Boursiquot S., Mullet M., Abdelmoula M., Genin J. M., Ehrhardt J.-J., *Phys. Chem. Minerals*, **28**, 600 (2001)

Braga M., Lie S. K., Taft C. A., Lester Jr. W. A., *Phys. Rev. B*, **38**, 10837 (1988)

Bragg W. L., *Proc. Royal Soc*., **A89**, 468 (1913)

Bullett D. W., *J. Phys. C: Solid State Phys.*, **15** 6163 (1982)

Cai J., Philpott M. R., *Computational Materials Science*, **30**, 358 (2004)

Cairns-Smith A. G., Hall A. J., Russell M. J., *Origins of Life and Evolution in the Biosphere*, **22**, 161 (1992)

Callaway J., Wang C. S., *Phys. Rev. B*, **16**, 2095 (1977)

Ceperley D. M., Alder B. J., *Phys. Rev. Lett.*, **45**, 566 (1980)

Chang L., Roberts A., Tang Y., Rainford B. D., Muxworthy A. R., Chen Q., *J. Geophys. Res.,* **113**, B06104 (2008)

Clark, A. H., *Neues Jahrb. Mineral Monatsch,* **1**, 300 (1966)

Clark A. H., *Neues Jahrb. Mineral Monatsch*, **6**, 282 (1969)

Clark A. H., *Am. Min.*, **55**, 1802 (1970a)

Clark A. H., *Economic Geology*, **65**, 590 (1970b)

Clerc D. G., *J. Phys. Chem. Solids*, **60**, 103 (1999)

Coey M. D., Morrish A. H., Sawatzky G. A., *J. Phys. (Paris) Colloq.*, **32**, C1 (1971)

Cody G. D., *Annu. Rev. Earth Planet. Sci.*, **32**, 569 (2004)

de Boer P. K., de Groot R. A., *Phys. Lett. A*, **256**, 227 (1999)

de Leeuw N. H., Parker S. C., Sithole H. M., Ngoepe P. E., *J. Phys. Chem. B*, **104**, 7969 (2000)

de Médicis R., *Science*, **170**, 1191 (1970)

Dekkers M. J., Passier H. F., Schoonen M. A. A., *Geophys. J. Int*., **141**, 809 (2000)

Deulkar S. H., Bhosale C. H., Sharon M., Neumann-Spallart M., *J. Phys. Chem. Solids*, **64**, 539 (2003)

Dick B. G., Overhausen A. W., *Phys. Rev.*, **112**, 90 (1958)

Dirac P. A. M.. *Proc. Cambridge Philos. Soc.*, **26**, 376 (1930)

Dudarev S. L., Botton G. A., Savrasov S. Y., Humphreys C. J., Sutton A. P., *Phys. Rev. B*, **57**, 1505 (1998)

Ebert H., Perlov A., Mankovsky S., *Solid State Comm.*, **127**, 443 (2003)

Eckart C., *Phys. Rev.*, **46**, 383 (1935)

Ellmer K., Hopfner C., *Philos. Mag. A*, **75**, 1129 (1997)

Engel E., Facco Bonetti A., Keller S., Andrejkovics I., Dreizler R. M., *Phys. Rev. A*, **58,** 964 (1998)

Evans, H. T. Jr., Berner R. A., Milton C., *Geol. Soc. Am. Prog. 1962*, **47a** (1962)

Evans H. T. Jr., Milton C., Chao E. C. T., Adler I., Mead C., Ingram B., Berner R. A., *USGS Professional Papers*, **475-D**, 64 (1964)

Ewald P., *Ann. Phys.*, **369**, 253 (1921)

Farina M., Esquivel D. M. S., Debarros H., *Nature*, **343**, 256 (1990)

Fermi E., *Z. Phys.*, **48**, 73 (1928)

Filippi C., Umrigar C. J., Taut M., *J. Chem. Phys.*, **100**, 1290 (1994)

Fleet M. E., *Phys. Chem. Minerals*, **8**, 241 (1982)

Furukawa Y., Barnes H. L., *Geochim. Cosmochim. Acta*, **60**, 3581 (1996)

Gale J. D., Rohl A. L., *Mol. Simul.*, **29**, 291 (2003)

Gibbs G. V., Downs R. T., Prewitt C. T., Rosso K. M., Ross N. L., Cox D. F., *J. Phys. Chem. B*, **109**, 21788 (2005)

Gibbs G. V., Cox D. F., Rosso K. M., Ross N. L., Downs R. T., Spackman M. A., *J. Phys. Chem. B*, **111**, 1923 (2007)

Glukhovtsev M. N., Bach R. D., Nagel C. J., *J. Phys. Chem. A*, **101**, 316 (1997)

Goffredi S. K., Warén A., Orphan V. J., Van Dover C. L., Vrijenhoek R. C., *Appl. Environ. Microbiol.*, **70**, 3082 (2004)

Goodenough J. B., *J. Phys. Chem. Solids*, **30**, 261 (1969)

Gourlay A. R., Watson G. A., *Computational methods for matrix eigenproblems, Wiley* (1973)

Grau-Crespo R., Corà F., Sokol A. A., de Leeuw N. H., Catlow C. R. A., *Phys. Rev. B*, **73**, 35116 (2006)

Hafner J., *Computer physics communications*, **177**, 6 (2007)

Hamajima T., Kambara T., Gondaira K. I., Oguchi T., *Phys. Rev. B*, **24**, 3349 (1981)

Han W., Gao M., *Crystal Growth and Design*, **8**, 1023 (2008)

Harris J., Jones R. O., *J. Phys. F Metal Phys.*, **4**, 1170 (1974)

Hatchett C., *Philos. Trans.*, **94**, 385 (1804)

He Z., Yu S.-H., Zhou X., Li X., Qu J., *Adv. Funct. Mat.*, **16**, 1105 (2006)

Heinen W., Lauwers A. M., *Origins Life E: Biosphere*, **26**, 131 (1996)

Henkelman G., Arnaldsson A., Jónsson H., *Comput. Mater. Sci.* **36**, 254 (2006)

Heywood B. R., Bazylinski D. A., Garrett-Reed A., Mann S., Frankel R. B., *Naturwissenschaften*, **77**, 536 (1990)

Hobbs D., Hafner J., *J. Phys. Condens. Matter*, **11** 8197 (1999)

Hohenburg P., Kohn W., *Phys. Rev.*, **136**, B864 (1964)

Horiuchi, S., Wada, H., Noguchi, T., *Naturwissenschaften*, **57**, 670 (1970)

Horiuchi, S., Wada, H., Moori, T., *J. Cryst. Growth*, **25**, 624 (1974)

Hubbard J., *Proc. Roy. Soc. A*, **276**, 238 (1963)

Huggins M. L., *J. Am. Chem. Soc.*, **44**, 1841 (1922)

Hung A., Muscat J., Yarovsky I., Russo S. P., *Surface Science*, **513**, 511 (2002)

Hung A., Yarovsky I., Russoy S. P., *Philosophical Magazine Letters*, **84**, 175 (2004)

Hunger S., Benning L. G., *Geochemical Transactions*, **8**, 1 (2007)

Jannasch H. W., Wirsen C. O., *Bioscience*, **29**, 592 (1979)

Jellinek F., *Acta Crystallogr.*, **10**, 620 (1957)

Katnelson M. I., Irkhin V. Y., Chioncel L., Lichtenstein A. I., de Groot R. A., *Rev. Mod. Phys.*, **80**, 2 (2008)

Keller L. P., Hony S., Bradley J. P., Molster F. J., Waters L. B. F. M., Bouwman J., de Koter A., Brownleek D. E., Flynn G. J., Henning T., Mutschke H., *Nature*, **417**, 148 (2002)

Kittel C., *Introduction to Solid State Physics*, Wiley (1986)

Kohn W., Sham L. J., *Phys. Rev.,* **140**, A1133 (1965)

Kostov I., Minceva-Stefanova J., *Sulfide Minerals: Crystal Chemistry, Parageneses and Systematics*, E. Bulgarian Acad. Sci. Inst. Geol. (1982)

Kotliar G., Savrasov S. Y., Haule K., Oudovenko V. S., Parcollet O., Marianetti C. A., *Rev. Mod. Phys.*, **78**, 865 (2006)

Kouvo O., Vuorelainen Y., Long J. V. P., *Am. Mineral.*, **48**, 511 (1963)

Kresse G., Joubert D., *Phys. Rev. B*, **50**, 1758 (1999)

Kristyán S., Pulay P., *Chem. Phys. Lett.*, **229**, 175 (1994)

Krupp R. E., *Eur. J. Mineral*., **6**, 265 (1994)

Kullerud G., Yoder H. S., *Economic Geology*, **54**, 533 (1959)

Langreth D. C., Perdew J. P., *Phys. Rev. B*, **15**, 2884 (1977)

Lennie A. R., Redfern S. A. T., Schofield P. F., Vaughan D. J., *Min. Mag.*, **59**, 677 (1995)

Lennie A. R., Redfern S. A. T., Champness P. E., Stoddart C. P., Schofield P. F., Vaughan D. J., *Am. Mineralogist*, **82**, 302 (1997)

Letard I., Sainctavit P., Menguy N., Valet J.-P., Isambert A., Dekkers M., Gloter A., *Physica Scripta*, **T115**, 489 (2005)

Lewars E., *Computational Chemistry*, Kluwer Academic Publishers (2003)

Lewis G. V., Catlow C. R. A., *J. Phys. C: Solid State Phys.*, **18**, 1149 (1985)

Li J., Fei Y., Mao H. K., Hirose K., Shieh S. R., *Earth Planet. Sci. Letts.,* **193**, 509 (2001)

Lie S. K., Taft C. A., *Phys. Rev. B*, **28**, 7308 (1983)

Liechtenstein A. I., Anisimov V. I., Zaanen J., *Phys. Rev. B*, **52**, R5467 (1995)

Lill R., Mühlenhoff U., *Annu. Rev. Biochem.*, **77**, 669 (2008)

Liu J., Valsaraj K. T., Devai I., DeLaune R. D., *J. Hazard. Mater.*, **157**, 432 (2008)

Livens F. R., Jones M. J., Hynes A. J., Charnock J. M., Mosselmans J. F. W., Hennig C., Steele H., Collison D., Vaughan D. J., Pattrick R. A. D., Reed W. A., Moyes L. N., *J. Environmental Radioactivity*, **74**, 211 (2004)

Luther III G. W., *Geochim. Cosmochim. Acta*, **51**, 3193 (1987)

Luther III G. W., Rozan T. F., Taillefert M., Nuzzio D. B., Di Meo C., Shank T. M., Lutz R. A., Cary S. C., *Nature*, **410**, 813 (2001)

Mann S., Sparks N. H. C., Frankel R. B., Bazylinski D. A., Jannasch H. W., *Nature*, **343**, 258 (1990)

Martin D. H., *Magnetism in Solids*, Illiffe Books (1967)

McCammon C., Zhang J., Hazen R. M., Finger L. W., *Am. Mineralogist*, **77**, 937 (1992)

Mermin N. D., *Phys. Rev.*, **137**, A1441 (1965)

Methfessel M., Paxton A. T., *Phys. Rev. B*, **40**, 3616 (1989)

Monkhorst H. J., Pack J. D., *Phys. Rev. B*, **13**, 5188 (1976)

Morice J. A., Rees L. V. C., Rickard D. T., *J. Inorg. Nucl. Chem.*, **31**, 3797 (1969)

Morse J. W., Millero F. J., Cornwell J.C., Rickard D., *Earth-Sci. Rev.*, **24**, 1 (1987)

Mott N. F., *Phil. Mag. B*, **42**, 327 (1980)

Moyes L. N., Jones M. J., Reed W. A., Livens F. R., Charnock J. M., Mosselmans J. F. W., Hennig C., Vaughan D. J., and Pattrick R. A. D., *Environmental Science & Technology*, **36**, 179 (2002)

Mullet M., Boursiquot S., Abdelmoula M., Génin J.-M., Ehrhardt J.-J., *Geochimica et Cosmochimica Acta*, **66**, 829 (2002)

Mullet M., Boursiquot S., Ehrhardt J.-J., *Colloids and Surfaces A: Physicochem. Eng. Aspects*, **244**, 77 (2004)

Murowchick J. B., Barnes H. L., *Am. Mineralogist*, **71**, 1243 (1986)

Muscat J., Hung A., Russo S., Yarovsky I., *Phys. Rev. B*, **65**, 54107 (2002)

Nair N. N., Schreiner E., Pollet R., Staemmler V., Marx D., *J. Chem. Theory Comput.*, **4**, 1174 (2008)

Nicolet Y., Piras C., Legrand P., Hatchikian C. E., Fontecilla-Camps J. C., *Structure*, **7**, 13 (1999)

Novák P., Boucher F., Gressier P., Blaha P., Schwartz K., *Phys. Rev. B*, **63**, 51120 (2001)

Ohfuji H., Rickard D., *Earth Planet. Sci. Lett.*, **241**, 227 (2006)

Okazaki A, Hirakawa K., *J. Phys. Soc. Jpn.*, **11**, 930 (1956)

Oliver, G. L., Perdew, J. P., *Phys. Rev. A*, **20** 397 (1979)

Parker V. B., Khodkovskii I. L., *J. Phys. Ref. Data*, **24**, 1699 (1995)

Parr R., Yang W., *Density Functional Theory of Atoms and Molecules*, Oxford (1989)

Parry D. E., *Surface Science*, **49**, 433 (1975)

Pauling L., *General Chemistry*, Dover (1988)

Payne M. C., Teter M. P., Allan D. C., Arias T. A., Joannopulos J. D., *Reviews of Modern Physics*, **64**, 1045 (1992)

Peng Y., Xi G., Zhong C., Wang L., Lu J., Sun X., Zhu L., Han Q., Chen L., Shi L., Sun M., Li Q., Yu M., Yin M., *Geochimica et Cosmochimica acta*, **73**, 4862 (2009)

Perdew J. P., McMullen E. R., Zunger A., *Phys. Rev. A,* **23**, 2785 (1981)

Perdew J. P., Wang Y., *Phys. Rev. B*, **45**, 13244 (1992)

Persson K., Bengtson A., Ceder G., Morgan D., *Geophys. Res. Letts*, **33**, 16306 (2006)

Pickett W. E., *Comput. Phys. Rep*., **9**, 115 (1989)

Piekarz P., Parlinski K., Oleś A. M., *Phys. Rev. B*, **76**, 165124 (2007)

Pinto H. P., Elliot S. D., *J. Phys. Condens. Matter*, **18**, 10427 (2006)

Pósfai M., Buseck P. R., Bazylinski D. A., Frankel R. B., *Science*, **280**, 880 (1998a)

Pósfai M., Buseck P. R., Bazylinski D. A., Frankel R. B., *American Mineralogist*, **83**, 1469 (1998b)

Press W. H., Flannery B. P., Teukolsky S. A., Vetterling W. T., *Numerical Recipes*, Cambridge University Press New York (1986)

Rakcecha V. C., Satya Murthy N. S., *J. Phys. C*, **11**, 4389 (1978)

Raybaud P., Kresse G., Hafner J., Toulhoat H., *J. Phys. Condens. Matter*, **9**, 11085 (1997)

Rees D. C., Howard J. B., *Science*, **300**, 929 (2003)

Reich M., Becker U., *Chemical Geology*, **225**, 278 (2006)

Rickard D., Butler I. B., Oldroyd A., *Earth Planet. Sci. Letts.*, **189**, 85 (2001)

Rickard D., Morse J., *Mar. Chem.*, **97**, 141 (2005)

Rickard D., Luther III G. W., *Rev. Mineral. Geochem.*, **61**, 421 (2006)

Rickard D., Luther III G. W., *Chem. Rev.*, **107**, 514 (2007)

Rimstidt J. D., Vaughan D. J., *Geochim. Cosmochim. Acta*, **67**, 873 (2003)

Roberts A. P., *Earth Planet. Sci. Letts.*, **134**, 227 (1995)

Rohrbach A., Hafner J., Kresse G., *J. Phys. Condens. Matter*, **15**, 979 (2003)

Rollmann G., Rohrbach A., Entel P., Hafner J., *Phys. Rev. B*, **69**, 165107 (2004)

Rouxel O., Bekker A., Edwards K., *Science*, **307**, 1088 (2005)

Russell, M. J., Daniel, R. M., Hall, A. J., Sherringham, J. A., *J. Mol. Evol.*, **39**, 231 (1994)

Russell M. J., Hall A. J., *J. Geog. Soc. Lond.*, **154**, 377 (1997)

Russell, M. J., Martin, W., *Trends Biochem. Sci.*, **29**, 358 (2004)

Sadtler B., Demchenko D. O., Zheng H., Hughes S. M., Merkle M. G., Dahmen U., Wang L.-W., Alivisatos A. P., J. *Am. Chem. Soc*., **131**, 5285 (2009)

Salehpour M. R., Satpathy S., *Phys. Rev. B*, **41**, 3048 (1990)

Sarkar, S. C. *Am. Mineral.,* **56**, 1312 (1971)

Sasaki S., *Acta Cryst*., **B53**, 762 (1997)

Schlegal A., Wachter P., *J. Phys. Chem: Sol. Stat. Phys.*, **9**, 3363 (1976)

Schoonen M. A. A., Barnes H. L., *Geochim. Cosmochim. Acta*, **55**, 1505 (1991)

Schoonen M. A. A., Xu Y., Bebie J., *Origins Life E: Biosphere*, **29**, 5 (1999)

Shoesmith D. W., Taylor P., Bailey M. G., Owen D. G., *J. Electrochemical Soc*, **127**, 1007 (1980)

Skinner B. J., Erd R. C., Grimaldi F. S., *Am. Mineralogist*., **49**, 543 (1964)

Solovyev I. V., Dederichs P. H., Anisimov V. I., *Phys. Rev. B*, **50**, 16861 (1994)

Spender M. R., Coey J. M. D., Morrish A. H., *Canadian J. Phys.*, **50**, 2313 (1972)

Stanjek H., Fassbinder J. W. E., Vali H., Wägele H., Graf W., *Euro. Jour. Soil. Sci.*, **45**, 97 (1994)

Steele H. M., Wright K., Hiller I. H., *Phys. Chem. Materials*, **30**, 69 (2003)

Stephenson A., Snowball I. F., *Geophys. J. Int.*, **145**, 570 (2001)

Stirling A., Bernasconi M., Parrinello M., *Journal of Chemical Physics*, **19**, 4934 (2003a)

Stirling A., Bernasconi M., Parrinello M., *Journal of Chemical Physics*, **118**, 8917 (2003b)

Suzuki Y., Kopp R. E., Kogure T., Suga A., Takai K., Tsuchida S., Ozaki N., Endo K., Hasimoto J., Kato Y., Mizota C., Hirata T., Chiba H., Nealson K. H., Horikoshi K., Kirschvink J. L., *Earth Planet. Sci. Letts.*, **242**, 39 (2006)

Swendsen R. H., *J. Phys. C: Solid State Phys.*, **6**, 3763 (1973)

Takai K., Komatsu T., Inagaki F., Horikoshi K., *App. Env. Microbiology*, **67**, 3618 (2001)

Takele S., Hearne G. R., *J. Phys. Conden. Matter*, **13**, 10077 (2001)

Takeno S., *Japan. Geol. Rept. Hiroshima Univ.,* **14**, 59 (1965)

Takeno S. and Clark A. H., *J. Sci. Hiroshima Univ. Ser. C*, **5**, 287 (1967)

Takeno S., Zôka H., Niihara T., *Am. Mineralogist*, **55**, 1639 (1970)

Tasker P. W., *J. Phys. Chem: Solid State Phys.*, **12**, 4977 (1979)

Taylor L. A., Finger L. W., *Carnegie Inst. Washington Geophys. Lab. Ann. Rep.*, **69**, 318 (1970)

Taylor P., *Am. Mineralogist,* **65**, 1026 (1980)

Terakura K., Oguchi T., Williams A. R., Kübler J., *Phys. Rev. B*, **30**, 4734 (1984)

Thauer R. K., Jungermann K., Decker K., *Bacteriological Review*, **41**, 100 (1977)

Thomas L. H., *Proc. Cambridge Philos. Soc.*, **23**, 542 (1927)

Tossell J. A., Vaughan D. J., Burdett J. K.*, Phys. Chem. Minerals*, **7**, 177 (1981)

Uda M., *Am. Mineralogist*, **50**, 1487 (1965)

Uda M., *Zeit. für anorg. alleg. Chem.,* **350**, 105 (1967)

Uda M., *Zeit. für anorg. alleg. Chem.*, **361**, 94 (1968)

Uhl M., Siberchicot B., *J. Phys.: Condens. Matter*, **7**, 4227 (1995)

Vandenberghe R. E., de Grave E., de Bakker P. M. A., Krs M., Hus J. J., *Hyperfine Interactions*, **68**, 319 (1992)

Vaughan D. J., *Am. Min.*, **54**, 1190 (1969)

Vaughan D. J., *Am. Min.*, **55**, 1807 (1970)

Vaughan D. J., Ridout M. S., *J. Inorg. and Nuc. Chem.*, **33**, 741 (1971)

Vaughan D. J., Craig J. R., *Mineral Chemistry of Metal Sulfides*, Cambridge University Press (1978)

Verati C., de Donato P., Prieur D., Lancelot J., *Chemical Geology*, **158**, 257 (1999)

Verwey E. J. W., Haayman P. W., *Physica*, **9**, 979 (1941)

Volbeda A., Fontecilla-Camps J. C., *Coord. Chem. Rev.*, **249**, 1609 (2005)

Von Damm K. L., *Ann. Rev. Earth Planet Sci.*, **18**, 173 (1990)

Vosko S. H., Wilk L., Nusair M., *Can. J. Phys.*, **58**, 1200 (1980)

Wächtershäuser G., *J. Theor. Biol.*, **187**, 483 (1997)

Wächtershäuser G., *Science*, **289**, 1307 (2000)

Wada H., *Bullet. Chem. Soc. Japan*, **50**, 2615 (1977)

Walde P., Goto A., Monnard P-A., Wessicken M., Luisi P. L., *J. Am. Chem., Soc.*, **116**, 7541 (1994)

Wang C. S., Klein B. M., Krakauer H., *Phys. Rev. Letts.*, **54**, 1852 (1985)

Wang J. H., Cheng Z., Brédas J.-L., Liu M., *J. Chem. Phys.*, **127**, 214705 (2007)

Ward J. C., *Pure App. Chem.*, **20**, 175 (1970)

Watson G. W., Kelsey E. T., de Leeuw N. H., Harris D. J., Parker S. C., *J. Chem. Soc. Faraday Trans.*, **92**, 433 (1996)

Watson J. H. P., Cressey B. A., Roberts A. P., Ellwood D.C., Charnock J. M., Soper A. K., *J. Magnetism and Magnetic Materials*, **214**, 13 (2000)

Wells S., Alfe D., Blanchard L., Brodholt J., Calleja M., Catlow R., Price D., Tyler R., Wright K., *Molecular Simulations*, **31**, 379 (2005)

Welz D. Rosenberg M., *J. Phys. Chem.: Solid State Phys.*, **20**, 3911 (1987)

Wenzel M. J., Steinle-Neumann G., *Phys. Rev. B*, **75**, 214430 (2007)

Wintenberger M., Buevoz J. L., *Solid State Communications*, **27**, 511 (1978)

Wintenberger M., Srour B., C. Meyer, Hartmann-Boutron F., Gros Y., *Journal de Physique*, **39**, 965 (1978)

Wolf S. A., Awschalom D. D., Buhrman R. A., Daughton J. M., von Molna S., Roukes M. L., Chtchelkanova A. Y., Treger D. M., **294**, *Science*, 1488 (2001)

Wolthers M., Charlet L., Linde P. R. V. D., Rickard D., Weuden C. H. V. D. *Geochimica et Cosmochimica Acta*, **69**, 3469 (2005)

Wright J. P., Attfield J. P., Radaelli P. G., *Phys. Rev. B*, **66**, 214422 (2002)

Yamaguchi, S., Katsurai, T., *Kolloid Z.*, **170**, 147 (1960)

Yamaguchi S., *Phys. Rev.*, **126**, 102 (1962)

Yi Q., Bengtson S., *Fossils Strata*, **24**, 1 (1989)

Zope R. R., Blundell S. A., *J. Chem. Phys.*, **115**, 2109 (2001)